UNIVERSITY OF BIRMINGHAM

Coupling a Solid Oxide Fuel Cell Exhaust with a Vapour Absorption Refrigeration System for Refrigerated Truck: Modelling and Experimental Investigation

By

Eridei Lucky Amakiri

(Student ID: 1314824)

A thesis submitted to the University of Birmingham for the degree of

Doctor of Philosophy

Centre for Fuel Cell and Hydrogen Research

School of Chemical Engineering

College of Engineering and Physical Sciences

University of Birmingham

APRIL 2020

ABSTRACT

Refrigerated trucks for both chilled and frozen products; pharmaceutical and perishable foods, are conventionally fitted with a vapour compression refrigeration system that is powered by either the vehicle main engine or an auxiliary diesel engine on board. This process increases the fuel consumption rate, greenhouse gas emissions especially during idling, reduced engine performance and efficiency, and increased noise pollutions among others. Hence, attentions have shifted to using available waste heat to drive heat driven refrigeration systems.

Vapour absorption refrigeration system (VARS) is one heat driven technology that has been in existence for decades. It has been mainly used in commercial building and recently has been looked at for automotive applications. Researches have been conducted to couple the vehicle engine exhaust heat with VARS for refrigerated trucks or car air-conditioning purposes. This process has its demerits of the unavailability of enough heat during idling times, noise and increased emissions. This thesis looked at the feasibility of using environmental friendly high temperature fuel cell (solid oxide fuel cell) auxiliary power system that generates electricity and heat. The electricity can be used for auxiliary load or on board appliances while the heat generated is harnessed to drive the VARS.

There is temperature mismatch between the SOFC exhaust heat (600-900^{o}C) and that required at the desorber of the VARS (120-240^{o}C). Therefore, an internally finned tube-in-shell heat exchanger and heat transfer fluid (thermal oil) were employed to couple these two different units (fuel cell exhaust heat and VARS).

A detailed component and system level modelling of the VARS is carried out and the influence of design and the various operating conditions was investigated. A brassboard was used to experimentally investigate the feasibility of the technology. Experimental results from the test bench are used to validate the modelling results and prove the practical feasibility of the technology. Results showed that 1.84 kW of heat was recovered from a simulated SOFC stack of 5 kW_e, at cathode exhaust flow rate of 0.03019 kg/s. The recovered amount of heat is able to cater to a 1 kW refrigeration load for a small refrigerated truck. It was also shown that a 1.84 kW of heat would still be recovered to meet the same 1 kW refrigeration load employing a 1 kWe SOFC at lower exhaust flow rates. Employing a 1 kW SOFC will increase the heat exchanger effectiveness and overall heat transfer coefficient by between 81.1 to 85 %, and 39.22 to 59.5 % respectively.

It was also shown that an evaporator temperature of 4^oC was achieved when the recovered simulated SOFC exhaust heat was integrated experimentally with the VARS. This was due to loss of heat at the desorber of the VARS where only a maximum of 0.5 kW (out of 1.84 kW) of heat was transferred from the coupling fluid (thermal oil) to the ammonia-water solution. This results in less ammonia desorption from the solution thereby causing reduced cooling at the evaporator.

There has been no study reported in the public domain as regards experimental work of a small VARS refrigerated truck, hence the work reported here is a novelty in this regard. Another scientific contribution/novelty of this research is the experimental integration of fuel cell exhaust heat as energy source to drive VARS for refrigerated transport application which has never been done

ACKNOLEDGEMENT

I want to first of all thank the almighty God for his guidance, protection, provision and wisdom to complete this study.

I want to specifically thank the Niger Delta Development Commission for providing the funding for me to pursue this programme.

My profound gratitude goes to my irreplaceable supervisors Prof. Robert Steinberger-Wilckens and Dr. Ahmad EL-Kharouf for their counselling, guidance, encouragement and support in all ramifications all through this programme.

I also want to thank my parents Mr. and Mrs Helen Ofoin Amakiri, my wife and son Mrs Ebieridei, Mr Justin Elnathan and other members of my immediate and extended family for their unending support. My thanks go to Pastor and Mrs. Angela Joseph Aduba and the entire Deeper Christian Life Ministry for their prayers, encouragement and support towards the completion of my project.

My gratitude also goes to Lynn Draper and John Hooper for their administrative assistance all through my programme. I also want to thank all my colleagues in the fuel cell group for the encouragement and support given to me during my research.

I sincerely thank Mr. Bob, Dave, Boyl and Chyntol for their technical support during the time of building the test rig for my project. I want to thank my flat mates Mrs. Chioma Madueke, Mr. Philip Oamen, Mr. Matthew Nanani, Mr. Andy and Mr. Uchenna for standing by me during my study. My sincere thanks also go to the families of Hon Samuel Godwill and Hon (Champion) Daniel Igali for their support.

Table of Contents

List of Figures

List of Tables

1 Chapter 1

INTRODUCTION

There is a steady increase in the world population as the day goes by, which invariably is causing an increase in the overall energy demand including the energy consumed by the food sector. This increase comes with higher global warming issues arising from the methods of energy supply. There will be a 45% increase in world energy demand by 2030 as predicted by Beddington [1]. The UK agricultural sector, manufacturing, distribution, retail, and consumption accounts for about 18% of UK total energy use, and 115 metric tonnes (Mt) of CO_2 emissions [2] . In the food chain, transportation plays a crucial role in the movement of foods. A study carried out by Mei el al. [3] showed that the transportation sector (automobiles and trucks) accounts for a substantial part of Western energy consumption. These automobiles and trucks use internal combustion engines and incur about 80% of the total energy expenditure in the transportation sector [4].

Due to the high deterioration rate of food such as vegetables, meat, fruits and milk etc. when exposed to ambient temperature, they are transported in refrigerated trucks with controlled temperature, and thereby delivered in good condition and quality. Refrigerated trucks use vapour compression (VC) refrigeration systems on board that are powered by electricity generated mostly by the main vehicle engine, or by an auxiliary diesel engine on board. This process increases fuel consumption rate of the vehicle and thus CO_2 emissions. More so, the refrigerants used in the conventional VC systems have a high global warming potential and deplete the ozone layer in cases of leakage. Hence, in the past few decades, attention has been shifting towards using

alternative, environmentally friendly means of refrigeration on trucks. One of such methods, amongst others, is the use of heat driven vapour absorption refrigeration system (VARS). The heat source normally comes from excess or waste heat. For instance, vehicle engine exhaust heat could be used as an energy source for a VARS on refrigerated trucks.

Using the fuel cell cathode exhaust heat as the energy source to drive a VARS on a refrigerated truck has the potential to be one of the environmentally friendly ways which can phase out the use of conventional VC systems on trucks. Venkataraman et al. [5] carried out a system modelling of a fuel cell exhaust driven VARS for truck refrigeration application and concluded that it is feasible. This PhD is to continue in that path and carry out components and system level modelling and experimental validation of the potential of a solid oxide fuel cell to drive a VARS refrigeration system.

1.1Fuel cells

A fuel cell is a device that electrochemically converts chemical energy stored in the fuel into electricity and heat without a combustion process. The heat generated by the reaction is carried out of the cell by the excess reactants and products, or through a cooling system. This heat can then be harnessed to drive a VARS. There are different types of fuel cells such as the Polymer Electrolyte Fuel Cell (PEFC), Alkaline Fuel Cell (AFC), Phosphoric Acid Fuel Cell (PAFC), Solid oxide Fuel Cell (SOFC), and Molten Carbonate Fuel Cell (MCFC). The PEFC and SOFC types have been the major beneficiaries of research and development, by today firmly establishing their technology. The PEFC is categorised as a low temperature type with a conventional operating temperature between 60 to 90^{o}C except for high temperature (HT)-PEFCs which operate up to

200^{o}C. On the other hand, the SOFC is a high temperature type with operating temperatures of 600 to 900^{o}C. Table 1.1 shows the comparison between the two technologies.

Table 1.1 Characteristic comparison of SOFC and PEFC technologies

Parameter	PEFC	SOFC
Operating temperature range	60 to 90^{o}C	600 to 900^{o}C
Automobile drivetrain suitability	YES	YES
Auxiliary Power Unit suitability	YES	YES
Fuel flexibility	No, only hydrogen (H_2)	YES, H_2, CH_4, CO, etc
Quality of waste heat	Poor, except for the HT-PEFC	Excellent
Suitability for VARS integration	Poor	Excellent
Start-up time	Quick	Extended

From Table 1.1, it can be seen that the benefit of using an SOFC with heat driven technology outweighs the advantages with a PEFC. This is because, the temperature of waste heat from a PEFC is too low, so if harnessed would not be efficient for the application with a VARS. PEFC possess quick start up times and are best suited for automobile drivetrain applications. On the other hand, the temperature of SOFC waste heat is high enough in that even with losses during heat recovery there is potential to drive heat driven technologies. SOFCs possess fuel flexibility (ability to utilize different types of fuel) due to the high temperature operation and can achieve an overall efficiency of over 85% if both the electricity and heat produced are utilised: in this way, they are operated in combined heat and power mode.

Amongst all heat driven cooling technologies, vapour absorption refrigeration systems (VARS) have been the most used technology because this is a well-established technology and has been used for decades. VARS is a cooling system that can be powered by heat from solar, geothermal and other sources, including waste or residual heat from process plants in order to cause a cooling or refrigeration effect. The temperature used for driving a VARS is in the range of 120 to 240 ^{0}C, depending on the application. The heat when applied at the desorber of the VARS separates a refrigerant-absorbent solution. The separated refrigerant vapour flows into the condenser, cooling down into liquid after rejecting heat to the surrounding. The liquid refrigerant passes through an expansion valve which further cools it down and reduce the pressure before entering the evaporator where it causes the cooling/refrigeration effect and turns to vapour. The refrigerant vapour leaves the evaporator and flows back into the absorber of the VARS where it mixes with the absorbent returning from the desorber, thereby forming the refrigerant-absorbent solution. The formed solution is then pumped into the desorber from the absorber by a pump for pressure increase and for repeat of the cycle. In comparison with the conventional electrical driven vapour compression cooling system (VCS), the desorber and the absorber of the VARS replace the compressor of the VCS. The only moving part is the pump and its electricity consumption is insignificant compared to the compressor of a VCS. Adjibade et al. [6] showed experimentally by using a vehicle engine exhaust as the energy source to drive a VARS, that the minimum temperature required at the desorber of the VARS was 140^{o}C. Therefore, an SOFC is a good choice to be used due to the high operating temperature resulting in higher exhaust heat that can be utilised if captured, hence the use of SOFC as heat source for this study.

1.2 Thesis objective and scope

The main objective of this research is to experimentally couple SOFC fuel cell and vapour absorption refrigeration system for a refrigerated truck application. Hence the scope will be looking at the following:

i. Identification of the type of heat driven VARS to be used.

ii. System level modelling and simulation of the VARS and its components.

iii. Experimental integration of VARS and fuel cell exhaust using a breadboard test rig.

iv. Validation of modelling results based on the experimental data obtained.

This research focuses mainly on the technical feasibility of using SOFC exhaust heat to successfully drive the VARS on board of a truck for refrigeration purposes. The experimental data obtained will be used to validate the modelling and simulation work carried out, and to make recommendations for components and system choice.

1.3 Structure of the thesis

This PhD thesis is organised as follows:

Chapter 2 gives a critical and thorough literature review ranging across heat driven refrigeration technologies, vapour absorption systems, working pairs of vapour absorption systems, engine exhaust heat driven vapour absorption systems, fuel cell exhaust heat driven vapour absorption systems, and operation mode of fuel cell system (heat following and electric following).

Chapter 3 gives an overview of the experimental test rig used for the study. It gives a brief description of all the components on the test rig and their functions. It outlines the experimental tests carried out and the procedures followed in the study. This gives a clear understanding of all single components' operation before finally integrating all the stages together. More so, the variables and measured parameters are highlighted.

Chapter 4 looks into the modelling of the VARS components starting with the double pipe heat exchanger, rectifier, and absorber with their parametric analysis.

Chapter 5 presents a detailed system level modelling of a single effect vapour absorption refrigeration system considered for the application. Different operating scenarios of the system are looked into here with various methods to improve the coefficient of performance of the refrigeration system.

Chapter 6 provides the details of experimental procedures and the results obtained at each step. It starts with the simulated fuel cell cathode exhaust heat recovery, integration of desorber and rectifier, integration of condenser and evaporator. The complete integrated system performance study is carried out here with different operating conditions to map out a possible operating band.

Chapter 7 discusses the validation of the models by using the obtained experimental data and then shows the improvements made to the models to fit/match the experimental data.

Chapter 8 gives an overview of the work done in the previous chapters with a summary of addressed issues, challenges faced during the experimental work and possible future work

2 Chapter 2

LITERATURE REVIEW

Perishable food items, such as; milk, vegetables, fruits and meat, among others, are transported by refrigerated trucks that keep their temperature at the desired level, and thereby delivering them in good condition and quality. Conventionally, these refrigerated trucks have a vapour compression refrigeration system on board driven by electricity generated by either the main vehicle engine or an auxiliary engine on-board [4]. The engines are fuelled by diesel, which is used to power the truck powertrain, which results in an increased fuel consumption and CO_2 emissions. The situation is worse when no auxiliary engine is installed; as when the vehicle is stationary, the main engine will have to stay in operation at a partial load to keep the goods refrigerated resulting in very low engine efficiency. The UK food chain (agricultural production, manufacturing, distribution, retail and consumption) alone accounts for about 176 Mt of CO_2 emissions annually [7]. Moreover, the conventional vapour compression systems use refrigerants that have high global warming potentials (GWP) in case of leakages; for example R134a has a GWP of 1300 as against that required by European laws of less than 150, while R404A has 4000 times the GWP of CO_2 [8]. It is estimated that 10% of the refrigerants used on trucks leak annually with Adekomaya et al. [9] reporting up to 21% annual loss for R404A. There are over four million refrigerated road vehicles worldwide [10] of which 30% each are trailers and large trucks while 40% are small trucks and vans. The UK has 172, 000 refrigerated trucks in operation, while in the US approximately 300,

000 auxiliary power unit (APU) fitted refrigerated trucks exist [11]. Refrigerated trucks are noisy due to the many moving parts in the diesel engine and the compressor itself. Hence, there are laws in some cities that restrict them from operation in the night and impose limited operational hours in the day due to increased emissions during idling [12]. On the other hand, there are no specific laws put in place as regards the use of on-board APUs but, these are also diesel engines and are noisy with even higher pollution issues as their emissions are not regulated.

In order to address some of the issues associated with conventional refrigerated trucks, researchers have been studying the possibility of employing thermally driven refrigeration/air conditioning systems on-board, by utilizing waste heat from the vehicle exhaust as the energy source. Using thermally driven refrigeration systems would reduce the electrical load on vehicle engine and enhance fuel economy. One of the thermally driven refrigeration systems that have attracted much attention for use on board of vehicles is the vapour absorption refrigeration system (VARS).

2.1Thermally activated cooling technology

Thermally activated cooling systems are those that are driven by heat rather than electricity as in the conventional vapour compression systems. The most common heat driven cooling systems are absorption and adsorption systems. The absorption process is one in which a substance (refrigerant) in one phase (gas) is incorporated or absorbed into another substance (absorbent) of a different phase (liquid) [13]. On the other hand, adsorption is one in which a solid is used to hold ions and molecules of another substance to its surface. Therefore, an adsorption process, simply put, is the separation of a substance in one phase followed by its accumulation or concentration on the surface of another substance. Besides the absorption and adsorption cooling technologies, there

are also the desiccant and ejector systems which are not as established as the absorption systems. The coefficient of performance of absorption, adsorption and ejector refrigeration systems is 0.4 to 1.2, 0.4 to 0.7, and 0.1 to 0.3, respectively. More so, ejector and adsorption refrigeration systems are applied in cases where the desired refrigeration temperature is above 0^{o}C, while absorption systems can be used for applications that requires temperatures below 0^{o}C. Furthermore, adsorption systems require large adsorbent beds that are far more expensive than the components of absorption systems. Based on the aforementioned reasons, vapour absorption refrigeration systems would be most suitable for truck refrigeration.

2.2 Vapour absorption refrigeration systems

As explained in the previous section, absorption systems use working pairs of two different phases (liquid and gas mixture) that are otherwise called refrigerant and absorbent. In VARS, there are four main components called the absorber, desorber, condenser and evaporator. The design of a VARS also depends on the working pair used which has a direct effect on number of components and complexity of the system. A VARS is one in which heat is supplied at the desorber where the solution is heated and the refrigerant evaporates flowing into the condenser cooling down to liquid releasing heat to the surroundings. The liquid refrigerant passes through an expansion valve, thereby reducing pressure before being heated at the evaporator causing a cooling effect. The evaporated refrigerant then flows back into the absorber forming a strong solution which is pumped back to the desorber for repeat of the cycle. Absorption systems are divided into single, double, and triple effect systems depending on the number of times the heat is utilized within the system,

2.3 Working fluids of vapour absorption refrigeration systems

The type of working pair (refrigerant and absorbent) defines the design, performance and selection of materials for the VARS, hence attention is given to the thermodynamic properties of the working fluids. The choice of the working pairs in some cases depends on the application, especially if the intent were for air-conditioning or refrigeration. It is extremely important to choose working pairs that are non-explosive, non-toxic and chemically stable in the solution stage (mixture). In addition they must exhibit the following characteristics [14]

- The working pair should be environmental friendly and low cost.
- Viscosity, thermal conductivity and diffusion coefficients being the transport properties should be favourable.
- The refrigerant must have high heat vaporization and concentration
- The difference between the boiling point of the pure refrigerant and mixture should be as high as possible.

There are different types of working pairs based on the refrigerant employed, hence the following sections give details of pairs as regards the major refrigerants used in absorption cycles.

2.3.1 Ammonia (NH3) refrigerant based working pairs

Ammonia is one of the most used refrigerants in VARS along with water as the absorbent due to the stability of the mixture at wide range of operating temperatures and pressures, high latent heat evaporation, low cost, low GWP, and low ozone depleting potential (ODP) [15]–[18]. Ammonia ($NH_{3)}$ has high latent heat of vaporization with freezing and boiling points of -77 and -33^{o}C,

respectively. It can easily be used in combination with other absorbents apart from water. Kaushik and Kuma [19] carried out a thermodynamics analysis of a single and double absorption refrigeration system employing two different working pairs NH_3-H_2O and NH_3-$LiNO_3$. Results showed that there was a 10% improvement in the coefficient of performance (COP) for both systems using NH_3-$LiNO_3$ working pair when compared to NH_3-H_2O [20]. It was found that the higher COP occurred at higher generator temperatures. The maximum COP was achieved at generator and evaporator temperatures of 120 and -20^oC, respectively. Another advantage of using NH_3-$LiNO_3$ was the elimination of rectifier (see Fig. 2.1) as compare to the working pair of NH_3-H_2O (see Fig. 2.2) for separation of water vapour from ammonia vapour. Sun [21] investigated the thermodynamic performance of VARS using ammonia-water (NH_3-H_2O), ammonia-Lithium nitrate (NH_3-$LiNO_3$), and ammonia-sodium thiocyanate (NH_3-NaSCN) working pairs. It was found that the system performed much better using NH_3-NaSCN, followed by NH_3-$LiNO_3$ when compared to NH_3-H_2O working pair. It was also shown that NH_3-$LiNO_3$ can be utilized for generator temperature as low as 80^oC.

Mclinden et al. [22] in their study compared the COP of a vapour absorption heat pump using NH_3-H_2O and NH_3-H_2O-LiBr as the working pairs. The authors gathered that the system's COP was better with 0.05 higher with NH_3-H_2O than the NH_3-H_2O-LiBr. Steiu et al. [23] introduced NAOH into NH_3-H_2O working pair and showed that there was not only improvement in ammonia separation at the desorber, but reduces both chiller driving temperature and rectification losses. They gathered through cycle simulation with experimental data that there was 20% COP increase as compared to the conventional NH_3-H_2O alone pair under the same operating conditions using hydroxyl separation of 99% for NAOH.

2.3.2 Water refrigerant based working pairs

In systems where water is used as the refrigerant, LiBr had been the absorbent. Water has high heat of evaporation. One of the advantages of using this working pair (H2O-LiBr) is the high boiling point temperature difference between H_2O and LiBr. Berestneff [24] carried out comparative performance analysis of a VARS using NH_3-H_2O and H_2O-LiBr solutions as working pairs. Results showed that H_2O-LiBr had lower pressure and higher efficiency, with H_2O-LiI having similar performance as H_2O-LiBr [25], [26].

Best [27] investigated the performance of a single and double effect absorption heat transformers using H_2O-carrol mixture(lithium bromide and ethylene glycol). Lee et al. [28] investigated the possibility of using alternate working pairs as opposed to H2O-LiBr solution only. They gathered that all the proposed working pairs LiBr + $H_2N(CH_2)_2OH$ + H_2O, LiBr + $HO(CH_2)_3OH$ + H_2O, and LiBr + $(HOCH_2CH_2)_2NH$ + H_2O were fairly safe for use in the system within the chosen operating range and conditions. Rosa et al. [29] carried out a modelling study on single and double effect vapour absorption heat pumps using H_2O + $CaCl_2$ and H_2O + LiCl as the working pairs with result showing that H_2O + LiCl had better performance. Antonio et al. [30]–[32] compared the performance of VARS using H_2O + CHO_2Na + LiBr, H_2O + LiBr, and H_2O + LiBr + CHO_2K as working pairs. Results showed H_2O + LiBr + CHO_2K and H_2O + CHO_2Na had higher performance than the conventional H_2O-LiBr solution based on mass transfer characteristics of water vapour absorption into LiBr and the organic salts. More so, it is less corrosive with lower density and viscosity than H_2O-LiBr.

The addition of salts into LiBr has been shown to minimize the risk of crystallization. One of such combinations is H_2O + LiBr + LiI + $LiNO_3$ + LiCl with 35^oC crystallization temperature lower

than the conventional H_2O + LiBr [33]. Its density, solubility and heat capacity were determined with the aid of empirical polynomial equations and experimentally tested using a water cooled vertical smooth tube with further simulations in sea water purification system using absorption transformers and double effect series flow chillers with no crystallization experienced [34]–[36] Alkitrate is another working pair that is made up of alkali-metal nitrate salts and water and has been proven to having a higher output temperature of about 260^oC in the absorption transformer without losing its COP as against the H_2O-LiBr solution but with limitations of the combination at low temperatures [37]–[39]. The LiBr absorbent in the H_2O-LiBr solution was combined with NaOH, KOH, CsOH and experimentally tested using a 45 kW absorption heat pump and was able to achieve a COP 2.1 [40], [41]. The measurement and correlations of the vapour pressure, heat capacity and density of H_2O-EMISE had shown that it is another alternative pair to H_2O-LiBr [42]. Saravanan and Maiya [43] carried out a simulation study on couple of working pair combinations (four binary mixtures (H_2O + LiBr, H_2O + NaOH, H_2O + LiCl), five ternary mixtures H_2O + LiBr + LiI, H_2O + LiCl + $LiNO_3$, H_2O + LiBr + $ZnBr_2$, H_2O + LiBr + LiSCN and seven quaternary mixtures H_2O + LiBr + LiCl + $ZnCl_2$, H_2O + LiBr + $ZnCl_2$ + $CaBr_2$, H_2O + LiBr + $ZnBr_2$ + LiCl, H_2O + LiBr + LiI + $C_2H_6O_2$, H_2O + NaOH + KOH + CsOH, H_2O + $LiNO_3$ + KNO_3 + $NaNO_3$, H_2O + LiCl + $CaCl_2$ + $Zn(NO_3)_2$). It was found that the pair of H_2O + LiBr + LiCl + $ZnCl_2$ had higher COP and efficiency ratio while H_2O + LiCl had better cut-off temperature and circulation ratio. Gogoi and Konwar [44] also carried out a comparative study between H_2O + LiCl and H_2O + LiBr and found that H_2O + LiCl performance was better.

2.3.3 Alcohol based working fluids

Alcohol based working fluids have high thermal stability. Yin et al. [45] compared the performance of H_2O-LiBr, TFE(2,2,2-trifluoroethanol)/NMP(*N*-methy1-2-pyrrolidone), TFE/E181(dimethyl-ether tetra-ethylene glycol) and TFE/PYR(2-pyrrolidone) in an absorption heat transformer. Results showed that H_2O-LiBr had better performance but at temperatures below 150^{o}C while TFE/NMP, TFE/E181 and TFE/PYR were better at higher temperatures of up to 200^{o}C. Simulation studies carried out by some researchers [46]–[49] had proven that trifluoroethanol (TFE)-tetraethylene glycol dimethyl ether (TEGDME) pair is a better choice than H_2O- LiBr and NH_3-H_2O in absorption refrigeration. This is because it is thermally stable up to 250^{o}C, non-corrosive, completely miscible over wide range of temperature and has low working pressures. Results showed that there was an increase of COP by 15% with TFE-TEGDME pair compared to NH_3-H_2O.

2.3.4 Halogenated hydrocarbon based working fluids

The conventional working pairs of ammonia-water and water-Lithium Bromide solutions have their own disadvantages amongst which are corrosive nature to copper, toxicity, therefore fluorocarbon refrigerants and organic absorbents have been studied as possible replacement. The performance of R21, R22, R30, R31, R133a, R124a, R134a were studied in an absorption refrigeration cycle and findings showed that R21 had higher COP but was more corrosive to copper [14]. Borde et al. [50], [51] studied the performance of R134a as the refrigerant and DMETEG, MCL, and DMEU as absorbents with results showing that they all have similar COP but R134a + DEMTEG having lowest cycle ratio. Borde et al [52], [53] further studied the

performance of refrigerants R124 and R125 when used with the absorbents DMAC, NMP, MCL, DMEU and DMETEG. It was gathered that for R124, the pair R124 + DMAC showed better performance while for R125, the pair R125 + DMEU was better.

Table 2.1 Comparative analysis of different working fluid pairs adapted from [9].

Working pair	**Absorption cycle**	**Remark**
$NH_3 + H_2O + LiBr$	Absorption refrigeration/chiller	Lower water content of vapor entering the rectifier; higher COP than ammonia-water pair
$NH_3 + LiNO_3$	Absorption refrigeration/chiller	Lower generation temperature than ammonia-water pair
$NH_3 + H_2O + NaOH$	Absorption refrigeration/chiller	Higher COP, reduced driving temperature, higher ammonia separation
$H_2O + LiBr + (CH_2OH)_2$	Absorption heat transformer	Higher solubility of about 80%, same thermal properties as $LiBr + H_2O$
$LiBr + H_2N(CH_2)_2OH + H_2O$	Absorption refrigeration/chiller	Higher viscosity, corrosion but reduced risk of crystallization than $LiBr + H_2O$
$LiBr + HO(CH_2)_3OH + H_2O$	Absorption refrigeration/chiller	Higher viscosity, corrosion but reduced risk of crystallization than $LiBr + H_2O$

$LiBr + (HOCH_2CH_2)_2NH + H_2O$	Absorption refrigeration/chiller	Higher viscosity, corrosion but reduced risk of crystallization than $LiBr + H_2O$, less heat and mass transfer coefficients
$H_2O + KNO_3$	Absorption heat transformer	Increased heat and mass transfer than $H_2O + NH_3$, Low corrosive
$H_2O + CaCl_2$	Absorption heat transformer	High COP than $H_2O + LiCl$; readily available and environmental friendly; less corrosive than $LiBr + H_2O$
$H_2O + LiBr + CH_3COOK$ $H_2O + LiBr + CH_3CH(OH)COONa$	Absorption heat pump	Readily available and environmentally friendly, suitable for moderate temperature applications than $LiBr + H_2O$
$H_2O + CHO_2Na + LiBr$ $H_2O + CHO_2K + LiBr$	Absorption chiller/refrigeration	Good thermodynamic properties, low toxicity and non-flammability
$H_2O + LiBr + LiI + LiNO_3 + LiCl$	Absorption chiller/refrigeration	Higher COP, lower generation temperature, less crossivity than $LiBr + H_2O$
Alkitrate	Absorption heat transformer	Output temperature of 260 °C without losing the COP compared with $H_2O + LiBr$; limited in low temperatures

$NaOH + KOH + H_2O$	Absorption heat pump	Significant wider solution field, higher temperature lift, better COP than $LiBr + H_2O$
$NaOH + KOH + CsOH + H_2O$	Absorption heat transformer	Higher temperature lifts and a smaller risk of crystallization; high viscosity and corrosion
$H_2O + LiBr + LiNO_3$	Absorption heat pump	An alternative to the conventional $LiBr + H_2O$ with higher COP and less corrosive.
$H_2O + LiBr + HO(CH_2)_3OH$	Absorption heat pump, Absorption chiller/refrigeration	Higher COP with lower flow rate than $LiBr + H_2O$; air-cooled; anti-crystallization enhanced by $HO(CH_2)_3OH$.
$H_2O + LiBr + LiI + HO(CH_2)_3OH$	Absorption chiller/refrigeration	Better heat and mass transfer coefficient than $LiBr + H_2O$; air-cooled.
$H_2O + LiBr$, $H_2O + NaOH$, $H_2O + LiCl$, $H_2O + LiBr + LiI$, $H_2O + LiCl + LiNO_3$, $H_2O + LiBr + ZnBr_2$, $H_2O + LiBr + LiSCN$,	Absorption chiller/refrigeration	For improved COP and flow rate.

H_2O + LiBr + LiCl + $ZnCl_2$, H_2O + LiBr + $ZnCl_2$ + $CaBr_2$, H_2O + LiBr + $ZnBr_2$ + LiCl, H_2O + LiBr + LiI + $C_2H_6O_2$, H_2O + NaOH + KOH + CsOH, H_2O + $LiNO_3$ + KNO_3 + $NaNO_3$, H_2O + LiCl + $CaCl_2$ + $Zn(NO_3)_2$		
TFE + NMP	Absorption heat transformer	Working temperature range, lower working pressure and good safety level
TFE + E181		Temperature lift over 30 °C without losing COP
TFE + TEGDME	Absorption heat pump	Lower driving temperature, higher COP than NH_3 + H_2O
R134a + DMETEG, R134a + MCL, R134a + DMEU		No rectification; non-toxic and non-corrosive

R125 + NMP, R125 + DMAC, R125 + MCL, R125 + DMPU and R125 + DMETEG	TPL	Low-potential heat-sources (70–120) for cooling and refrigeration; not toxic or corrosive; environmentally acceptable; no rectification
R124 + DMAC, R124 + NMP, R124 + MCL, R124 + DMEU, R124 + DMETEG	Absorption chiller/refrigeration	Lower COP values than R22 series, higher COP than R134a series. The working fluids based on R124 had lower *f* values; driven by low potential heat sources for sub-zero temperatures
R134a + DMAC	Absorption chiller/refrigeration	Effectively increased COP than NH_3-H_2O with a half effect cycle
Acetone + $ZnBr_2$	Absorption heat pump	Generating temperature of 50 °C
H_2O + monomethyl-amine	Absorption heat pump	Similar properties as NH_3 with lower vapour pressure

As seen from Table 2.1 and the reviewed literature it can be deduced that the most used working pairs are the ammonia-water and water-Lithium bromide solutions. This is because their application in absorption cycles have been established for long due to dedicated research and development. Hence, they have been used as the basis for further cycle improvement against other refrigerants by adding additives. Due to the freezing point of water when used as refrigerant in absorption systems, it is deployed in areas of chilled foods and air-conditioning whose refrigeration temperature is not less than 1^oC. While NH_3 based working pairs can be employed for refrigeration applications of down to -20^oC.

2.4 Vapour absorption refrigeration systems using Lithium bromide-water

In a VARS where water-Lithium bromide is used as the working pair, water is the refrigerant and Lithium-bromide is the absorbent. The H_2O-LiBr pair is mostly used in applications of chilled food and air-conditioning where the desired refrigeration temperature is above 0^oC. This is because the freezing point of water is zero hence if used for frozen food (refrigeration temperature below zero) will solidify and damage the absorption chiller and there will be no cooling effect. Figure 2.1 shows a schematic of a single effect H_2O-LiBr VARS.

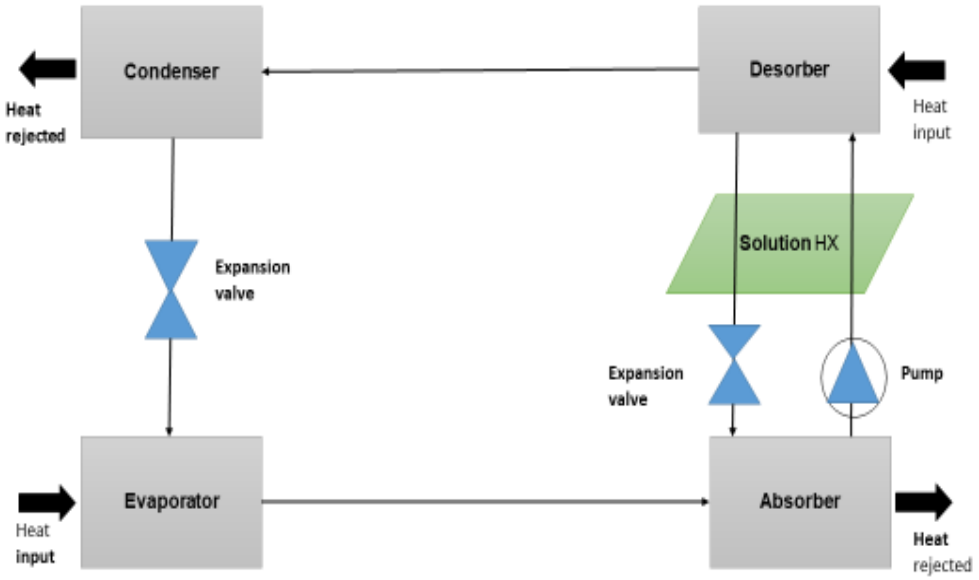

Figure 2.1 Schematic of a single effect H2O-LiBr VARS.

The H_2O-LiBr is pumped into the desorber with the aid of a pump where heat is added, and water evaporates. The evaporated water vapour flows into the condenser and cools down to liquid rejecting heat to the surrounding in the process. It then flows into the evaporator through an expansion valve that helps in reducing the pressure. In the evaporator it absorbs heat from the refrigerated space and evaporates turning into vapour and flows back into the absorber. The water vapour from the evaporator mixes with the strong solution that returned from the desorber rejecting heat to the surrounding and the mixture is pumped back into the dersorber for repeat of the cycle.

H_2O-LiBr VARS is a well-established technology that is commercially available in the market through the following suppliers: Broad, Carrier, Ebara, Entropie, Hitachi, Kawasaki, LG,

McQuay, Sanyo, Shuangliang, Thermax, Trane, Rotartica, Yazaki, and York [13], [54]–[61]. The operating temperature of the heat source for single, double and triple effect H_2O-LiBr VARS is between 80-120^oC, 120-170^oC, and 200-230^oC, respectively [62], [63].

2.5 Vapour absorption refrigeration systems based on ammonia- water

Ammonia-water VARS is one in which ammonia act as the refrigerant and water the absorbent. It is one technology that has benefited from many decades of research and development with the first U.S patent in 1860 by Ferdinand Carie for commercialization making it the oldest heat driven technology [13]. The working principle is the same as that for water-Lithium bromide VARS except for the inclusion of a rectifier for purification of ammonia vapour at the exit of the desorber. In this case, ammonia from the strong NH_3-H_2O solution in the desorber when heated by the external source evaporates. Due to the volatility of both water and ammonia, some water vapour accompanies the ammonia vapour exiting the desorber which is then separated at the rectifier and returns to the absorber with little amount of NH3 (weak solution) as illustrated in Fig 2.2. The pure ammonia vapour exiting the rectifier condenses in the condenser rejecting heat and flows through expansion valve where its pressure is reduced before entering the evaporator. The liquid ammonia evaporates after receiving heat from the refrigerated space and flows back into the absorber where it mixes with the weak solution coming from the desorber to form a strong solution, rejecting heat in the process. The strong solution is them pumped back into the desorber for repeat of the cycle. Because the desorption process in the desorber takes place at high pressure and temperature, the weak solution leaves the rectifier at high temperature and pressure. Therefore, a solution heat exchanger is placed between the desorber and the absorber through which the returning weak solution from the desorber and the strong solution from the absorber pass. In this process heat is transferred from

the weak solution to the strong solution. The weak solution at the exit of the solution heat exchanger passes through an expansion valve that reduces its pressure before entering the absorber. At the other end, a refrigerant heat exchanger is used in which the liquid ammonia leaving the condenser transfers heat to the ammonia vapour exiting the evaporator.

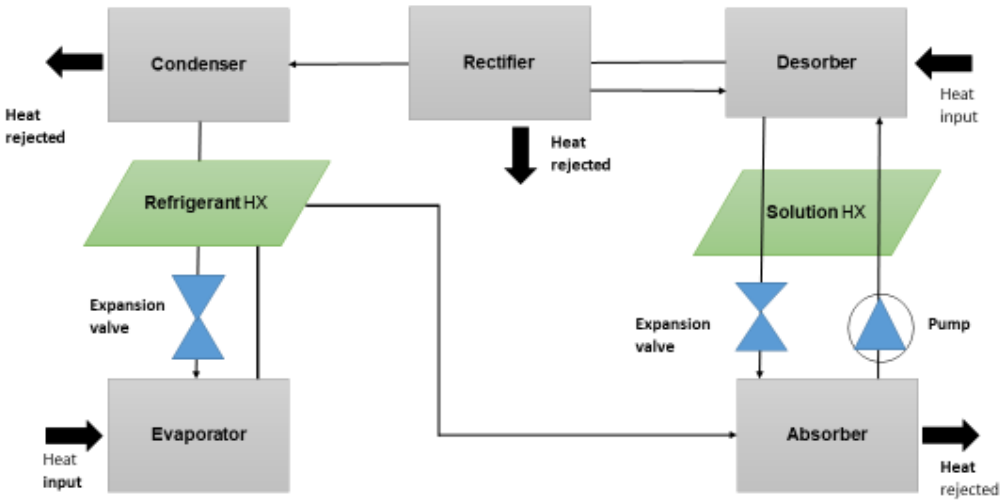

Figure 2.2 Schematic of single effect NH3-H2O VARS.

The NH_3-H_2O VARS has the following benefits: free from crystallization issues found in H_2O-LiBr VARS, ability to achieve evaporator temperatures below zero, elimination of air purge system due to operation under positive pressure, the pair is environmental friendly, more compact due to high pressure ammonia and lower specific volume. The manufacturers of NH_3-H_2O VARS are Apina, Carrier, Colibri-Stork, SolarNext, and Hans Güntner GmbH [13], [64].

2.6 Vapour absorption refrigeration system based truck refrigeration

Tremendous efforts have been made in the area of utilizing the waste heat from engine exhaust to drive VARS for refrigerated truck application through modelling and simulations. Alam [65] investigated the feasibility of integrating a ternary working pair VARS with a vehicle engine exhaust for meeting the air-conditioning need of a passenger car through modelling. Results showed that enough thermal energy was recovered from the exhaust that meets the cooling load. The performance of NH_3-H_2O based VARS coupled to the exhaust of a marine diesel engine studied in [66] showed that the desorber and evaporator temperatures increase had positive effect on the system COP. On the other hand, low condenser and absorber temperatures increased the system COP. An investigation into the coupling of the exhaust of trawler chiller fishing vessel engine with an NH_3-H_2O VARS was carried out by Fernández-Seara et al. [67]. The authors' work was based on modelling by indirectly coupling the two units using a coupling heat exchanger and thermal fluid. The thermal fluid absorbs heat from the exhaust flue in the coupling heat exchanger and transfer same to the NH_3-H_2O in the desorber at the desired temperature. They concluded that it was feasible and beneficial due to the steady operation of the trawler engine.

A simulation study in the integration of caterpillar diesel engine and VARS showed that there was enough thermal energy from the engine exhaust to cater to the cooling load requirements and cooling of the inlet air to the engine compressor [68]. A single effect NH_3-H_2O based VARS was indirectly coupled with a diesel engine to cater for small capacity load in [69] using a thermal fluid. The authors work was based on modelling and the operation of the system was both in cooling and heating modes. Results showed that a COP of 1.67 and 0.69 were achieved for heating and cooling mode, respectively based on a control strategy applied. A H_2O-LiBr

VARS was directly coupled with the exhaust of vehicle engine to study the performance and amount of thermal energy recoverable during vehicle idle times. They concluded by showing their simulation study that there was enough thermal energy available during idle times to cater for a mid-sized passenger car cooling load [70]. Direct coupling of engine exhaust and desorber of VARS causes corrosion at the desorber thereby reduces system performance with time, hence not a good idea.

Vicatos et al [71] built a prototype to test the performance of integrating an NH_3-H_2O VARS with the engine exhaust of a mini truck based on their modelling results and showed that there was enough heat to meet the air-conditioning need of the truck. An energy and exergy analysis of coupling waste heat from cooling systems and engine exhaust of electric vehicles and hybrid-electric vehicles with VARS had been carried out by Javani et al. [72]. The VARS and the HEV engine exhaust or EV cooling loop were indirectly coupled using thermal fluid and coupling heat exchanger. Results showed that there was no sufficient heat recovered to meet the air-conditioning load of the car with EV, but the HEV exhaust heat recovered was more than enough to meet the cooling load with a COP of 0.52. Results of a feasibility and exergy study of coupling a Homogenous charge compression ignition (HCCI) engine with ammonia-water VARS for combined cooling and power application carried out by Sarabchi et al. [73] showed that the highest exergy occurred in the engine and the absorber of the VARS. The VARS and the engine were directly coupling through series of heat exchangers thereby reducing the exhaust temperature to a maximum of 180^{o}C at the desorber inlet. Their study was based on modelling and simulation.

Researchers have carried out experimental work on utilizing waste heat from the vehicle exhaust to drive the VARS for either car air conditioning or refrigeration [4], [6], [74]–[81]. An experimental investigation into the feasibility of waste heat recovery from the vehicle

exhaust to drive VARS using ammonia-water as working pair was carried out by Koehler et al. [4]. They coupled the vehicle exhaust and the VARS directly with the exhaust gas temperature varied between 440 and 490^{o}C at mass flow rate of 0.1 kg/s. This method of coupling can cause back pressure effect on the engine thereby reducing the engine performance significantly. More so, direct coupling of the engine exhaust and the VARS can cause corrosion at the desorber of the VARS. The exhaust gas temperature exiting the desorber was measured to be around 180^{o}C. A cooling capacity of 6 kW was achieved at refrigeration temperature of -20^{o}C and ambient temperature of 30^{o}C, while 8 kW was achieved when the ambient temperature is reduced to 20^{o}C.

AlQdah et al. [74] coupled a diesel engine waste heat with VARS using a shell and tube heat exchanger for car air conditioning purposes. Water was used as the heat recovering fluid, flowing through the tube of the heat exchanger while the exhaust gasses flowed in the shell side in a counter-flow direction. The emphasis here was on the recoverable heat from the engine exhaust and on designing a desorber based on the available heat. It was found that an increase in the engine rpm increases its exhaust flow rate, exhaust gas temperature, heat transfer and the system COP at constant water flow rate

Talom and Beyene integrated the exhaust of a 2.8 L V6 Internal combustion engine (ICE) with a commercially available 10 kW VARS by replacing the VARS burner with a heat exchanger. They operated the VARS in a closed and open cycle at ambient temperatures between 24 and 30^{o}C for air-conditioning and refrigeration applications on transport vehicles [75]. They achieved an evaporator temperature of 12^{o}C in the former mode and 5-8^{o}C in the later. The experimental work was carried out at high engine rpms between 1800 and 2400 Hence, the insufficient heat from engine exhaust during idling and traffic periods were neglected which will negatively affect the refrigerated space temperature. They concluded with

recommendations for further work to be conducted on the system scalability, engine back pressure, cost, and refrigerant regulations.

A plenum was built around the desorber of an ammonia-water VARS coupled directly to the exhaust of an ICE with small and large flow area modes of operation by Horuz [76]. Results showed that the large flow area mode has similar fuel consumption rate, exhaust gas temperature and back pressure to the engine before coupling the VARS, while the small flow area mode has higher back pressure. This means that, the mode of operation with small flow area will reduce vehicle engine performance resulting in low refrigeration effect on the VARS. They also concluded that there isn't enough heat for refrigeration purposes during idling and traffic times and the associated cost for alternative source of heat needs be looked into. More so, the effect of increased back pressure on the engine during operation and corrosion effect on the desorber were recommended to be studied.

An ICE vehicle exhaust was directly integrated with an ammonia-water VARS, to analyse the recoverable heat from the engine exhaust, and the engine performance and its emissions, by Manzela et al. 2010) [78]. The study was based on the exhaust back pressure by controlling the percentage of throttle valve opening and thereby controlling the amount of heat supplied to the desorber of the VARS. Results show that it took the system 2 hrs 55 minutes to get into steady state cooling effect. The test showed a reduction in carbon monoxide (CO) emissions but no positive change in the carbon dioxide (CO_2) emissions. Alqdah et al [79] on his part also integrated the exhaust gases of an ICE with and ammonia water VARS. They evaluated the engine performance, the effect of exhaust flow on VARS and the emissions. COP of 0.85 and 1.04 were achieved depending on the desorber temperature which is directly proportional to the exhaust heat temperature.

An investigation into directly coupling the engine exhaust to a single effect LiBr-H_2O VARS, which was carried out by Kaewpradub et al. [80], showed promising results. The condenser, absorber and evaporator of the VARS were of the shell and coil heat exchanger type while the desorber was of spiral fin-and-tube type as shown in Fig. 3

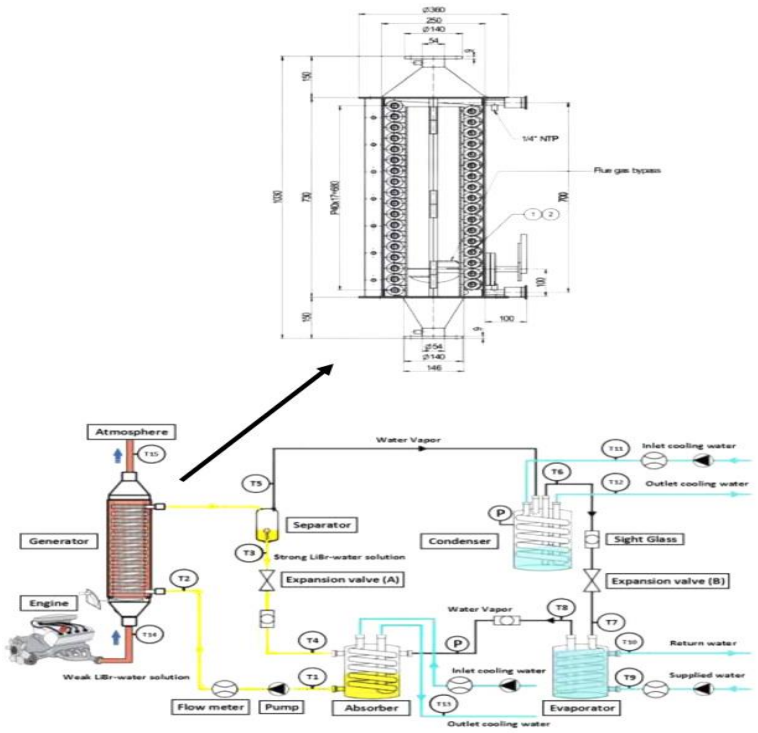

Figure 2.3 Schematic diagram of engine exhaust coupled VARS test bench [80].

In the desorber, the exhaust gases flowed through the shell side while the LiBr-H_2O solution flowed in the coiled tube. A cooling capacity of 700 W was achieved with a COP of 0.275 at a condenser outlet temperature of 25^oC. They found that crystallization of LiBr-H_2O solution at the desorber outlet occurs at engine rpm of 1600 and above which will stop system operation due to no flow, while there was no sufficient heat to cause evaporation at rpm below 1200. Hence, the tests were carried out at engine rpm between 1200 and 1400. This is not practically achievable as the engine rpm would be below 1200 during traffic and idling resulting in insufficient heat for refrigeration.

The transient performance of an ammonia-water-hydrogen diffusion absorption refrigeration system (DARS) utilizing heat from an ICE exhaust gases and electric heaters as energy sources was studied by Adjibade et al. [6]. The exhaust of the internal combustion engine was directly coupled to the desorber of the absorption system with two censored valves regulating the amount of heat input to the desorber and that rejected to the surrounding. The desorber was a double pipe heat exchanger where the outer tube is directly heated up by the exhaust gas which transfers the heat to the solution flowing in the inner tube. Results showed that, 40 sec and 180 sec were required to heat up the DARS using exhaust gases and electric heating respectively. Furthermore, it took 2 hours for the exhaust to reach a steady state temperature of 3^{o}C at the evaporator and 7hrs for the electric heater. It was found that a minimum temperature of 140^{o}C is required at the desorber for the cooling effect to start taking place at the evaporator. Using the same DARS, Aly et al. [81] were able to achieve a refrigerated temperature of between 10 and 14.5^{o}C in 210 minuteswhen the engine was operated at 1750 rpm. A maximum of 9% waste heat was recovered by the system and a COP of 0.10 was achieved. A minimum refrigeration temperature of 10^{o}C was attained at exhaust gas temperature of between 215 and 230^{o}C.

2.7Discussion

From the above literature on modelling/simulation and experimental studies, the following problems were deduced: (i) back pressure effect on vehicle engine performance, (ii) corrosion effect on desorber of VARS due to direct coupling of the exhaust to VARS, (iii) not enough heat from the engine during idle and traffic periods, (iv) noise from the vehicle engine or the alternative diesel generator on board with associated greenhouse gas emissions.

In a bid to addressing most of the problems encountered on the use of vehicle engine exhaust heat as energy source for VARS, researchers have explored the use of the exhaust heat from a fuel cell as the energy source to drive VARS [82]–[94]. A fuel cell is an electrochemical device that converts the chemical energy in fuel into electricity and heat without the combustion process. They are quiet due to the absence of moving parts with potentially zero emissions at the point of use depending on the fuel used. Fuel cells are categorised into low and high temperature types. The low temperature types operate in the temperature range of 60-200^{o}C, and the high temperature types are in the range of 600-900^{o}C. If a high temperature fuel cell is used as an APU on board of a refrigeration truck, the high temperature cathode exhaust heat from high temperature fuel cells can be harnessed and used as an energy source for VARS. This will reduce the electric load from the vehicle engine. On the other hand, by decoupling the source of heat from the engine, there will always be sufficient heat even during idling and low speed conditions, and no emissions and noise associated with the refrigeration on the truck. Moreover, the electricity generated from the fuel cell can be used to power the cabin air conditioning system and other auxiliary electrical loads including vehicle battery charging.

Compact thermally driven refrigeration systems are scarce with no experimental work on fuel cell-VARS refrigerated trucks. A detailed modelling study, which was carried out by Venkataraman et al. [86], shows the feasibility of the use of SOFC cathode exhaust heat to drive VARS for refrigerated truck applications. Their systematic modelling work used an internally finned double pipe heat exchanger to indirectly couple the two units (SOFC and VARS) by using thermal oil as the heat transfer fluid due to the units' different operating temperature levels. They started with modelling the single components and finally analysing the entire system configuration. The results showed that 80% overall system efficiency is achievable.

A thorough review of engine exhaust and fuel cell exhaust heat coupled VARS was carried out by Venkaraman et al [95]. They concluded that the benefits of using fuel cell exhaust heat powered VARS outweighs that of the engine exhaust powered VARS for refrigerated transport application.

Apart from the study carried out by Venkataraman et al. [86] for use of fuel cell and VARS for refrigerated truck application, all other fuel cell-VARS integration studies [82]–[85], [87]–[94] have been mainly for residential applications and therefore not discussed here. A comparative study of coupling SOFC (in parallel and series modes) with VARS for refrigerated transport application was also carried out by Bhargav et al [96]. Their simulation study focused on the thermos-economic performance of the SOFC in the two different configurations as shown in Fig. 4 for optimisation of the SOFC sub-system layout. Results showed that the parallel configuration requires 45-65% lower number of SOFC cells to meet a targeted refrigeration load as opposed to the series.

a

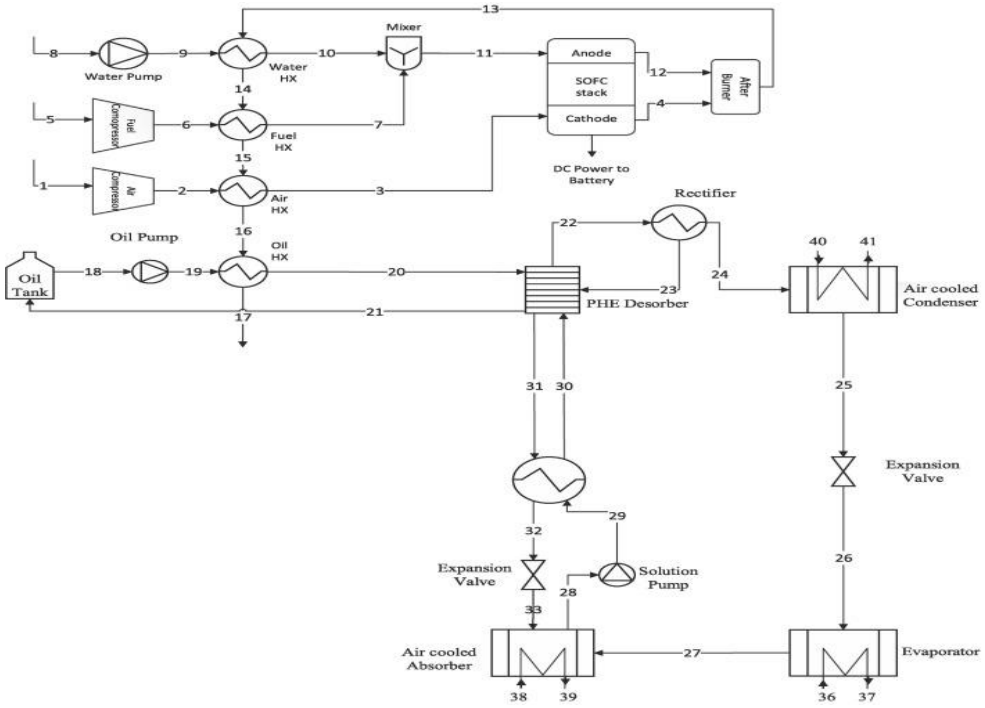

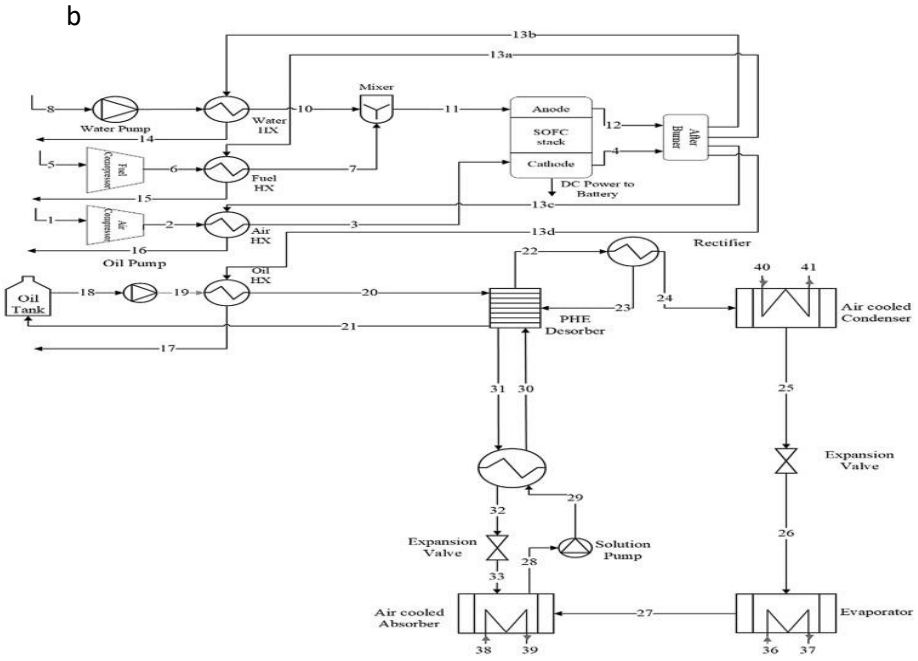

Figure 2.4 SOFC-VARS system layout: (a) series configuration (b) parallel configuration [96].

Experimental studies on coupling of SOFCs with VARS for refrigerated trucks has not been in the public, thus more data is required to prove the feasibility of the concept. This is the main purpose of this study and the novelty behind the work. However, a demonstration project using fuel cell as auxiliary power unit (APU) on truck refrigerated units have been carried out successfully in the USA [97]. The project was sponsored by the department of energy (DOE) with Nuvera Fuel Cells, Thermo King, Ballard Power, Zen Clean Energy, Carrier Transicold, and Walmart as partners, The complete system was successfully demonstrated for 8 hours in 2018.The fuel cell used was 25 kW_e stack from Nuvera mounted at the belly of the TRU with a 10 kg hydrogen tank. The demonstration was carried out at refrigerated temperature set point of 1 and -20^oC and were met at average inverter power of 12.5 and 12.11 kW.

From the foregoing, it will be more efficient to use a high temperature fuel cell (SOFC in particular) to drive VARS and still use the available electricity from the fuel cell for auxiliary load on the truck. More so, since the evaporation temperature for refrigerated trucks in most cases will be below zero, the VARS will be ammonia-water based as the H_2O-LiBr is for air – conditioning purposes and chilled food above zero degree.

3 Chapter 3

SYSTEM DESCRIPTION AND EXPERIMENTAL SET UP

The integration of high temperature fuel cells, such as SOFCs, with a thermally driven vapour absorption refrigeration systems (VARS) to utilise the waste heat from the fuel cell to provide air-conditioning or refrigeration alongside side heating and domestic hot water is an attractive concept. Such an integrated system is called Combined Cool, Heat and Power System (CCHP). However, the temperatures required at the inlet of the VARS (desorber) are between 120^{o}C and 240^{o}C depending on the type of chiller (single, double, or triple step) and the refrigerant-absorbent pair used [98], while waste heat from SOFCs is generated at much higher temperatures. Therefore, direct coupling of the two systems is not possible as it may cause boiling in the desorber of the VARS resulting in low or inefficient performance. Venkataraman et al. carried out detailed system modelling and simulation of indrectly coupling of SOFC with an NH_3-H_2O working pair in a single step VARS. Thermal oil was used as the heat transfer fluid for coupling as shown in Fig.3.1 which forms the basis of this work [86].

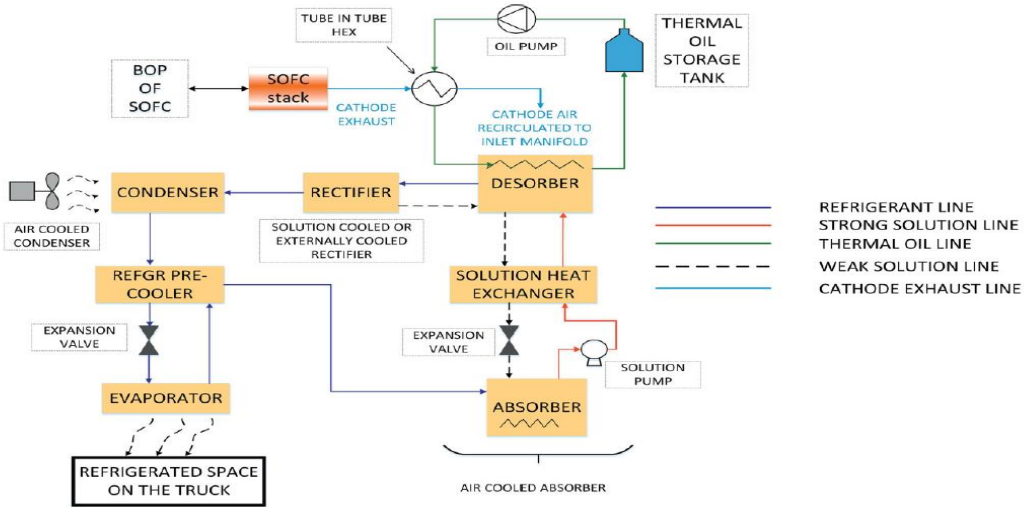

Figure 3.1 Schematic of SOFC-VAS integration [86]

The coupling is made possible using an internally finned double pipe heat exchanger (DPHX) in which the SOFC waste heat, carried by the exhaust air, flows in the shell side while a thermal oil flows through the annulus. The thermal oil is heated up to the desired temperature in the DPHX and flows into the desorber of the VARS where heat is transferred to the strong NH_3-H_2O solution (rich in ammonia concentration) resulting in the ammonia evaporating. The evaporated ammonia is not 100% pure as there might be water vapour accompanying it; hence a vapour separator or rectifier is used. The pure ammonia vapour leaving the rectifier then flows into the condenser where it cools down and condenses into liquid by rejecting heat to the surrounding. The liquid ammonia leaving the condenser is further cooled down in a refrigerant pre-cooler where heat is transferred to the ammonia vapour leaving the evaporator. The cold liquid ammonia flows through an expansion valve during which the pressure is reduced before entering the evaporator. In the evaporaor, the liquid ammonia gains heat from the refrigerated space and evaporates thereby causing the cooling effect. Now, the hot ammonia vapour leaving the evaporator gains more heat from the refrigerant precooler before entering the absorber

where it mixes with the weak solution (poor in ammonia concentration) coming from the desorber to form a strong solution which is pumped back to the desorber for a repeat of the cycle.

A test rig was built in the laboratory to verify the model and demonstrate the feasibility of the practical integration of the system explained above. The performance of the complete systems is studied based on the design and operating conditions.

3.1Experimental test rig description and set up

There is need to investigate the performance of the integrated system (SOFC-VARS) by carrying out experimental work to validate the modelling studies. The outcome of the experimental study will be used to modify the models and make amendments. This section gives a detailed description of the test rig used in the laboratory for the study and the test procedures followed. Stainless steel parts were used for all components in contact with ammonia to elevate any corrosive effect of the ammonia (refrigerant). With this in mind, the rectifier, desorber, solution tank, condenser and the piping into and out of these components were made of stainless steel. Fig. 3.2 shows a schematic of the test rig.

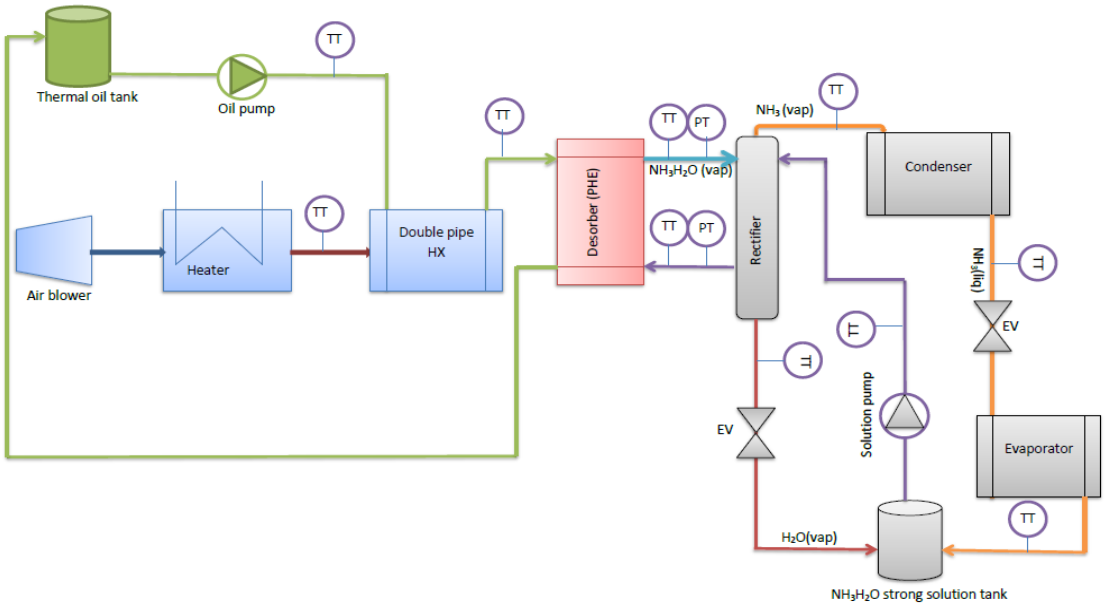

Figure 3.2 Schematic of the test rig

An air blower was used on the test rig to simulate the exhaust flow rate of the SOFC cathode. The air is passed through an electric heater to increase its temperature to replicate that of the SOFC stack exhaust. The heated air is passed through an internally finned double pipe heat exchanger where it transfers heat to the thermal oil flowing through the annulus. Hereby, the thermal oil is heated to the desired temperature of 200°C which is the required inlet temperature for the desorber of the VARS.

A plate heat exchanger is utilised as a desorber. The hot oil flows through the desorber on one side while the strong ammonia-water solution is pumped into the other side of the desorber by a variable speed diaphragm pump, transferring the heat from the oil to the NH_3-H_2O solution. The process makes the ammonia in the strong solution to evaporate and flows into the vapour separator (rectifier) where any accompanying water vapour is removed and is flowed back to the absorber. The refrigeration cycle continues as explained in the previous section. Fig. 3.3

shows the experimental test rig. A cylindrical tank of about 20 litres in volume is used as the absorber in which the ammonia-water solution is stored.

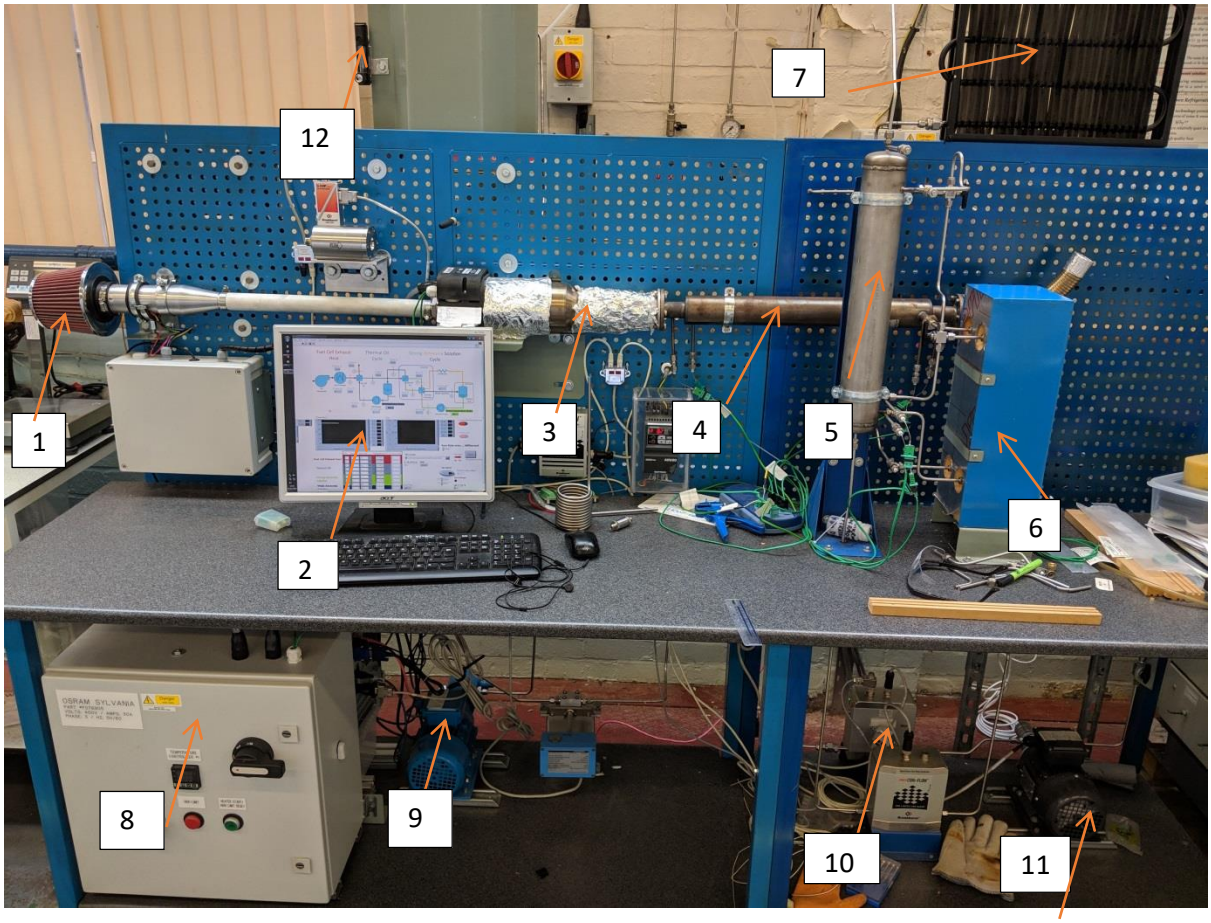

Figure 3.3 Experimental prototype of simulated SOFC cathode exhaust and VARS.

1- Air blower/compressor, 2 - Computer for data recording and visualisation, 3 - Electric heater, 4 - Internally finned double pipe heat exchanger, 5 – Rectifier, 6 – Desorber (Plate heat exchanger, PHE), 7 – Condenser, 8 - Heater control, 9 - Oil pump, 10 - Coriolis flow controller, 11 - Solution pump, 12 - Oil tank.

3.1.1 System component description

The air blower is a turbo-compressor with rated power of 1 kW and maximum flow rate of 55 g/s supplied by celeroton. The blower is connected to a SureHeat MAX electric heater (model F074729) by SYLVANIA with rate power of 10 kW and maximum temperature of 649ºC. A variable speed oil pump (ECHTOP MS 711-2) is employed in pumping the oil from the oil tank into the annulus of the coupling heat exchanger (DPHX) and back to the tank. The DPHX was manufactured by EBZ with series ID HX-GW-D1.2-01. Figure 3.4 shows the drawing of the heat exchanger.

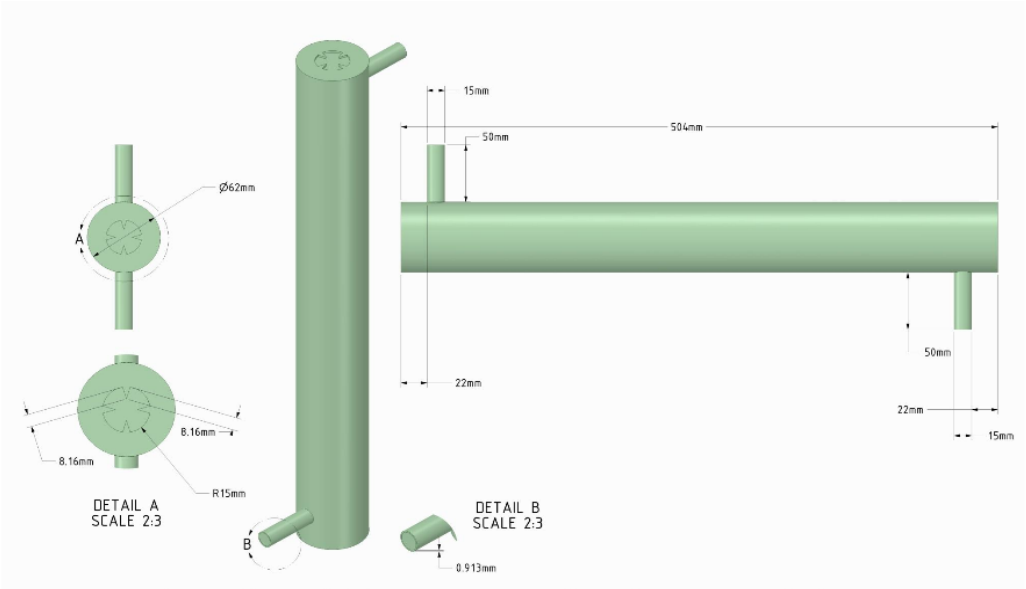

Figure 3.4 Engineering drawing of the tube-in-tube heat exchanger [3]

The hot oil flows through the desorber on one side while the ammonia-water solution is pumped into the desorber on the other side by a variable speed diaphragm pump (ECHTO MS 711-2). Heat is transferred from the oil to the NH_3-H_2O solution in the desorber causing ammonia to evaporate. Type K thermocouples are installed at the inlet and outlet of each component, i.e.

condenser, air and oil inlet, and outlet of the DPHX, the rectifier, and the desorber, which allows measuring the temperatures at these points to be used for the analysis. The mass flow rates of the oil and strong solution were measured with RHM03-T2-P1-PM0-M0-G1-N flow transmitter model supplied by Bronkhorst.

The rectifier is a helical coiled tube heat exchanger which was manufactured by EBZ. The heat of the ammonia vapour flowing in the upward direction (parallel flow) is transferred to the solution before it enters into the desorber. This process helps to increase the strong solution temperature before entering the desorber, thereby acting as both the vapour separator and solution pre-heater. This drastically reduces the cost of installing a solution heat exchanger and improves compactness.

The pumps and turbo-compressor could be manually controlled by their accompanying software and data recorder, however a data acquisition LabVIEW interface was developed and used. LabVIEW is National Instrument software which makes it possible for the user to write codes, to communicate with the hardware and to record experimental data. Fig. 3.5 shows the interface window used for controlling the system. The mass flow meters, thermocouples and controls are interfaced with the software through an RS232 with the aid of a USB adaptor.

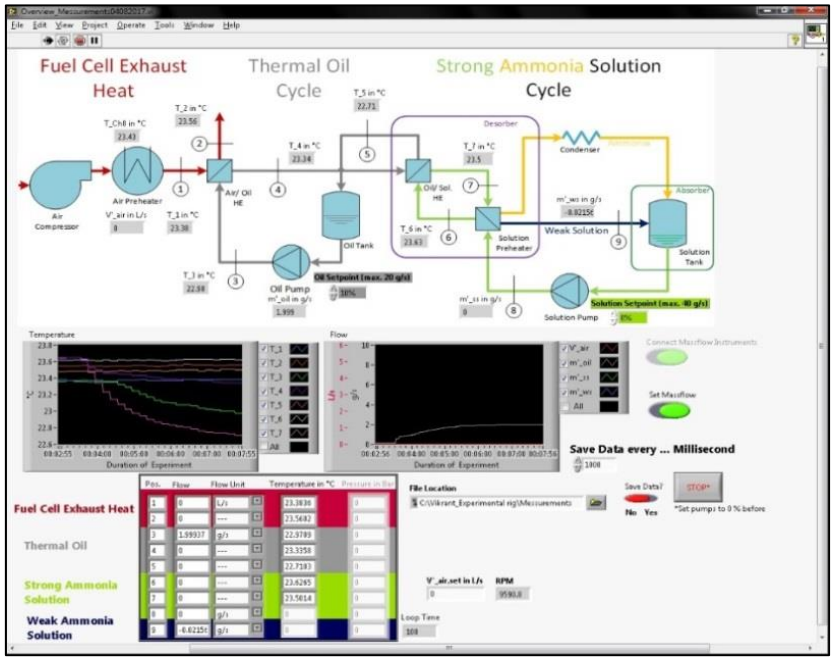

Figure 3.5 Front panel/user interface of LabVIEW for overall monitoring and control of test rig.

A U-coiled stainless tube with aluminium fins is used as the condenser while the evaporator is made from stainless steel formed into ring. The condenser is on the high pressure side after the rectifier while the evaporator is on the low pressure side after the condenser. There are two controllable electronic expansion valves (Carel E2V05BS000) operated by means of pulse-width modulation installed one each after the condenser and rectifier. The high pressure ammonia liquid exiting the condenser first passes through the expansion valve which helps in reducing the pressure to lower pressure before it enters the evaporator. While the separated water vapour from the ammonia exiting the rectifier passes through another expansion valve where its pressure is reduced before entering the absorber and mixes with the low pressure ammonia vapour exiting the evaporator to form a strong solution. Therefore, the high pressure

side consists of the desorber, rectifier and condenser, while the low pressure side is made up of the evaporator and absorber

3.2 Experimental Plan

The aim of the experiments is to validate the modelling and simulation results. The overarching goal here is to build a functional test rig demonstrating a compact and small scale VARS integrated with an SOFC and managed by a control system. The experiments are taken in steps to validate and calibrate the individual components and finally incorporated all together for the final system test and analysis. Based on this, the experimental procedures are divided into small test groups and this section gives details of each step taken.

3.2.1 Waste heat recovery through double pipe heat exchanger

The first part of the experiment is to harness the waste heat from the fuel cell cathode by using the thermal oil flowing through the annulus of DPHX while the hot cathode exhaust through the shell side. For a VARS, the temperature of the heat that can cause vaporization of the refrigerant at the desorber is between 140-240^{o}C. Since the temperature of the SOFC is between 600-900^{o}C a thermal fluid is used here which is heated up to the required temperature range in a double pipe heat exchanger and flows into the desorber where it transfers the absorbed heat to the strong solution and causes separation of the refrigerant and absorbent. By doing so, the high temperature SOFC cathode exhaust heat is coupled indirectly with the VARS using thermal oil. The aim here is to transfer the required heat to the desorber by the thermal oil at a temperature range of between 140-240^{o}C. Figure 3.6 shows a schematic of the first part of the experiment.

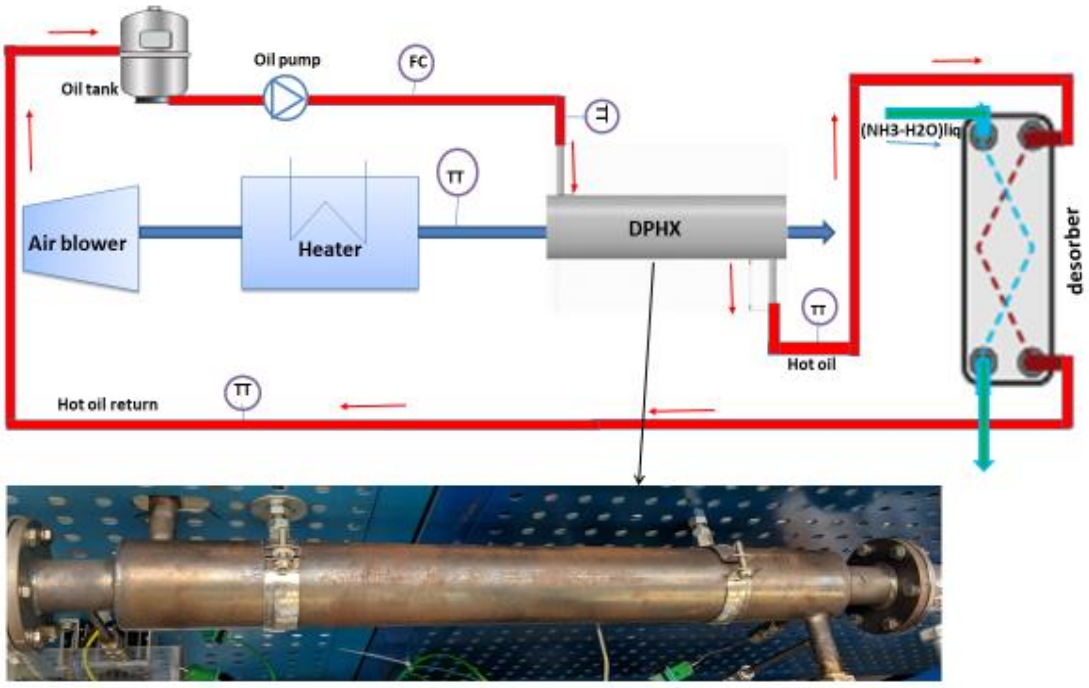

Figure 3.6 Piping and instrumentation diagram of test rig for heating thermal oil.

The controlled variables were the air and oil mass flow rates by varying the rpm of the air blower and the oil pump speed respectively through the computer interface. These in turn changes the air and oil inlet and outlet temperatures at the double pipe heat exchanger. The air blower operating range is 180K rpm and was varied in steps 500 rpm every 1 minute while the oil flow rate was varied between 1 and 16g with incremental steps of 2g/5minutes.

The desired results and purpose of this part of the experiment are as follows

i. Characterise the correlation between the air flow rate, the heat captured in the air stream and the temperature at the heater outlet.
ii. Determine the relationship between the oil outlet temperature and oil mass flow rate to find the required conditions to achieve the desired oil outlet temperature.

iii. Measure the time required to heat the thermal oil to the desired temperature which will help in analysing the start-up operation of the system and also for dynamic/transient modelling.

iv. The mass flow rate and temperature of air needed for transferring the required amount of heat in the heat exchanger.

v. The temperature gained by thermal oil (of different mass flow rates) in one pass through the heat exchanger and to verify the results with simulation.

vi. Characterize and correlate air flow rates with SOFC stack size and fuel utilisation factor

Operational procedure of the test rig for heating the thermal oil

In order to carry out a successful experiment the following steps were followed in operating the test rig:

a. The required power supply for this part of the experiment was first turned on.
b. The air blower was then turned on and the rpm of the air blower increased in steps of 500 so that the compressor reaches the desired rpm when heated will give the heater maximum temperature of 649^{o}C that replicates the SOFC's cathode exhaust temperature. It was then allowed to run for about 3 minutes to attain steady state.
c. the heater is then turned on to heat the air thereby mimicking the fuel cell cathode exhaust
d. The hot air is passed through the DPHX and vented out from the other end of the heat exchanger.
e. The oil pump is turned on and the mass flow rate of thermal oil is increased in steps of 1 g/s. The oil flow rate at which the oil temperature gets to 200^{o}C and the time it takes to reach the desired temperature are recorded.

The system was allowed to run at the new air and oil flow rates for about 10 minutes and the inlet and outlet temperatures of the air and oil in the heat exchanger were recorded. Moreover, the mass flow rates of the air and thermal oil were also recorded for the calculation of the heat transfer rate and overall heat transfer coefficient.

3.2.2 Integration of thermal oil with desorber and rectifier of the VARS

This is the second part of the experimental work aimed at integrating the heat from the thermal oil gained from the hot cathode exhaust air with the desorber. The purpose of the experiment is to use the gained heat to heat the strong solution in the desorber thereby evaporating the ammonia from the solution. A schematic of the heat integration with the desorber and rectifier is shown in Fig. 3.7

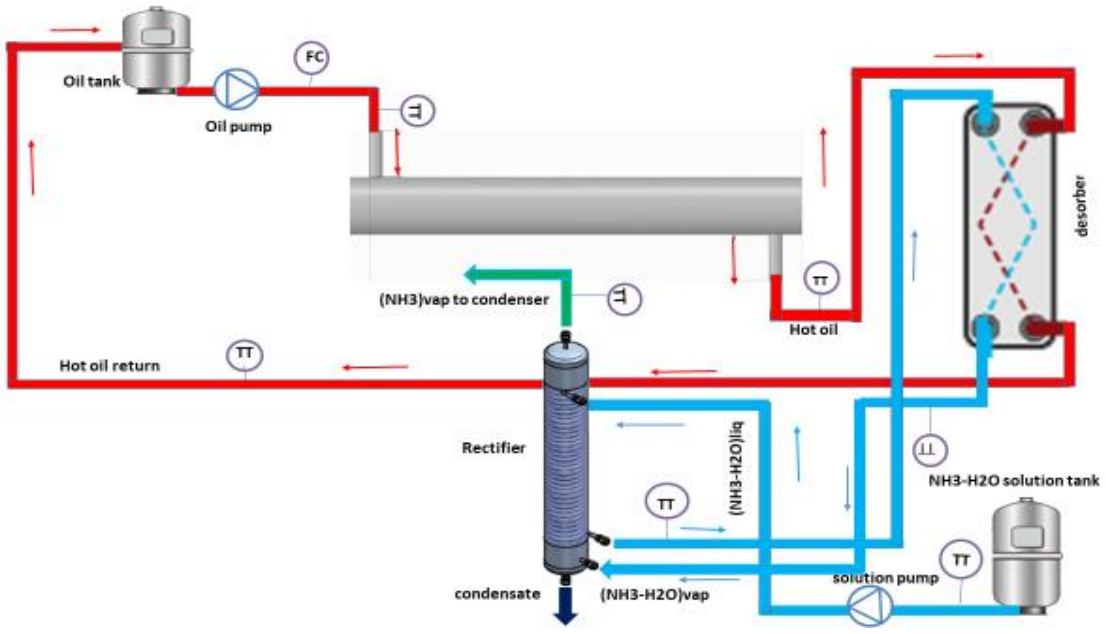

Figure 3.7 Schematic of integrating hot thermal oil with desorber and rectifier

The main results from the experiment are to determine the quantity, quality, temperature and pressure of the ammonia produced at the exit of the desorber. This is achieved by calculating

the heat transfer rate from the cathode exhaust to the thermal oil using the temperatures, mass flow rates and specific heat capacities. The results are compared with the modelling results for modification and validation. More so, the time required for producing the required quantity of ammonia vapour and that taken to reach steady state conditions is recorded. This will help in determining the start-up time needed for the system and also help in dynamic operation analysis.

Operational procedure for the integration of the hot thermal oil and desorber

With the thermal oil been heated up in the first part of the experiment, the strong NH_3H_2O solution pump is turned on to circulate the solution from the absorber into the desorber. This is achieved by first passing the solution through the rectifier to pre-heat before flowing into the desorber. The system is allowed to run for some time to allow the solution temperature at the exit of the rectifier to increase to a reasonable level; say 140^oC as identified from the simulation study. When the system attains a steady state condition, the temperatures at the inlet and outlet of the desorber, mass flow rates of the solution and oil at which the desired temperature was attained are recorded. More so, the temperatures at rectifier inlet and exit and mass flow rates of strong solution, ammonia vapour and vapour are recorded. The solution flow rate is between 1 and 8g with incremental steps of 1g every five minutes. These data will help in calculating the heat transfer rate, overall heat transfer coefficient and effectiveness of the desorber. It will also be used to determine the quantity and vapour quality of the ammonia leaving the strong solution and the time taken.

3.2.3 Integration of the condenser an evaporator in VARS

The condenser and evaporator are important components in the VARS and their integration to the system is carried out and analysed here. When the pure ammonia flows into the condenser from the rectifier it is cooled down rejecting heat to the surrounding and liquid ammonia is formed. The liquid ammonia passes through an expansion valve and its pressure is reduced in the process before entering the evaporator where the cooling effect takes place.

The mass flow rate of the pure ammonia in the condenser depends on the flow rate of at which it leaves the rectifier. The quality of the ammonia formed and quantity in the condenser also depends on the temperature of the solution leaving the desorber before entering the rectifier. This is related to the mass flow rates of both the strong solution and thermal oil. The amount and quality of pure ammonia in the condenser depends on the quantity of heat from the thermal oil supplied at the desorber, in that the higher the heat input the higher the ammonia desorption. This in turn will have a direct effect on the cooling process at the evaporator, the more the ammonia in the condenser the more the cooing effect at the evaporator. Therefore, the controllable parameters in this section are the mass flow rate of the ammonia and the cooling fan speed at the condenser. The parameters to be measured here are the inlet and outlet temperatures of ammonia at the condenser and evaporator, mass flow rate of ammonia and pressures.

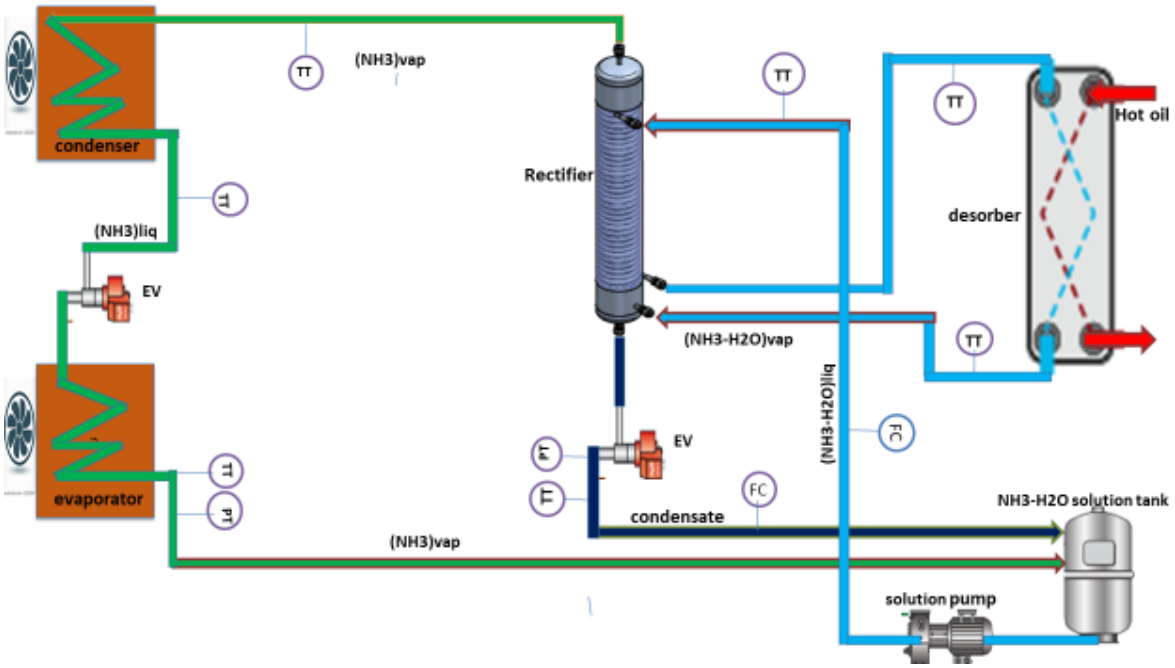

Figure 3.8 Schematic of test rig with integrated condenser and evaporator

When the liquid ammonia exiting the condenser flows through the expansion valve, it reduces in pressure before entering the evaporator where it gains heat from the evaporated space and evaporates. The evaporated space reduces in temperature to the target value set on the controller thereby causing a cooling effect. The system is allowed to run for about 10 minutes to attain a steady state and the pressure, temperature and flow rate of the ammonia vapour leaving the evaporator is recorded. The flow rate of the ammonia vapour leaving the evaporator is assumed to be the same as the ammonia liquid entering the evaporator. The oil and strong solution flow rates at which the desired cooling load is achieved are also recorded. These data will help in determining the evaporator capability in delivering a target cooling load. It will also help in investigating the entire VARS performance.

Following the successful components analysis of the VARS the whole system will be operated and its behaviour under dynamic operations will be studied and the CoP ascertained. First, the fuel cell exhaust flow rate will be varied and its effect on the heat transferred to the thermal oil, the heat input at the desorber, ammonia desorption at desorber, and cooling temperature at the evaporator will be determined. The temperatures and mass flow rates at all the components will be recorded. This will be followed by the variation of the thermal oil and the effects on the whole system determined by recording same parameters as those during the exhaust flow rate variation. Thirdly, the mass flow rate of the strong solution will be varied and all parameters as before will be recorded as well. Based on the recorded parameters, judgement will be made to determine the best operating conditions of the complete system at which the higher cooling is observed and COP.

4 Chapter 4

VAPOUR ABSORPTION SYSTEM COMPONENTS MODELLING

There is a steady growth in the population of the world which will inevitably increase the demand for energy, a major part of which will be for refrigeration and air-conditioning. As population growth will increase the demand for food, more attention is being given to the value chain ranging from production, processing and safely and qualitatively transporting same to the end user. This will inevitably increase global warming issues that are caused by the over dependence on fossil fuel for power generation and transportation. The major conventional systems used in refrigerated transportation emit greenhouse gases that contribute to global warming, as a result policies are being put in place that pose restrictions on refrigerated trucks. These are mostly operated by diesel engines even when the vehicle is at idle, emitting greenhouse gases and noise as they have to keep running in this idle condition to keep the temperature of the product at the desired level. Due to a lack of environmental legislation applying to these engines they are therefore by far noisier and more polluting than the main engines of the vehicles. On the other hand, electric driven air-conditioning (AC) systems also are powered by the same conventional systems that cause global warming. Due to the continued rise in outdoor temperatures there will certainly be an increase in electricity demand as most AC systems are powered through the conventional means with its adverse effects on the environment in terms of noise and greenhouse gas emission.

The vapour absorption system is made up of various sub components including absorber, desorber, rectifier, condenser and evaporator. This chapter is dedicated to the detailed

modelling of the rectifier, absorber, and the double pipe heat exchanger for coupling the SOFC and the VARS.

4.1Mathematical modelling of an internally finned double pipe heat exchanger

The overwhelming part of the worldwide cooling refrigeration is produced by electrically driven vapour compression systems (VCS). On the refrigerated trucks, the electricity is produced by so called Auxiliary Power Units (APUs) in around 90% of vehicles. They are equipped with small diesel engines that are not subject to any environmental legislation. The use of fuel cells to produce the electricity would dramatically reduce noise and pollutants. On the other hand, using waste heat from high temperature fuel cells like Solid Oxide Fuel Cell (SOFC) to drive a Vapour Absorption refrigeration system (VARS) will also increase system efficiency. In this way, the electricity produced from the fuel cell could be used for appliances on the vehicle and the waste heat, which is free in a sense used for refrigeration. As fuel cells are environmental friendly, this method will reduce the emission of greenhouse gases, the demand for conventional electricity production, and noise pollution. The exhaust temperature of the waste heat from SOFC or other high temperature fuel cells is between 600^{o}C and 900^{o}C while the temperature of heat needed at the desorber of VARS is between 120 and 240^{o}C. Therefore, there needs to be a medium to couple these two systems of different temperature levels. Double pipe heat exchangers can work well for this purpose with fuel cell exhaust flowing through inner tube and heat transfer fluid (thermal oil) through the annulus (inner tube).

Various works on modelling, simulation and experiments have been carried out using double pipe heat exchangers with the conclusion that internally finned types are more effective in heat

transfer [99]. Genetic algorithm and finite element methods have been used by Fabbri [100] to study the performance optimisation in terms of heat transfer of an internally finned tube heat exchanger. Kundu and Das [101] used an analytical approach to study the thermal performance of three types of fins in a tube, namely; longitudinal fin, spine and annuli fin, all of which are straight tapered. Results showed that the heat transfer coefficient largely influenced the fin efficiency. Using fluent software Rout et al. [102] utilised finite volume method in analysing the characteristics of an internally finned tube heat exchanger with different fin shapes, sizes and numbers.

Assuming a fully developed laminar flow in internally finned tubes, Tien et al [103] developed discretised two dimensional equations. The numerical equations were solved iteratively to analyse the flow behaviour in terms of velocity, temperature and heat transfer rate. The rate of heat transfer with respect to design parameter variation was also investigated. It was gathered that, the heat transfer rate increased with an increase in the number of fins but a large pressure drop was caused. They also found that there was a maximum Nusselt number of about 0.8 of the dimensionless fin height when the number of fins was less than 14. Experimental work was carried out to validate the numerical analysis using a counter flow type heat exchanger with hot and cold water running through the inner and outer tube, respectively. An analytical analysis of a fully developed laminar flow in internally finned tube was carried out by Hassan et al. [104]. They categorised the flow regions into two for which velocity profiles were studied with respect to boundary conditions and influence of design parameters.

Sreedhar and Varghese [105] investigated the heat transfer rate and overall heat transfer coefficient of an internally finned double pipe heat exchanger numerically, using the logarithmic mean temperature difference method. The authors used Fluent 6 for the numerical analysis with the fins studied in different positions viz: external fins on inner tube, tube without

fins, internal and external fins simultaneously on the inner tube, and inner tube internally finned only. Results from the modelling work showed that the rate of heat transfer and overall heat transfer coefficient was higher on the one with external fins on the inner tube. It had an overall heat transfer coefficient of about 60.5% increase compared to the base case with no fins. In conclusion, they stated that fins on the outside of the inner tube were the best design if the hot fluid flowed in the inner tube with the cold fluid in the annulus with intension to cool down the hot fluid, but the fins on internal part of the inner tube were best if the hot fluid is to heat up the cold fluid.

Indhe et al. [106] performed an experimental investigation into the optimisation of a longitudinal fin profiles for double pipe heat exchangers. It was found that heat transfer was enhanced by 26% as compared to an un-finned tube. Tang et al. [107] experimentally investigated the performance of finned tube with crimped spiral fin, plain fin, slit fin, fin with delta-wing longitudinal vortex generators, and mixed fins of vortex generator type and slit fin type. Results showed that a crimped spiral finned tube had the highest values of heat transfer but also pressure drop.

In order to understand the performance of a double pipe heat exchanger as used in coupling the SOFC and VARS a detailed design/modelling is presented in the following. The design of the double pipe heat exchanger is delicate as it is the key component that will make possible the coupling of high temperature fuel cell exhaust heat with the VARS. In this design, thermal oil is used as the heat transfer fluid flowing in the annulus while the fuel cell exhaust air flows in the finned inner tube. As the hot cathode exhaust fluid flows through the double pipe heat exchanger, it heats up the thermal oil in the annulus which in turn will pass the heat it gains to the desorber of the VARS. Table 4.1 gives the design details of the heat exchanger.

Table 4.1 Design parameters of the internally finned double pipe heat exchanger.

Parameter	Value
Fin height H_f (mm)	8
Fin thickness δ_f (mm)	4
Number of fins N	4
Length of finned tube L (mm)	500
Outer diameter of inner tube d_o (mm)	34
Inner diameter of outer tube d_i (mm)	57

The heat transfer rate in the heat exchanger on the oil and air side respectively is determined by Eq. 4.1 and 4.2

$$Q_O = \dot{m}_0 C_{po} \Delta T_o \quad \text{Eq. 4.1}$$

$$Q_a = \dot{m}_a C_{pa} \Delta T_a \quad \text{Eq. 4.2}$$

with ΔT_o and ΔT_a given as

$$\Delta T_o = T_{oo} - T_{oi} \quad \text{Eq. 4.3}$$

$$\Delta T_a = T_{ai} - T_{ao} \quad \text{Eq. 4.4}$$

Where

C_p specific heat capacity

T_{oi}, T_{oo} Oil inlet and outlet temperatures (K)

T_{ai}, T_{ao} Air inlet and outlet temperatures (K)

$\dot{m}$ mass flow rate of the fluids.

The overall heat transfer cofficient was determined with Eq. 4.5

$$U_o = \frac{Q_o}{A_{total} LMTD} \quad \text{Eq. 4.5}$$

Where U_o, A_{total}, and LMTD, are the overall heat transfer coefficient, total heat transfer area, and logarithmic mean temperature difference respectively. The LMTD term is calculated from Eq. 4.6

$$LMTD = \frac{(T_{ai} - T_{oo}) - (T_{ao} - T_{oi})}{\ln(\frac{T_{ai} - T_{oo}}{T_{ao} - T_{oi}})} \quad \text{Eq. 4.6}$$

It is important to note that the fluid friction for annular space occurs at both the inner wall of the outer tube and the outer wall of the inner tube while the heat transfer takes place at the outer surface of the inner tube wall. Therefore, in calculating the overall heat transfer coefficient, the heat transfer area is either based on the inner or outer diameter of the inner tube at the discretion of the designer [108].

For the Reynolds and Prandtl numbers determination, equations 4.7 and 4.8 are used

$$Re = \frac{\rho V d_h}{\mu} \quad \text{Eq. 4.7}$$

$$Pr = \frac{C_p \mu}{K} \quad \text{Eq. 4.8}$$

Where

Re Reynolds number

Pr Prandtl number

V fluid velocity

K thermal conductivity

ρ density

d_h hydraulic diameter

The local heat transfer rate at both the inner and outer tube side is calculated with Eq. 4.9

$$h = \frac{Nuss\ K}{d} \quad \text{Eq. 4.9}$$

With the Nusselt number for laminar flow being [109]

$$Nuss = 3.66 + \frac{o.0668(\frac{d}{L} RePr)}{1+0.04[\frac{d}{L} RePr]^{0.67}} \quad \text{Eq. 4.10}$$

While for turbulent flow equation 4.11 is used

$$Nuss = 0.023\ Re^{0.8}\ Pr^{0.4} \quad \text{Eq. 4.11}$$

The total heat transfer area is given as

$$A_{total} = A_f + A_b \quad \text{Eq. 4.12}$$

Where A_f and A_b are the total fin surface area and un-finned bare tube area which are calculated with Eqs. 4.13 and 4.14 respectively [110]

$$A_f = 2N_f H_f L_f \quad \text{Eq.4.13}$$

$$A_b = \delta_f d_o L_f - N_f L_f \delta_f \quad \text{Eq. 4.14}$$

Where

N_f Numbere of fins

H_f fin height

L_f Fin length

δ_f Fin thickness

d_o Inner tube outer diameter

The effectiveness of the double pipe heat exchanger is determined using Eq. 4.15

$$\text{Ɛ}= \frac{heat\ transfered\ to\ oil}{maximum\ heat\ transferrable} \quad \text{Eq. 4.15}$$

This means that

$$\text{Ɛ} = \frac{Q_o}{q_{max}} \qquad \text{Eq. 4.16}$$

$$q_{max} = C_{min}(T_{ai} - T_{oi})$$

Where C_{min} is the minimum of the heat capacitance of either of the fluids as determined by Eq. 4.17.

$$C_{min} = \dot{m} * C_p \qquad \text{Eq. 4.17}$$

Eq. 4.1 to 4.17 were solved simultaneously using Engineering Equation Solver (EES) and Table 4.2 gives details of the model initial input values and results. The oil flow rate was chosen to reflect what is achievable on the test rig.

The following assumptions were made for successful modelling of DPHX

a) There is no heat loss in the DPHX during operation
b) Mass flow rates of both fluids were specified.
c) Inlet temperature of the fluids were specified
d) Outlet temperature of the thermal oil was specified

Table 4.2 Results from the mathematical model.

Parameter	**Initial Input Value**	**Output value**
Oil inlet temperature (K)	303	303
Oil outlet temperature (K)	473	473
Oil flow rate (kg/s)	0.020	0.020
Cathode exhaust inlet temperature (K)	873	873
Cathode exhaust outlet temperature (K)		687.3
Cathode exhaust mass flow rate, (kg/s)	0.038	0.038
Heat transfer rate, (kW)		7.82
Maximum heat transferable (kW)		24
Heat exchanger effectiveness Ɛ (%)		32.58
Overall heat transfer coefficient (W/m^2-K)		277.8

4.1.1 Influence of operating parameters on heat exchanger performance

This section gives detail of the effect of the change in operating conditions on the heat exchanger performance.

It was observed that at fixed inlet and outlet temperatures of the exhaust and thermal oil respectively, and fixed thermal oil flow rate, there was a minimum thermal oil inlet temperature at every exhaust flow rate. The exhaust inlet temperature was fixed at 823 K, while the thermal oil flow rate and outlet temperature were fixed at 0.02 kg/s and 473 K respectively. Figure 4.1 shows the minimum thermal oil inlet temperatures and their associated exhaust flow rate. It was discovered that below these minimum oil inlet temperature as specified in Figure 4.1, the equations could not be solved as there was no convergence. This was due to the fact that below this temperature, Eq. 4.6 resulted in a logarithm of a number less than or equal to zero. Hence, with the log mean temperature difference (LMTD) value, the minimum oil inlet temperature at each exhaust flow rate was determined.

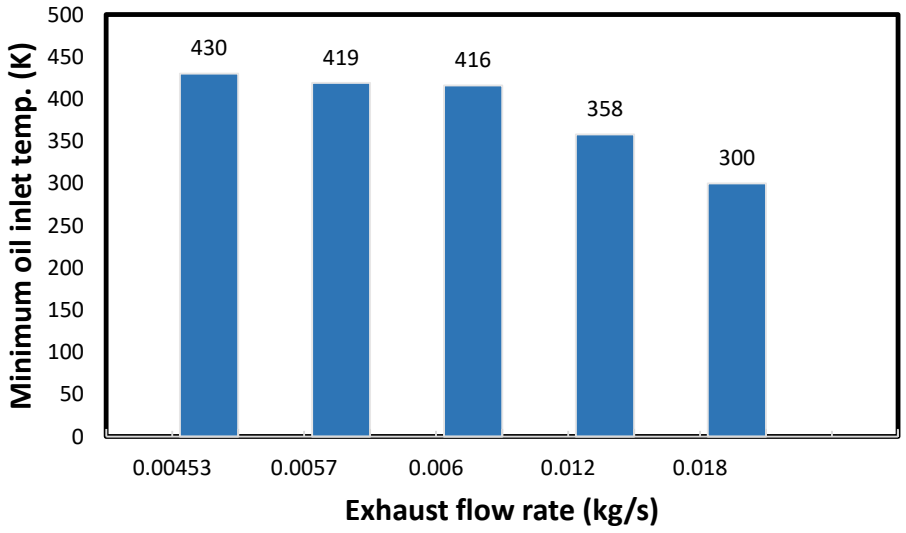

Figure 4.1 Effect of exhaust flow rate on thermal oil inlet temperature.

Effect of exhaust flow rate variation on heat exchanger performance

The effect of the exhaust flow rate variation on the exchanger performance was investigated here. The exhaust flow rate was varied between 0.00453 and 0.0.6 kg/s at fixed thermal oil flow rate of 0.02 kg/s and inlet temperature of 430 K, and exhaust inlet temperature of 873 K.

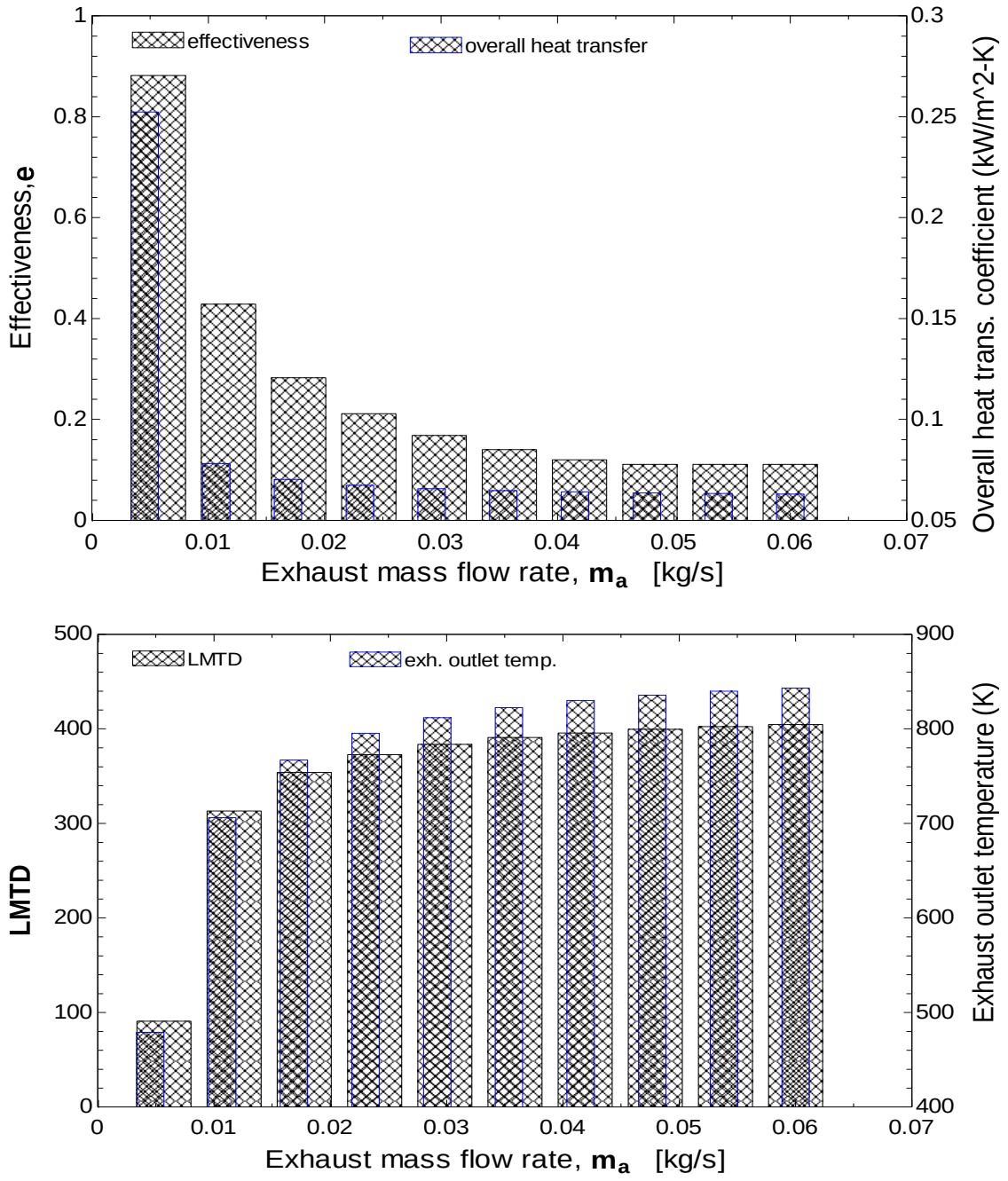

Figure 4.2 Effect of cathode exhaust flow rate variation on DPHX performance

It can be seen from Figure 4.2 that an increase in the exhaust flow rate increases the exhaust outlet temperature and logarithmic mean temperature difference (LMTD), while a reduction of the heat exchanger effectiveness was noticed. For balance of heat exchange between the hot cathode exhaust and thermal oil in the DPXH, the heat lost by the exhaust is equal to that gained by thermal oil. This means that the heat gained by the thermal oil is known since the inlet and outlet temperatures and flow rate are known and was 2.3 kW all through the variation of the exhaust flow rate. This heat gained by the thermal oil is equal to that lost by the hot exhaust, hence using Eq. 4.2, an increase in the exhaust flow rate increases the exhaust outlet temperature as the heat transfer and inlet temperature are known and fixed which basically explains the trend in Figure 4.2.

An increase in the exhaust outlet temperature will definitely increase the LMTD value which can be seen using Eq. 6. Increased LMTD negatively affects the overall heat transfer coefficient due to their irreversible proportional relationship as shown in equation 4.5. More so, the effectiveness is the ratio of the thermal oil heat gained to the product of the temperature difference between the exhaust and oil inlet temperatures and the product of the specific heat capacity and mass flow rate of the exhaust. Therefore, the exhaust flow rate is inversely proportional to the heat exchanger effectiveness, hence an increase in the exhaust flow rate negatively affects the heat exchanger effectiveness as seen in Figure 4.2.

Effect of oil flow rate variation

A similar investigation was carried out to find out the effect of varying thermal oil flow rate at different exhaust flow rates with their associated minimal thermal oil inlet temperature. Figure 4.3 and 4.4 shows the impact thermal oil flow rate had on the heat exchanger performance at the different exhaust flow rate.

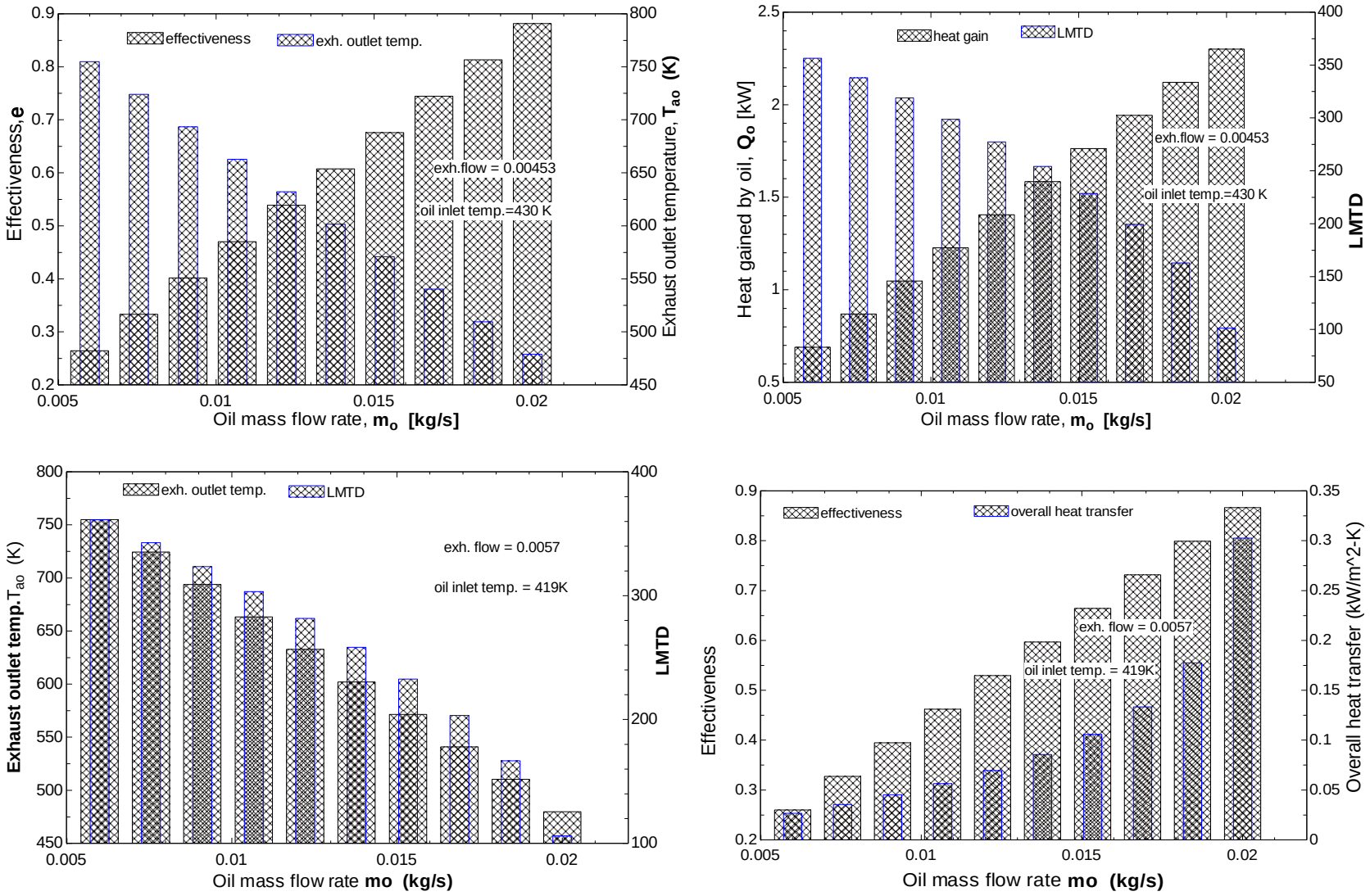

Figure 4.3 Effect of oil flow rate on heat exchanger performance

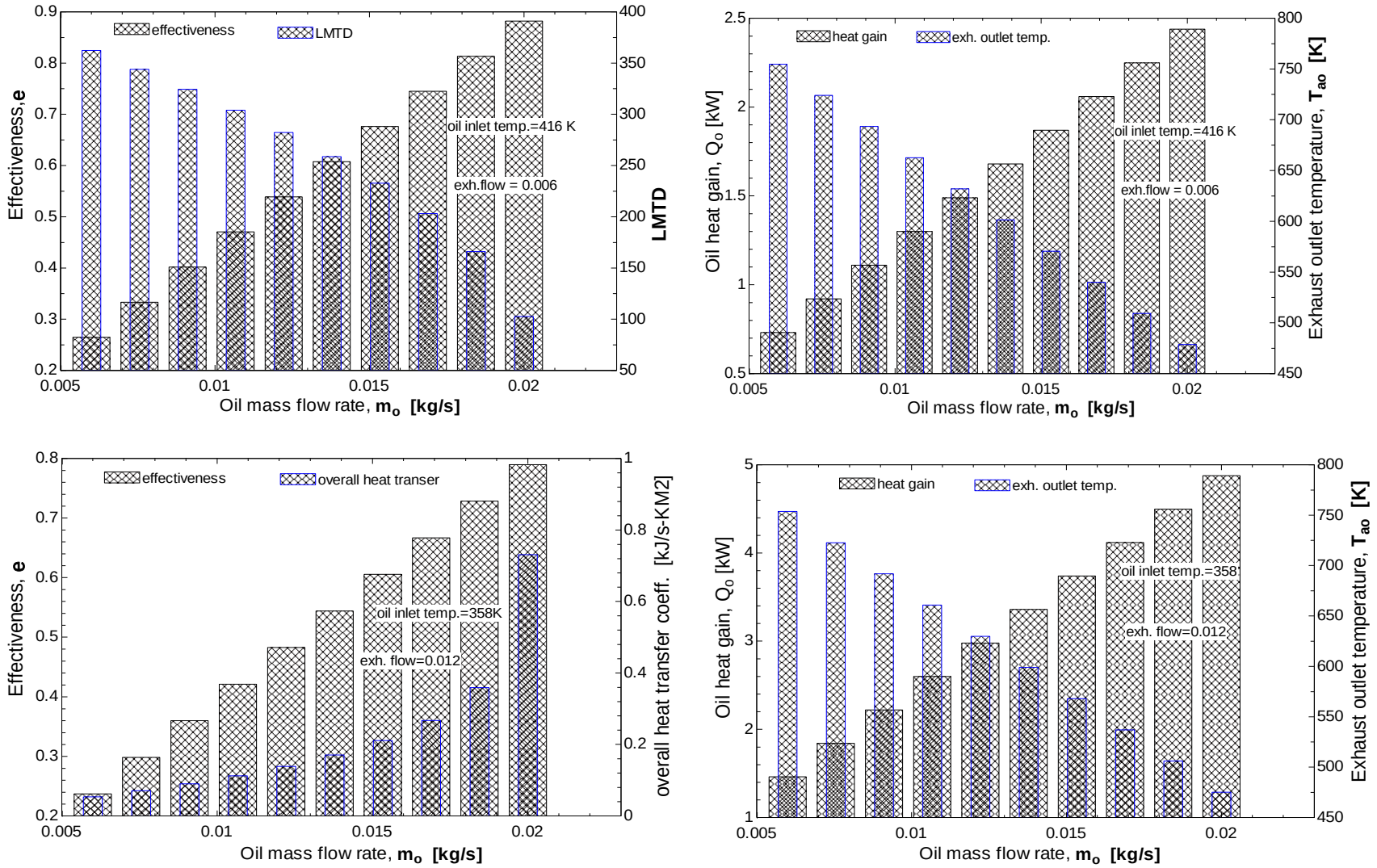

Figure 4.4 effect of oil flow rate on effectiveness, heat gained, and overall heat transfer

Figures 4.3 and 4.4 showed that an increase in the thermal oil flow rate at the different exhaust flow rate increases the thermal oil heat gained, heat exchanger effectiveness and overall heat transfer coefficient. This is due to the fact the heat gain is a product of the mass flow rate, specific heat capacity, and the temperature difference between the outlet and inlet, and since every other parameter is fixed any increase in the mass flow rate will definitely increase the heat gained by the thermal oil. More so, the effectiveness is a ratio of the thermal oil heat gain to the maximum heat transferable. Hence, an increase in the thermal oil heat gain will lead to an increase in the efficiency. Furthermore, the heat gained by the thermal oil is directly proportional to the overall heat transfer coefficient as seen in Eq. 4.5 which explains the increase in overall heat transfer in Figures 4.3 and figure 4.4 as the heat gained by the thermal oil increases. The exhaust heat is also a product of the mass flow arte, specific heat capacity and temperature difference between the outlet and the inlet as shown in Eq. 4.2. The exhaust flow rate and inlet temperatures are fixed, therefore, an increase in the heat will definitely reduce the exhaust outlet temperature which will further reduces the LMTD value as seen in Figures 4.3 and 4.4. The reduction in the exhaust outlet temperature also explains the increased heat gained in the exchanger in that the residence time of the cathode exhaust heat in the exchanger was higher thereby transferring more heat to the thermal oil.

From the ongoing parametric analysis, it has been shown that mass flow rate increase of thermal oil positively affects both the heat transfer rate and heat exchanger effectiveness, and the overall heat transfer coefficient. On the other hand, increasing the cathode exhaust flow rate negatively affects the effectiveness but increases the exhaust outlet temperature and the LMTD value. Table 4.3 shows a comparison of the heat exchanger performance at three different cathode exhaust flow rates and oil inlet temperatures. The inlet temperature of the thermal oil at exhaust flow rate of 0.00453 kg/s was 430 K, while it was 419 and 423 K respectively at

exhaust flow rates of 0.0057 and 0.039 kg/s. The oil outlet and exhaust inlet temperatures for the three exhaust flow rates were set at 473 and 873 K, respectively. The oil mass flow rate was kept constant at 0.02 kg/s

Table 4.3 Optimised operating conditions for the DPHX at different exhaust flow rates

Parameter	**Value at different Cathode exhaust flow rate**		
	0.00453 kg/s (3.698 L/s)	**0.0057 kg/s (4.653 L/s)**	**0.06 kg/s (48.98 L/s)**
Oil flow rate (kg/s)	0.02	0.02	0.02
Oil inlet temperature(K)	430	419	423
Oil outlet temperature (K)	473	473	473
Exhaust inlet temperature (K)	873	873	873
Exhaust outlet temperature (K)	478.9	479.7	838.4
Oil heat gained (Kw)	1.978	2.484	2.3
Effectiveness (%)	88.96	86.63	12.14
Overall heat transfer (W/m^2-K)	252.3	302.6	75.15

There was improvement in the heat exchanger effectiveness and overall heat transfer coefficient of 86.4% and 70.2% respectively at 0.00453 kg/s cathode exhaust flow rate as against those at 0.038kg/s, while it was 85.99% and 75.2% respectively at 0.0057 kg/s exhaust flow rate. It can also be seen in Table 3 that the overall heat transfer coefficient at 0.00453 kg/s exhaust flow rate was lower than that at 0.0057 kg/s though with a 2.6 % higher effectiveness. This is due to the reduced heat gained by the thermal oil from 2.3 kW to 1.978 kW. The heat exchanger is not used at its maximum capacity at exhaust flow rate of 0.038 kg/s, hence it would be ideal to use exhaust flow rate of 0.0057 kg/s due to the increased effectiveness, overall heat transfer, and even increased oil heat gained by 7.41 %.

4.2 Modelling of the rectifier/vapour separator

The rectifier is a hollow concentric cylinder with helical coil running through it. When the solution pump is turned on, the ammonia-water solution flows into the rectifier through the helical coil at one end and leaves at the other end of the coil. The hot pure ammonia vapour flowing in the shell upward (parallel flow) transfers the heat to the solution. By so doing, the solution leaves the rectifier at higher temperaturse and flows to the desorber thereby reducing the amount of heat needed at the desorber. This design is unique as it serves as the solution heat exchanger and vapour separator at the same time. It has high resistance to flow induced vibrations, accommodates thermal expansion and is compact due to the coiled nature of the inner tube. The NH_3-H_2O solution flowing in the coiled tube experiences secondary flow as depicted in Fig. 4.5. This flow has high ability to enhance heat transfer which depends on the tube and coil diameters [111].

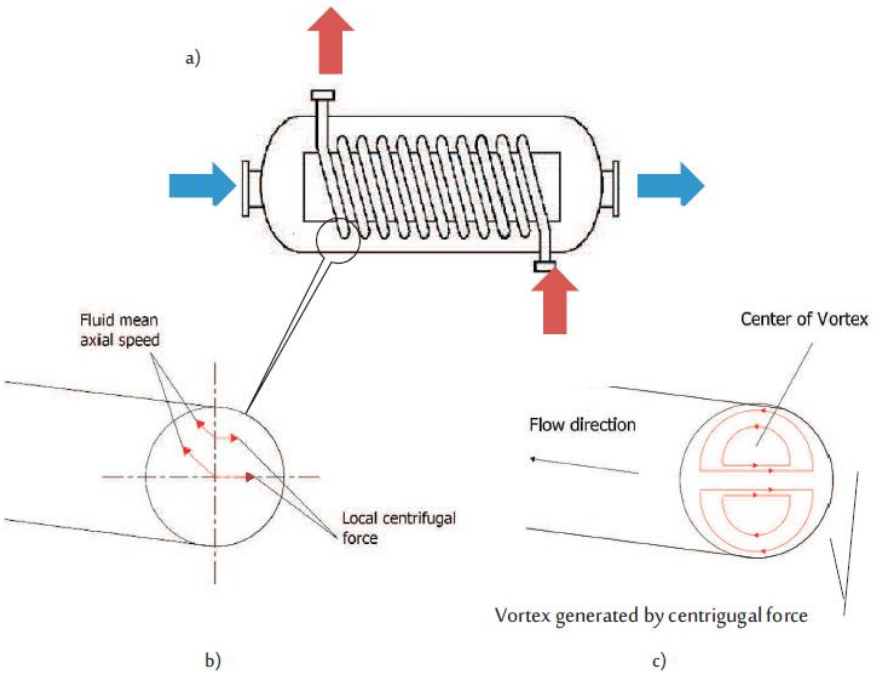

Figure 4.5 Schematic of rectifier with flows [112].

A centrifugal force is experienced by the fluid due to the shape of the coil in the heat exchanger (HX) depending on the local axial velocity as in Fig. 4.5b [112]. On the other hand, the fluid close to the tube wall experiences lower velocity compared to that in the coil due to the boundary layer, hence, the NH_3-H_2O solution in the coil is pushed outwards thereby recirculating counter-current vortices are formed as in Fig. 4.5c. The heat exchanger with assumptions is as shown in Fig. 4.6 and it is made of stainless steel.

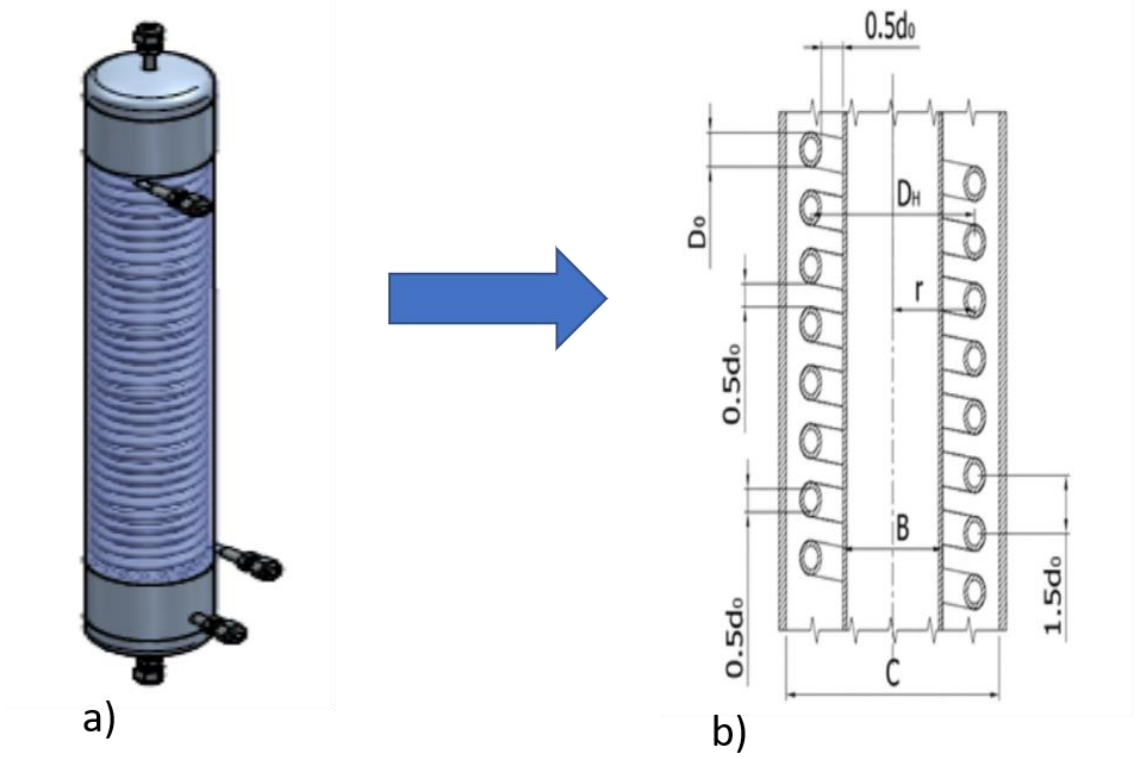

Figure 4.6 Schematic of rectifier heat exchanger with geometric assumptions.

For the purpose of this study, taking into account the working pair used, the rich or strong solution flows downward from top to bottom inside the helical coiled tube while hot pure ammonia flows upward in the shell side. It is assumed that when the ammonia-water vapour enters the rectifier from the desorber, the water vapour is separated and leaves from the bottom

of the rectifier while only pure ammonia vapour flows up the shell. Heat is transferred from the hot pure ammonia vapour to the strong solution in the coiled tube through the walls of the tube thereby increasing its temperature as it exits the rectifier and flows into the desorber. Since the strong solution enters the desorber at higher temperature, it will need less heat input from the thermal oil flowing at the other side of the desorber to evaporate the ammonia from the solution. The rectifier in this regard acts both as a solution heat exchanger and vapour separator.

Table 4.4 shows the rectifier design parameters while Table 4.5 gives a summary of the equations used for the modelling of the rectifier

Table 4.4 Rectifier design parameters.

Parameter	Value
Outside tube diameter Do (mm)	6
Average helix diameter DH (mm)	58
Height of cylinder H (mm)	400
Inner tube diameter Di (mm)	4
Outside diameter of inside cylinder B(mm)	42.4
Inside diameter of outer cylinder C (mm)	70.3

The following assumptions were made for the modelling of the rectifier.

1) ammonia-water solution enters the rectifier from the desorber.

2) only ammonia vapour flows upward into the condenser.

3) weak ammonia solution (low in ammonia concentration) leaves the rectifier and back flows into the absorber.

Table 4.5 Equations used for the modelling of the rectifier [111]–[113].

Parameter	Formula
Length of coil in cylinder	$L = N\sqrt{(2\pi r)^2 + P^2}$
Volume occupied by coil in cylinder	$V_c = \frac{\pi D_o^2 L}{4}$
Volume of shell side	$V_a = \frac{\pi}{4}(C^2 + B^2)PN$
Volume for fluid flow in shell side	$V_f = V_a - V_c$
Equivalent diameter of coiled tube	$D_e = \frac{4V_f}{\pi D_o L}$
Nusselt number at Reynolds $50 \leq 10{,}000$	$Nuss = 0.6Re^{0.5}Pr^{0.31}$
Nusselt number at Reynolds >10000	$Nuss = 0.36Re^{0.55}Pr^{0.333}\left(\frac{\mu}{\mu_p}\right)^{0.14}$
Reynolds number at shell side	$Re = \frac{GD_e}{\mu}$
Mass velocity	$G = 4M/\pi(C^2 - B^2) - (D_{H2}^2 - D_{H1}^2)$
Prandtl number	$Pr = \frac{C_P \mu}{K}$
Heat transfer coefficient at shell side	$h_o = 0.6Re_a^{0.5}Pr_a^{0.31}\frac{K_a}{D_e}$
Heat transfer coefficient at coil side	$h_{io} = h_{ic}\frac{D_i}{D_o}$
Corrected heat transfer coefficient based on inside coil diameter	$h_{ic} = h_i\left[1 + 3.5\frac{D_i}{D_H}\right]$
Heat transfer coefficient based on coil inside diameter	$h_i = j_{H1}Pr_s^{0.333}\frac{K_s}{D_i}$
Overall heat transfer coefficient	$\frac{1}{U} = \frac{1}{ho} + \frac{1}{hio} + \frac{x}{kc} + R_t + R_a$
Heat transfer rate	$Q = AULMTD$
Heat transfer area	$A = \pi D_o L$
Height of cylinder	$H = NP + D_o$

Where

P pitch (spacing between consecutive coil turns.)

N number of coil turns

C inside diameter of outer cylinder

B outside diameter of inner cylinder

μ dynamic viscosity of fluid

μ_p dynamic viscosity of wall

D_{H1} inside diameter of helix for by coil

D_{H2} outside diameter of helix formed by coil

M mass flow rate

D_i inside diameter of coil

D_o outside diameter of coil

j_{Hi} Colburn factor

R_t tube side fouling factor

R_a shell side fouling factor

In the rectifier, the heating fluid being ammonia vapour circulates over the wall of the coiled tube that is fitted in the shell and its flow rate is low compared to the heated fluid.The above equations were solved simultaneously using Engineering Equation Solver (EES) and Table 4.5 gives the results from the mathematical modelling.

Table 4.6 Rectifier model results.

Parameter	Value
Shell side h_o	55.93 W/m^2-K
coil side h_{io}	465.8 W/m^2-K
Overall heat transfer coefficient U_o	49.76 W/m^2-K
HX effectiveness ε	58.33%

4.2.1 Effect of Operating Conditions

There is need to know how influential some operating parameters may be on the performance of the rectifier hence this section looks into different parameter variation.

Variations of ammonia vapour inlet and outlet temperature

It is pertinent to understand the effect of changing various parameters on the others in order to know the maximum possible operating band of the rectifier. In view of this, some parameters were varied while keeping others constant.

As the two fluids flow in opposite direction in the rectifier there is transfer of heat between the two fluids. As the cold ammonia-water solution is pumped into the coil in the rectifier it is heated by the pure ammonia which is flowing in the opposite direction in the shell side to the condenser.

As depicted in Figure 4.7a, increasing the inlet temperature of the ammonia vapour (hot fluid) going into the rectifier from the desorber increases the heat transfer rate. Increased heat transfer

means that the rectifier can transfer more heat from the shell side to the ammonia-water solution in the coil tube thereby increasing the effectiveness of the rectifier.

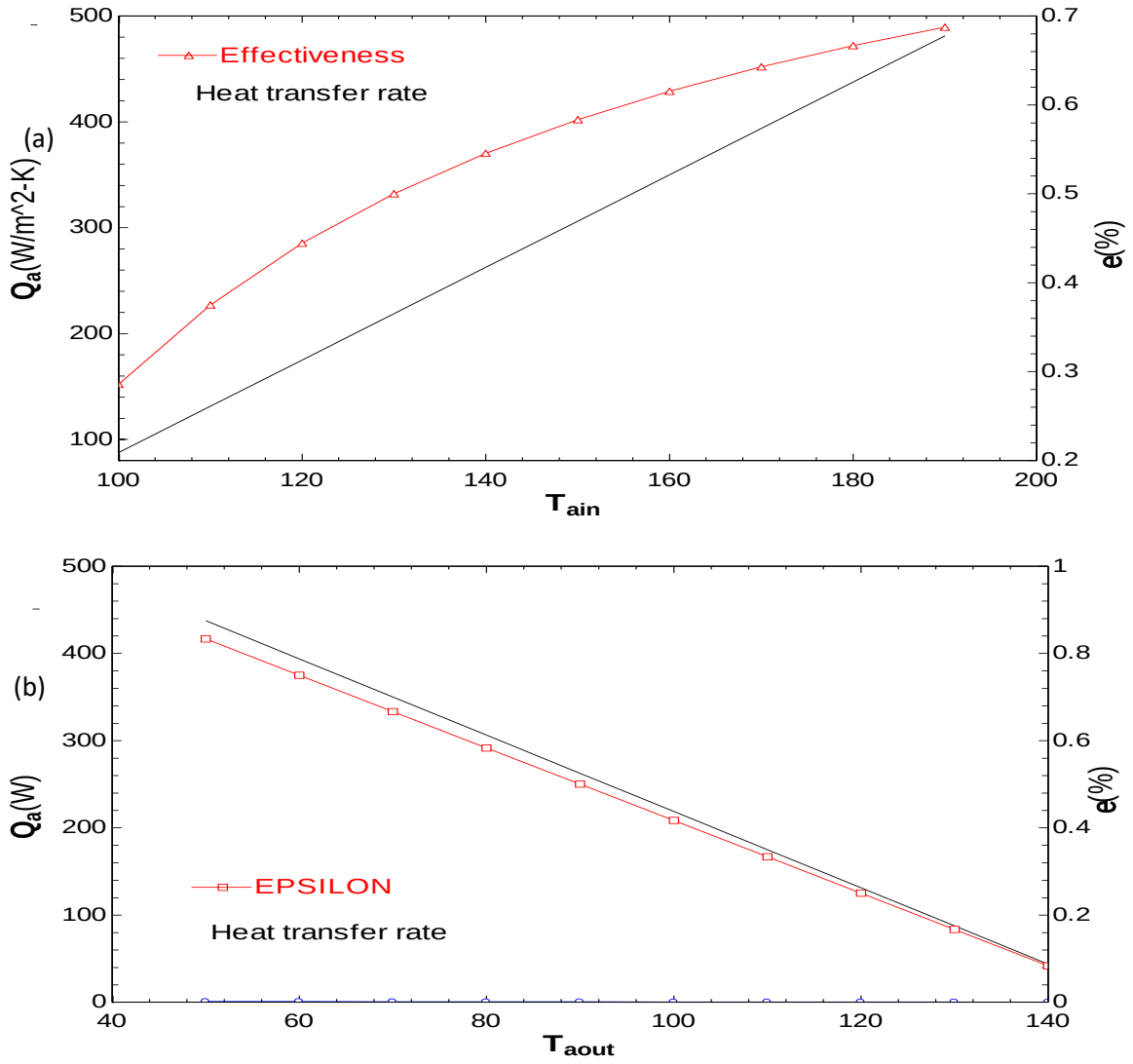

Figure 4.7 Ammonia inlet/outlet temperature effect on heat transfer and effectiveness.

This can be best verified in the relation for heat transfer rate and effectiveness as given in equations 4.1 and 4.16 respectively

As can be seen from equation 4.1, as the inlet temperature increases the heat transfer rate increases which increases the effectiveness as it is the ratio of the actual heat transfer to the maximum transferable heat.

On the other hand, increasing the outlet temperature reduces the heat transfer rate as it depends on the temperature difference between the inlet and the outlet. This subsequently reduces the effectiveness of the rectifier as there is less heat available to be absorbed. This is depicted in Figure 4.7b

Effect of mass flow rate on heat transfer

Figure 4.8 depicts the effect of either increasing or decreasing the mass flow on both sides on the local heat transfer and overall heat transfer coefficient. Increasing the mass flow of the shell side fluid (ammonia vapour) increases the local heat transfer on the shell side and consequently the overall heat transfer coefficient as shown in Fig. 4.8a. The same pattern is seen in the coil side when the mass flow rate of the ammonia-water solution is increased as in Fig. 4.8b

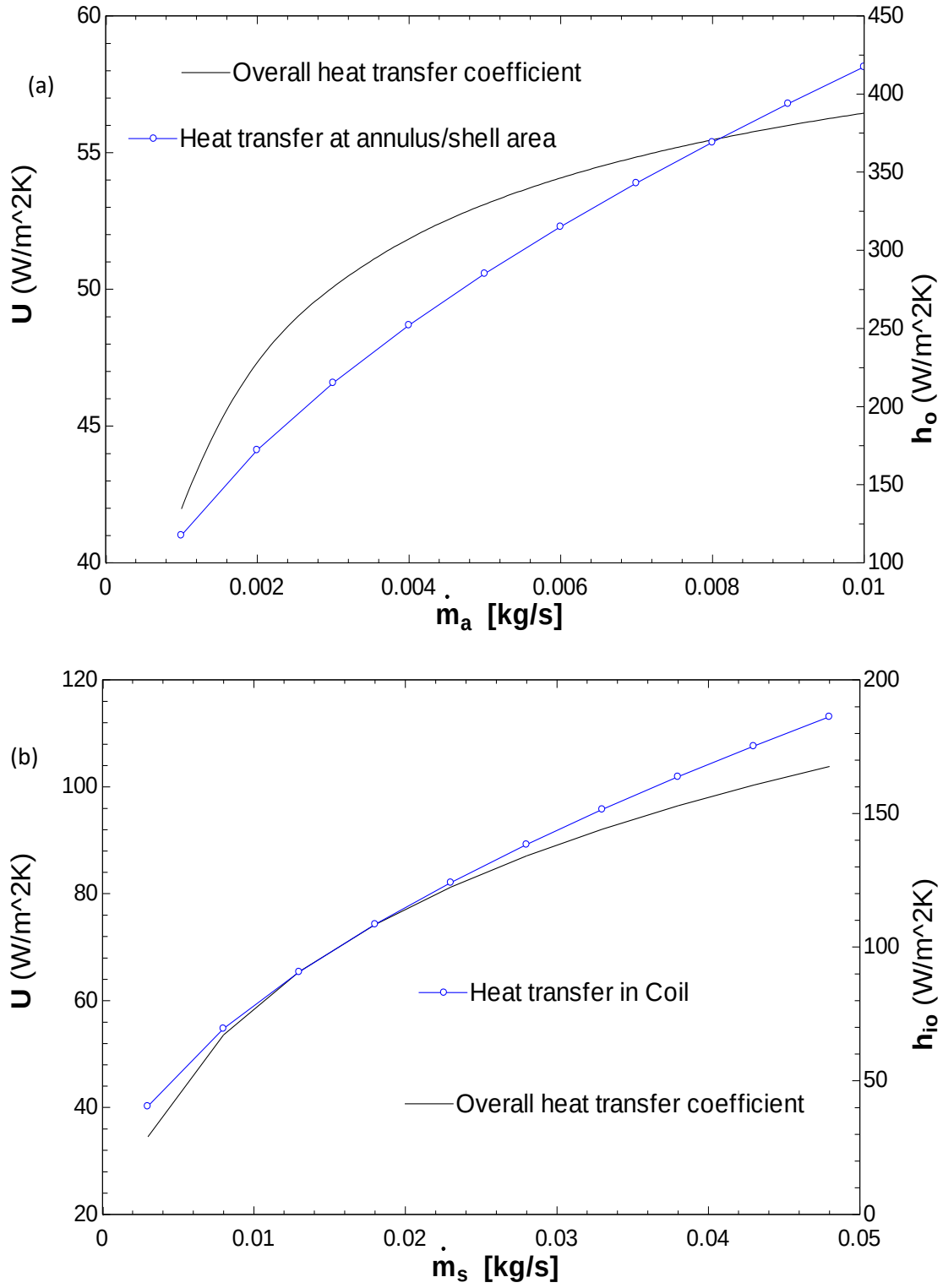

Figure 4.8 Variation of fluid flow rate with heat transfer.

4.2.2 Effect of design parameters

This section looks into the effect of varying the design parameters of the rectifier

Effect of helix diameter of the coiled tube on heat transfer

The helix diameter is the helical shape formed by the coiled tube in the shell. As can be seen in Figure 4.9, increasing the helix diameter reduces the coil side heat transfer but increases the overall heat transfer coefficient. This is because; as the helix diameter increases, the space between the coil and the inner cylinder becomes small. This area is inversely proportional to the overall heat transfer coefficient, hence the increase in the overall heat transfer coefficient.

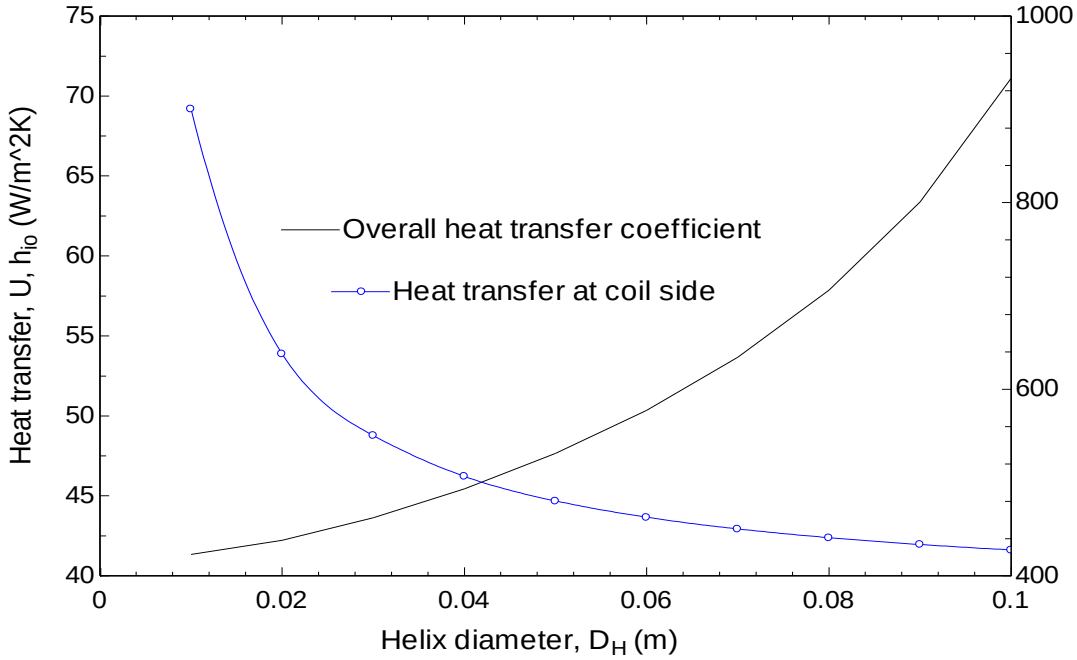

Figure 4.9 Variation of helix diameter with overall heat transfer coefficient.

Effect of coiled tube diameter variation

Varying either the inner (D_i) or outer diameter (D_o) of the coiled tube has effects on the heat transfer in the rectifier. As seen in figure 4.10a, an increase in the outer diameter causes an increase in the shell side heat transfer while that at the coil side reduces. On the other hand, the increase in the outer tube diameter enhances the overall heat transfer coefficient of the rectifier as shown in Figure 4.10b. More so, an increase in the coil inner diameter enhances both the coil side heat transfer and the overall heat transfer coefficient as depicted in figure 4.10c. This is because, as the outer tube diameter increases the space in the shell side is reduced thereby less time in getting contact with the coil wall, greater time to transfer heat to the fluid in the coiled tube due to the increase in the coil thickness resulting from the outer diameter increase.

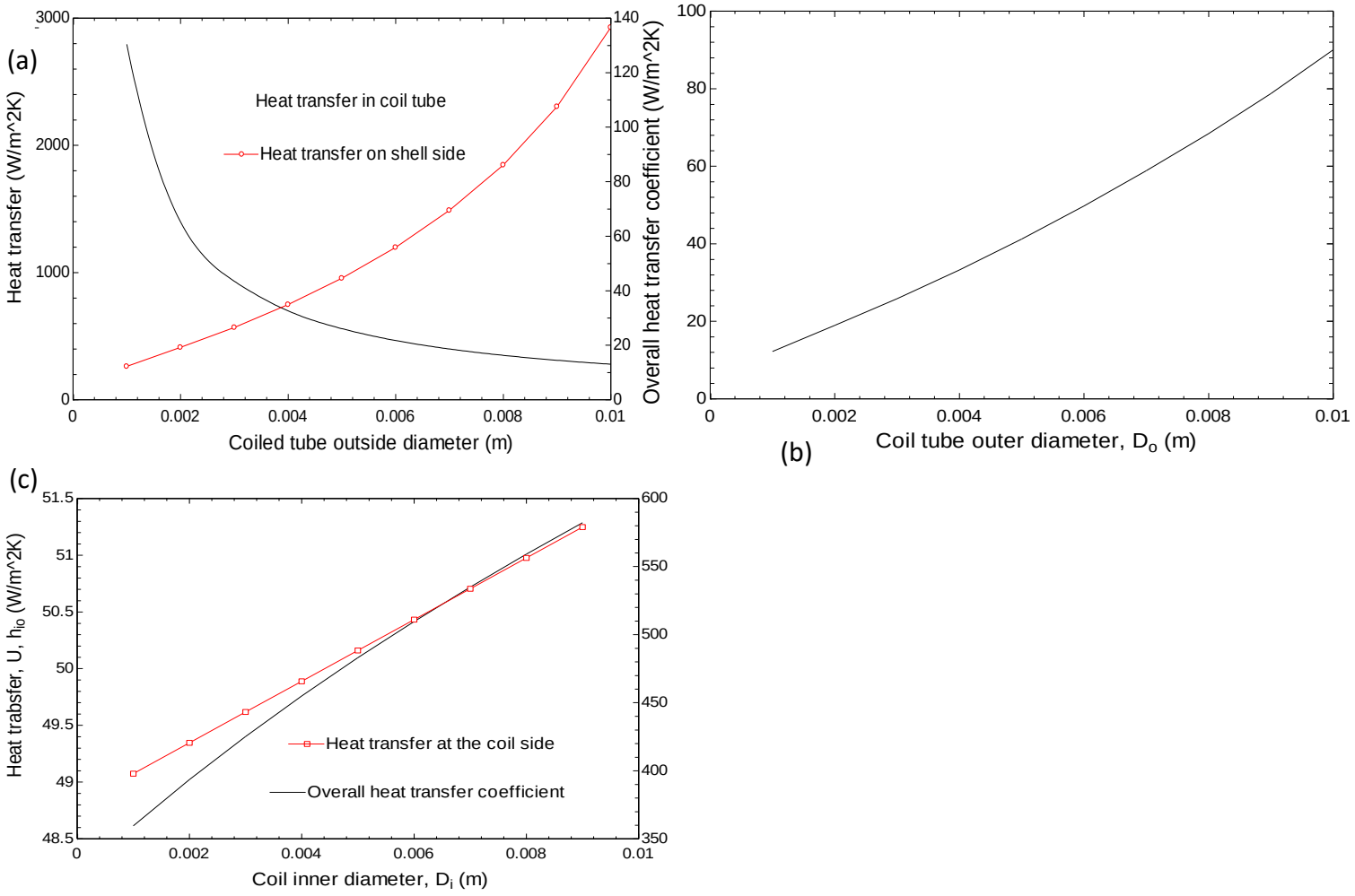

Figure 4.10 Variation of coil tube diameter on heat transfer

Effect of pitch variation

The pitch is the distance between two consecutive turns of the coil in the rectifier and varying it has an effect on several parameters. Figure 4.11a shows that increasing the pitch has an adverse effect on the local heat transfer and that of the overall heat transfer coefficient in that it results in the reduction of both coefficients.

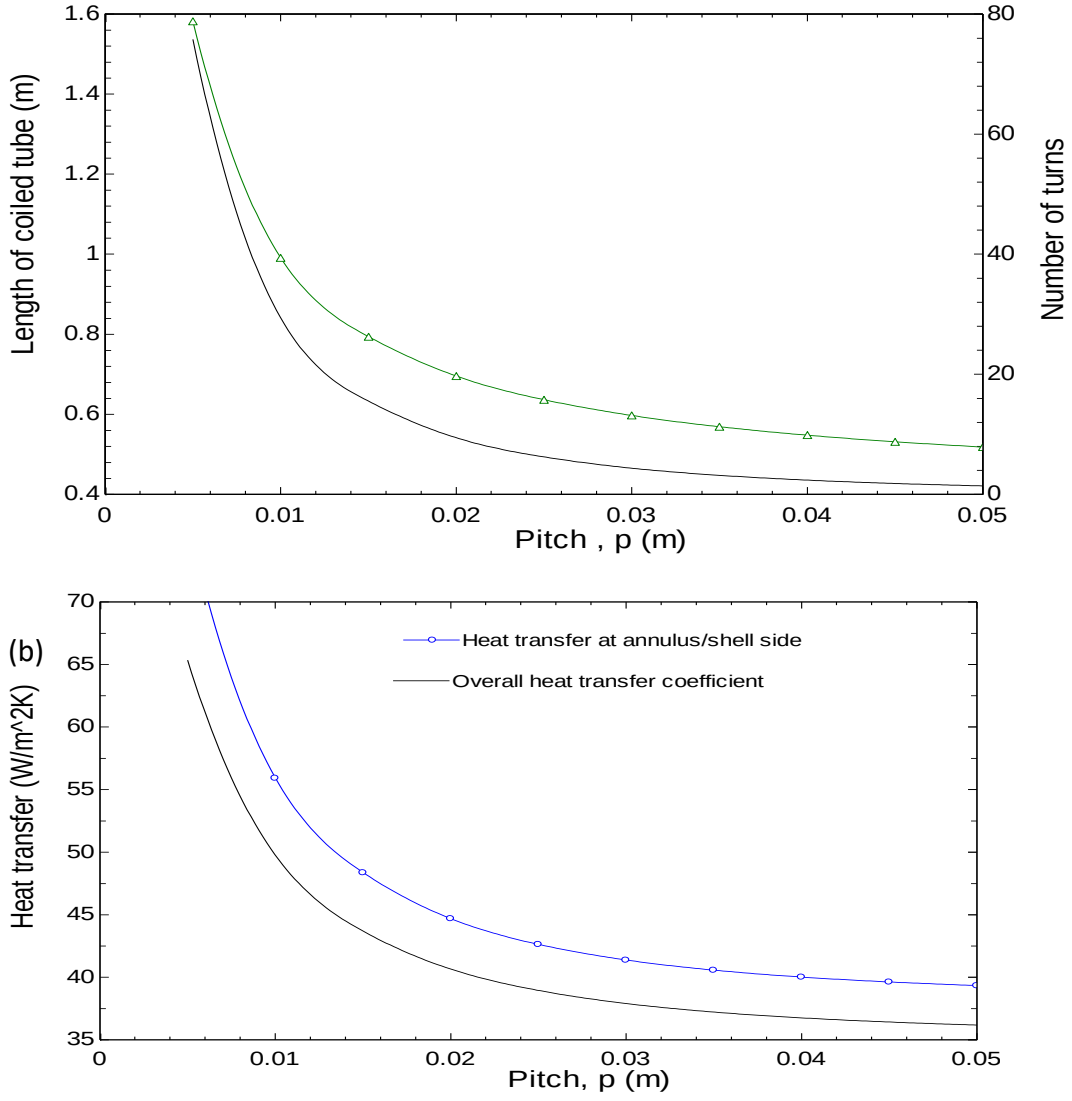

Figure 4.11 Pitch variation with local heat transfer, overall heat transfer coefficient, coil length and number of turns.

It is pertinent to note that pitch variation affects the number of turns and the length of the coiled tube. This is because any increase causes the number of turns and subsequently the length of the coiled tube to reduce as shown in Figure 4.11b while, keeping all other parameters constant. As depicted in Figure4.11b, the reduction in the coil number of turns and length becomes small as the pitch increases and will become insignificant above 50 mm in the case analysed.

Effect of outer cylinder on overall heat transfer

Figure 4.12 shows the effect of the variation of the outer cylinder diameter on the overall heat transfer, shell heat transfer and volume for NH_3 gas/vapour flow. It can be seen that as the diameter is increased the volume available for the fluid flow increases due to the increased annulus area. On the other hand, increasing the diameter reduces the heat transfer at the shell side and subsequently the overall heat transfer coefficient. This is because, the increased area gives longer time for the heat in the fluid to move towards the coil and transfer same thereby causing a reduction in the heat transfer and overall heat transfer, respectively.

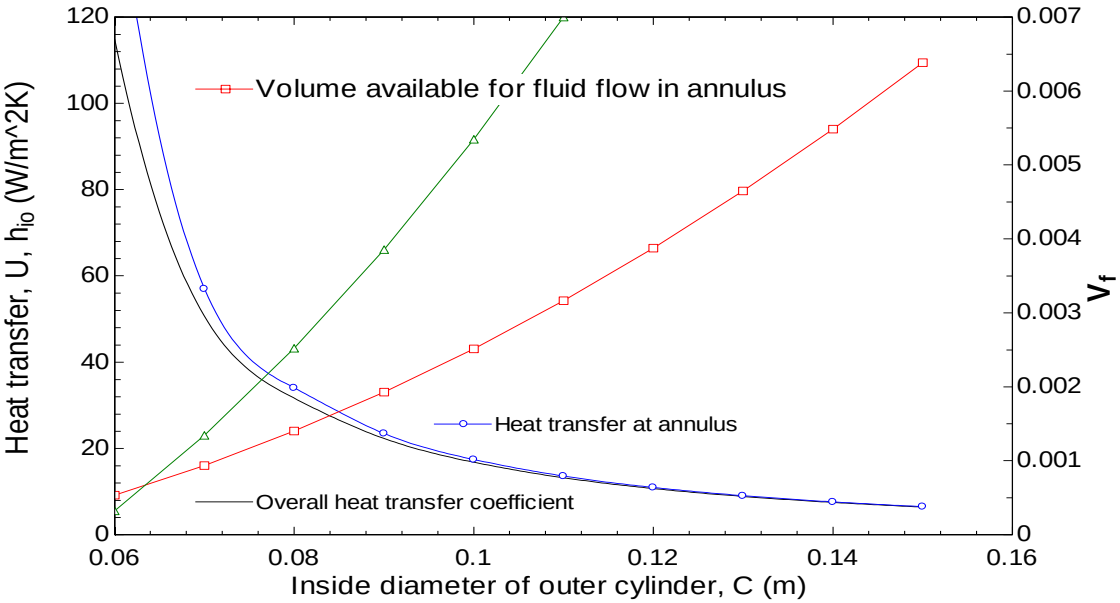

Figure 4.12 Effect of outer cylinder diameter on heat transfer.

4.3 Numerical Modelling of the absorber

Vapour absorption systems are made up of a generator, rectifier, condenser, evaporator and absorber as their main components depending on the working pair used in the system. The absorber is one of the most important components in the system because the system performance, sizing and cost depends on it, hence much attention is given to its research, development and manufacture [114]. The two types of absorbers mostly studied are the falling film and bubble type absorber, with ammonia-water as the working pair. During the absorption of ammonia into water in the absorber there is simultaneous heat and mass transfer that occurs from the beginning to the end which is complex, therefore studied thoroughly. The bubble type absorber has been proven to be better than the falling film type because of its better vapour distribution and high heat and mass transfer coefficients [115]. A model built to analyse the performance in terms of heat and mass transfer during the absorption process in absorbers in both falling film and bubble mode reveals the superiority of the bubble type. A plate heat exchanger with offset strip fin (OSF) in the coolant side was used for the analysis and parametric analysis carried out by Kang et al. [116]. Results showed that the heat exchanger size could be reduced to about 48.7% in the bubble mode compared to that in falling film mode because the rate at which ammonia was absorbed into water was always higher in the bubble mode.

Mathematical studies of bubble mode absorbers have been carried out by Fernandez-Serra [115] to investigate the simultaneous mass and heat transfer during the absorption process in a water cooled shell and tube absorber. The authors developed a differential mathematical model to analyse the process based on mass and energy balances and heat and mass transfer equations using finite-difference method. The model took into account the different flow patterns that

usually occur in bubble absorbers. Results showed that the absorption process occured faster in the lower regions than the upper part of the absorber. Ferreira et al. [117] conducted an experiment using a glass tube as the absorber which was water cooled and developed a mathematical model describing the absorption process in vertical tubular absorbers. In this study, the authors neglected the mass transfer that takes place during the absorption process and only studied the concentration and temperature behaviour along the tubes. They conducted two types of experiment, one without heat removal and the second with heat removal and compared the results with those from literature.

As stated earlier, the absorber contributes considerably to the cost, size and performance of the vapour absorption system. The cost and size will also depend on whether the absorber is water cooled or air cooled. Water cooled absorbers are more expensive as a cooling tower is required and the complexity of the system increases. In order to avoid these complexities, Fernández-Seara et al. [118] carried out a modelling study on a vertical tubular absorber that was air cooled with ammonia-water as the working pair . In their study, it was assumed that a bank of finned tubes are arranged vertically in a staggered form and a fan is used to force air over the tubes to effect heat removal from their surfaces as shown in Fig. 4.12c . Fig 4.13b shows the stages of the different types of flow in vertical tubular absorber with the slug flow region having bullet shaped bubbles normally referred to as Taylor bubbles.

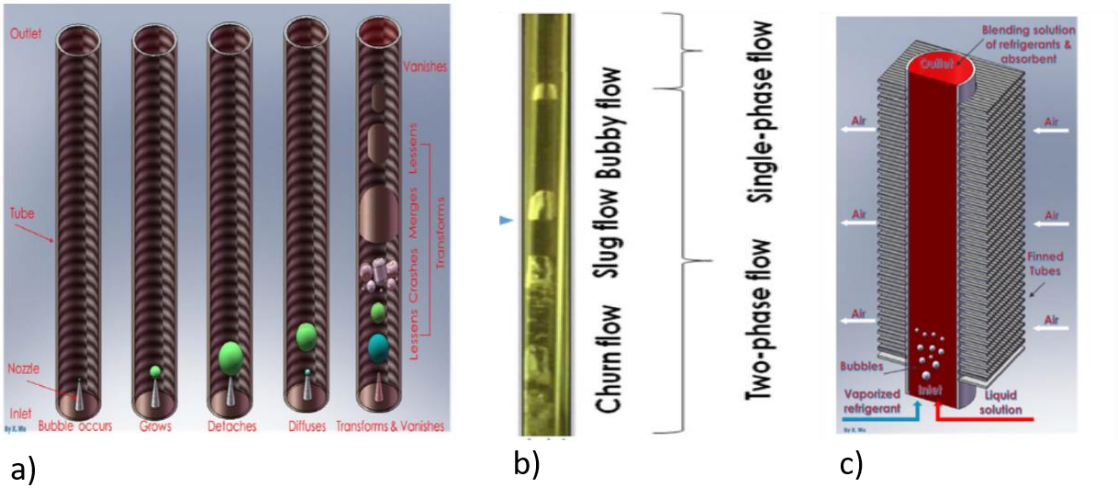

Figure 4.13 Bubble formation and disappearance during absorption with flow regions and phases [119].

The vapour is introduced at the bottom of the tube through a nozzle and leaves as a bubble while in contact with the liquid solution (churn flow), it later forms a bullet shape in the slug region as depicted in Figure 4.13a. It then progresses to the bubbly region where it is completely dissolved in the liquid. Fig. 13b shows that two phase flow exists only at the churn and slug regions while a single phase takes place in the bubbly region.

The vertical air cooled absorber is made up of a bundle of tubes in rows (four in this case) in staggered form in the direction of air flow as depicted in Fig.4.14, and externally finned with plate fins. The ammonia vapour and the weak solution (low ammonia content in water) are introduced into the absorber at the bottom and circulate co-currently upward during which the ammonia get absorbed into the weak solution and leaves with the strong solution at the top of the tubes.

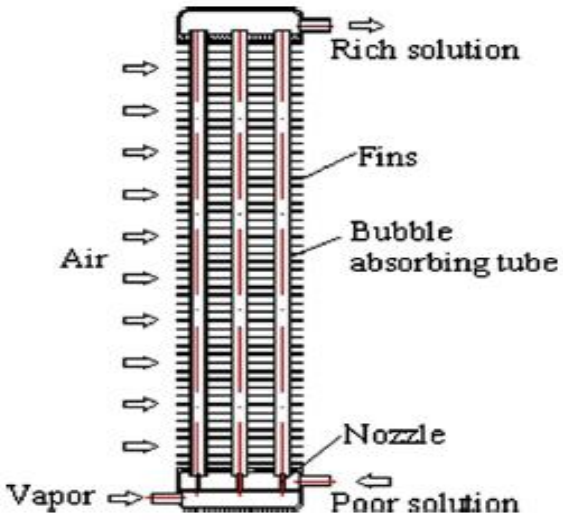

Figure 4.14 Schematic of air-cooled vertical tubular absorber [120].

As in Fig.4.14, the ammonia vapour enters at the bottom of the absorber and is introduced into the tubes via the nozzles while the weak ammonia-water solution enters through the space between the nozzles and the tubes. Both get in contact and mix, causing increased absorption from the bottom to the top. The process is complete when the ammonia vapour is fully absorbed in the liquid solution and the formed strong solution is removed from the top. The heat produced in the tubes during the absorption process is removed by the air provided by the fan which flows in cross section to the absorption process and in between the fins. Fig 4.15a and 4.15b show a schematic of the tube arrangement with geometrical parameters characterising the tubes and fins.

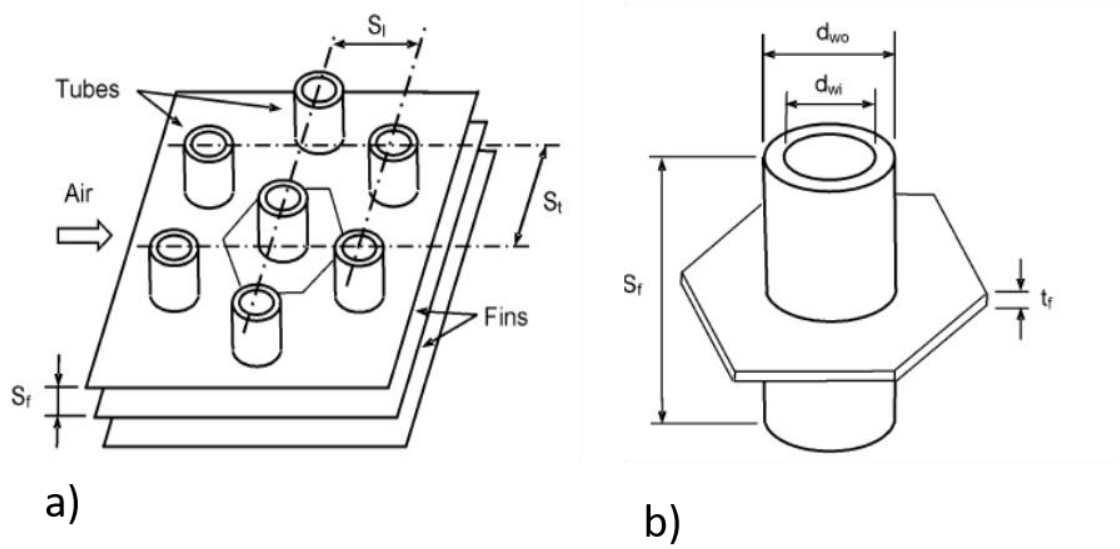

Figure 4.15 Geometrical parameters of tubes and fins with tube arrangement [118].

The absorber tubes are segmented into a number of incremental elements equal to the number of fins per tube with each discrete element comprising of corresponding portions of tube and fin as indicated in Fig. 4.15b, with table 4.6 showing the dimensions and descriptions of parameters.

A mathematical model has been developed on the basis of mass and energy balances and heat and mass transfer equations using a distributed mathematical modelling method and applied to each discrete element of fin and tube taking into account the churn, slug and bubbly flow patterns separately. The model takes into cognisance the simultaneous heat and mass transfer that take place in the liquid and vapour phases and the heat transfer to the cooling air through the finned tube.

Table 4.7 Geometrical and material properties of the absorber

Parameter	Value
Absorber length (m)	1.1
Inner tube diameter d_{wi} (m)	0.022
Outer tube diameter d_{wo} (m)	0.025
Fin spacing S_f (m)	0.006
Fin thickness t_f (m)	0.00045
Fin height H_f (m)	0.02
Number of rows	4
Number of tubes	60
Transversal tube spacing S_t (m)	0.05
Longitudinal tube spacing S_f (m)	0.0433
Nozzle diameter (m)	0.009
Tube wall thermal conductivity (W/mK)	13
Fin thermal conductivity (W/mK)	204

The following assumptions were made in building the mathematical model [114], [115], [118], [121]

i. There is constant absorber pressure and the absorption process is in steady state.

ii. The interface is at equilibrium hence no chemical reaction takes place at the interface.

iii. Liquid and gas are at equilibrium at the interface.

iv. Coolant, liquid and vapour properties are assumed constant at each discrete element.

v. No direct heat transfer between cooling air and vapour

vi. Heat transfer between tubes and fins is neglected.

vii. No bubble break up and coalescence.

viii. Air velocity around absorber is in a homogenous distribution.

The initial condition of the vapour and liquid were known and each tube was divided into a number of elements and incremental length equal to the fin spacing as shown in Figure 14b. A tube was selected to represent each row and the incremental elements solved from bottom to the top until the absorption process is complete. In each element, the outlet conditions were solved based on the initial inlet conditions. The outlet conditions of each solved element served as the inlet condition for the next consecutive element in the representative tube row, and this process continued until the absorption process was complete.

The cooling air outlet conditions of the first element serve as the inlet for the second row and the same procedure used in solving the elements of the first row was applied to solve those in the second row. This pattern was carried out on the third and fourth rows to complete the entire process. In each element, the mass and heat transfer equations, mass, concentration and energy balances were solved simultaneously to get the outlet conditions for the churn, slug and bubbly flow.

4.3.1 Development/formulation of mathematical equations

This section describes the method and procedures used in developing the mathematical equations for the absorber calculation. Fig. 4.16 shows the different types of flow patterns in the tube with churn flow existing just at the entrance, slug flow rising as bubbles with bullet

shape and later turning into small spherical bubbles in the bubbly region and eventually vanishing into the liquid.

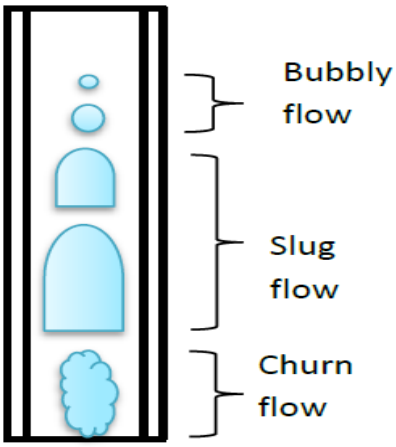

Figure 4.16 Flow profiles in vertical tubular absorber

The slug flow pattern is separately shown in Fig.4.17 with y_b, y_L, U_v, r_i, V_{Lf} and being the Taylor bubble length, distance between two Taylor bubbles, bubble rising velocity, interfacial radius, mean liquid film velocity and film thickness, respectively.

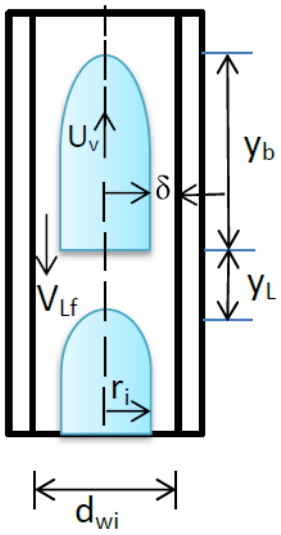

Figure 4.17 Schematic of slug flow region.

The concentration gradient in the vapour and liquid phases causes molecular diffusion, which in combination with the bulk transport of material through the interface results in mass transfer between the vapour and liquid phases [115]. Table 4.7 gives the basic formulated equations used for the mathematical model.

Where

Re_f, *film Reynolds number*

Sc, *Schmidt number*

Pr *Prandtl number*

D *mass diffusivity*

$\bar{M}$ *molecular weight*

Ti *interface temperature*

T_{vb} *bulk vapour temperature*

T_{Lb} *bulk liquid temperature*

d_{wi} *tube inner diameter*

d_{wo} *tube outer diameter*

η_f *fin efficiency*

Table 4.8 Mathematical equations for absorber modelling [109], [118], [121]–[125]

Parameter	Formula
Ratio of ammonia molar flux to total molar flux	$z = \frac{\dot{n}_{NH3}}{\dot{n}}$
Ammonia molar flux from bulk vapour to interface	$\dot{n}_{NH3v} = F_v z ln\left[\frac{z-\bar{x}_{vi}}{z-\bar{x}_{vb}}\right]$
Ammonia molar flux from interface to liquid	$\dot{n}_{NH3L} = F_{Li} z ln\left[\frac{z-\bar{x}_{Lb}}{z-\bar{x}_{Li}}\right]$
Mass transfer coefficient in liquid phase	$F_{Li} = 0.01099 Re_f^{0.3955} Sc_L^{0.5} \frac{D_L \bar{M}_L}{\rho_L}\left[\frac{g\rho_L^2}{\mu_L^2}\right]^{1/3}$
Mass transfer coefficient in vapour phase	$F_v = \frac{\alpha_v}{c_{pv}\bar{M}_v\left[\frac{Sc_v}{Pr_v}\right]^{2/3}}$
Mass flux of ammonia	$\dot{m}_{NH3} = \dot{n}_{NH3}\bar{M}_{NH3}$
Mass flux of water	$\dot{m}_{H2O} = \dot{n}_{NH3}\bar{M}_{NH3} + \dot{n}(1-z)\bar{M}_{H2O}$
Heat transfer from bulk vapour to interface	$\varphi_v = \alpha_v\left[\frac{c_v}{1-exp^{-c_v}}\right](T_{vb} - T_i)$
Heat transfer from interface to bulk liquid	$\varphi_L = \alpha_{Li}\left[\frac{c_L}{1-exp^{-c_L}}\right](T_i - T_{Lb})$
Heat transfer coefficient at vapour phase	$\alpha_v = 7.415\frac{K_v}{d_{wi}}$
Heat transfer coefficient at liquid phase	$\alpha_{Li} = F_{Li} c_{pL} \bar{M}_L\left[\frac{Sc_L}{Pr_L}\right]^{2/3}$
Heat transfer correction factor	$c = \frac{\dot{m}_{NH3}C_{pNH3} + \dot{m}_{H2O}C_{pH2O}}{\alpha}$
Overall heat transfer coefficient	$\frac{1}{U_o} = \frac{\Delta A_c}{\alpha_{Lw}\Delta A_L} + \frac{\Delta A_c}{2\pi k_w S_f} ln\frac{d_{wo}}{d_{wi}} + \frac{1}{\alpha_c \eta}$
Heat transfer coefficient between liquid phase and inner tube wall	$\alpha_{Lw} = \frac{1.88 k_L}{0.91 Re_f^{1/3}\left[\frac{\mu_L^2}{g\,\rho_L^2}\right]^{1/3}}$
Heat transfer coefficient between outer tube wall and cooling air	$\alpha_c = 0.134\, Re_a^{-0.319}\left[\frac{S_f}{H_f}\right]^{0.2}\left[\frac{S_f}{t_f}\right]^{0.11}$
Element inner tube area	$\Delta A_L = \pi d_{wi} S_f$
Element outer surface area	$\Delta A_c = \pi d_{wo}(S_f - t_f) + \Delta A_f$
Overall outer surface efficiency	$\eta = 1 - \frac{\Delta A_f}{\Delta A_c}(1-\eta_f)$
Element fin area	$\Delta A_f = 2\left[S_t S_l - \frac{\pi d_{wo}^2}{4}\right]$

The fin efficiency is calculated with Eq. 4.21

$$\eta_f = \frac{tanh\sqrt{\frac{2\alpha_c}{k_f t_f}}R\phi}{\sqrt{\frac{2\alpha_c}{k_f t_f}}R\phi} \quad \text{Eq.4.21}$$

Where k_f, t_f, and R, are fin thermal conductivity, fin thickness, and tube outer radius.

Mass, concentration and energy balances over the control volume in figure 15 are calculated from Eqs. 4.22, 4.23, and 4.24 for the vapour phase while those for the bulk liquid phase are determined from Eqs. 4.25, 4.26, and 4.27:

$$\Delta\dot{M}_v = -\dot{m}_{total}\Delta A_i \quad \text{Eq. 4.22}$$

$$\Delta\dot{M}_v x_v = -\dot{m}_{NH3}\Delta A_i \quad \text{Eq. 4.23}$$

$$\Delta\dot{M}_v h_v = -(\dot{m}_{NH3}h_{vNH3} + \dot{m}_{H2O}h_{vH2O} + \varphi_v)\Delta A_i \quad \text{Eq. 4.24}$$

$$\Delta\dot{M}_v = -\Delta\dot{M}_L \quad \text{Eq. 4.25}$$

$$\Delta\dot{M}_v x_L = -\Delta\dot{M}_L x_L \quad \text{Eq. 4.26}$$

$$\Delta\dot{M}_L h_L = -\Delta\dot{M}_v h_v - \varphi_c\Delta A_c \quad \text{Eq. 4.27}$$

Where ΔA_i is the heat and mass transfer area between the liquid and vapour phases and is determined from Eq. 4.28

$$\Delta A_i = a_{esp}S_f\frac{\pi - d_{wi}^2}{4} \quad \text{Eq. 4.28}$$

and a_{esp} is the specific interfacial area which must be determined for the three flow regions

In the churn flow, it is assumed that the flow is laminar at the entrance and it is investigated as an annular flow model as described in [126]. The interfacial radius r_i, and mean velocity V_{Lf}

are calculated iteratively from Eq. 4.29, 4.30, 4.31, and 4.32 where V_{Li} is the interfacial liquid velocity and $\Delta P/\Delta Z$ is the static pressure drop

$$\dot{M}_{Lf} = \pi\rho_L \left[\left(\frac{\Delta P}{\Delta Z} + \rho_v g \right) \left(\frac{r_w^2 - r_i^2}{8\mu_L} \right) + \left(\frac{\rho_L - \rho_v}{8\mu_L} \right) \left[(r_w^2 - r_i^2)^2 + 2r_i^2 \left(r_i^2 - r_w^2 + 2r_i^2 ln \frac{r_w}{r_i} \right) \right] \right]$$

$$\frac{\Delta P}{\Delta Z} = \left[\frac{1}{\frac{r_i^4}{16\mu_v} + \frac{r_i^2 (r_w^2 - r_i^2)}{8\mu_L}} \right] \left[\left(\frac{\dot{M}_v}{2\pi\rho_v} - \frac{(\rho_L - \rho_v) g r_{ri}^2}{8\mu_L} \right) \left(r_w^2 - r_i^2 + 2r_i^2 ln \frac{r_i}{r_w} \right) \right] - \rho_v g \qquad \text{Eq.4.30}$$

$$V_{Li} = \left(\frac{r_w^2 - r_i^2}{4\mu_L} \right) \left(\frac{\Delta P}{\Delta Z} + \rho_v g \right) + \left(\frac{g(\rho_L - \rho_v)}{4\mu_L} \right) \left(r_w^2 - r_i^2 + 2r_i^2 ln \frac{r\ \ i}{r_w} \right) \qquad \text{Eq. 4.31}$$

$$V_{Lf} = \frac{V_{Li}}{2} + \left(\frac{(\rho_L - \rho_v) g r_i^2}{8\mu_L} \right) \left[2 - \frac{r_w^2 + r_i^2}{r_w^2 - r_i^2} \right] ln \left(\frac{r_i}{r_w} \right)^2 \qquad \text{Eq. 4.32}$$

The specific interfacial area in the churn flow is determined with Eq. 4.33

$$a_{esp} = \frac{2r_i}{r_w^2} \qquad \text{Eq. 4.33}$$

In the slug flow region the vapour phase rises in the form of bullet shaped bubbles and is assumed to have a-half sphere nose and a cylindrical body as shown in Fig.4.17. The interfacial radius r_i and the mean velocity of the liquid film V_{Lf} in this region are calculated iteratively with Eqs. 4.34, 4.35, and 4.36 [115].

$$U_v r_i^2 - V_L r_w^2 = V_{Lf} (r_w^2 - r_i^2) \qquad \text{Eq.4.34.}$$

$$V_{Lf} = \left(\frac{(\rho_L - \rho_v) g r_w^2}{8\mu_L} \right) \left[1 - 3 \left(\frac{r_i}{r_w} \right)^2 - \left(\frac{4 \left(\frac{r_i}{r_w} \right)^4 ln \left(\frac{r_i}{r_w} \right)}{1 - \left(\frac{r_i}{r_w} \right)^2} \right) \right] + \left[\frac{\Delta P}{\Delta Z} + \rho_v g \right] \left[\frac{r_w^2 - r_i^2}{8\mu_L} \right] \qquad \text{Eq. 4.35}$$

$$\frac{\Delta P}{\Delta Z} = \left[\frac{1}{\frac{r_i^4}{16\mu_v} + \frac{r_i^2\left(r_w^2 - r_i^2\right)}{8\mu_L}}\right]\left[\left(U_v \frac{r_i^2}{2} + \frac{(\rho_L - \rho_v) g r_{ri}^2}{8\mu_L}\right)\left(r_w^2 - r_i^2 + 2r_i^2 ln\frac{r_i}{r_w}\right)\right] + \rho_v g \quad \text{Eq. 4.36}$$

Where U_v, the mean bubble rise velocity, and V_L, the total volume flux, are determined with Eq. 4.37 and 4.38, respectively.

$$U_v = 1.2\frac{\dot{V}_v + \dot{V}_L}{A_t} + 0.35\left[\frac{g d_{wi}(\rho_L - \rho_v)}{\rho_L}\right]^{1/2} \quad \text{Eq. 4.37}$$

$$V_L = \frac{\dot{V}_v + \dot{V}_L}{A_t} \quad \text{Eq. 4.38}$$

Where $\dot{V}_v$, $\dot{V}_L$, and A_t are the volumetric flow rate of the vapour, volumetric flow rate of the liquid and the tube cross sectional area respectively,

The length of the bubble y_b, and the separation distance between two Taylor bubbles are evaluated with Eqs. 4.39, and 4.40, respectively

$$y_b = \left[\frac{\dot{M}_v}{\rho_v \dot{N}_b} + \frac{\pi r_i^2}{3}\right]\left(\frac{1}{\pi r_i^2}\right) \quad \text{Eq. 4.39}$$

$$y_L = \left[\frac{U_v}{\dot{N}_b} - y_b\right] \quad \text{Eq. 4.40}$$

Where ρ_v, $\dot{M}_v$, and $\dot{N}_b$ are the vapour density, mass flow rate of the vapour and bubble frequency. The bubble frequency used here is that experimentally determined in [127] and is set to a value of $\dot{N}_b = 3$

The slug flow void fraction, terminal velocity and specific interfacial area are determined from Eqs. 4.41, 4.42 and 4.43, respectively

$$\varepsilon = \frac{U_{vs}}{C_o U_v + U_\infty} \quad \text{Eq. 4.41}$$

$$U_{\infty} = 0.35\left[\frac{g d_{wi}(\rho_L - \rho_v)}{\rho_L}\right]^{1/2} \quad \text{Eq. 4.42}$$

$$a_{esp} = \frac{2r_i y_b + 0.1 r_i^2}{r_i^2 (y_b - y_L)} \quad \text{Eq. 4.43}$$

Where C_o, U_{vs}, U_{Ls} are constant gas superficial velocity and liquid superficial velocity and are determined with Eqs. 4.44, 4.45, and 4.46

$$C_o = 1.2 - 0.2\left[\frac{\rho_v}{\rho_L}\right]^{1/2} \quad \text{Eq. 4.44}$$

$$U_{vs} = \frac{\left(1 - \frac{4\delta}{d_{wi}}\right)}{A_t} U_v \quad \text{Eq. 4.45}$$

$$U_{Ls} = \frac{\left(1 - \frac{4\delta}{d_{wi}}\right) U_v - \dot{V}_v - \dot{V}_L}{A_t} \quad \text{Eq. 4.46}$$

On the other hand, the specific interfacial area and the average bubble radius in the bubbly flow region are determined from Eqs. 4.47 and 4.48, respectively, with the bubble frequency in this case set to 1.5

$$a_{esp} = \frac{4 r_B^2}{r_w^2 Z_B} \quad \text{Eq.4.47}$$

$$r_B = \left[\frac{\dot{M}_v}{2\,\pi\,\rho_v}\right]^{1/3} \quad \text{Eq. 4.48}$$

Where Z_B is the bubble separation distance and given by Eq. 4.49

$$Z_B = \frac{V_B}{\dot{N}_b} \quad \text{Eq. 4.49}$$

Here, 1.5 is the bubble frequency, $\dot{N}_b$, and V_B is the single bubble rise velocity in bubbly flow determined with Eq. 4.50. This is based on the assumption that the bubble behaves as a solid sphere [128]:

$$V_B = V_\infty \left[1 + \frac{2.4 r_B}{r_v}\right]^{-1} \quad \text{Eq. 4.50}$$

Where V_∞ is the terminal rise velocity determined with Eq 4.51 by applying the Stokes solution assuming a single isolated smallest bubble [129].

$$V_\infty = \frac{2 r_B g(\rho_L - \rho_v)}{g \mu_L} \quad \text{Eq. 4.51}$$

All the above equations were implemented and solved iteratively in Engineering Equation Solver (EES). The procedure for solving these equations is summarised as follows [118]

(1) Guess the interface temperature T_i

(2) Considering equilibrium and saturation, calculate the ammonia molar concentration at the liquid and vapour interface X_{Li} and X_{vi}

(3) Guess z

(4) Calculate $\dot{n}_{NH3L}$ and $\dot{n}_{NH3v}$

(5) If $\dot{n}_{NH3L} = \dot{n}_{NH3v}$ go to step 6 otherwise guess another value of z and go to step 4

(6) Calculate ammonia and total mass flux

(7) Calculate sensible heat transferred from liquid and vapour phases

(8) Check energy balance at interface and if verified go to step 9 otherwise guess a new value of interface temperature T_i and go to step 2

(9) Guess T_{co}

(10) Calculate heat flux transferred from liquid to the air

(11) Check T_{co} with the following equation, if equal go to step 12 otherwise guess new values of T_{co} and go to step 9.

$$T_{co} = T_{ci} + \frac{\varphi_c \, \Delta A_c}{\dot{M}_c \, C_{pa}} \quad \text{Eq.4.52}$$

(12) The new vapour and liquid values is then calculated using the equations in Table 4.7

The initial input parameters for the absorber operating conditions are shown in table 4.8, while the geometry and material thermal properties of the absorber are found in Table 4.6. These parameters were used in solving the unknown conditions of the absorption process from bottom to top of each tube row.

Table 4.9 Absorber operating conditions

Parameter	**Value**
Vapour mass flow rate (kg/h)	15.0
Vapour concentration (kgNH3/kg)	0.995
Vapour temperature (K)	288.15
Inner tube pressure (bar)	2.25
Weak solution mass flow rate (kg/h)	135.0
Weak solution concentration (kgNH3/kg)	0.235
Weak solution temperature (K)	323.15
Cooling are facing velocity (m/s)	2.5
Cooling air flow rate (kg/s)	1.8
Cooling air inlet temperature (K)	303.15

4.3.2 Results and Discussion

With the initial input parameters as presented in Tables 4.6 and 4.8, the output values/results from the model were calculated with the help of the developed mathematical model. This section presents the results from the model and the sensitivity analysis carried out. The absorption process was considered to be complete when the vapour flow rate became less than

1% of its initial value of concentration at the beginning of the flow. Table 4.10 shows the results from the numerical modelling of the absorber after solving the mathematical equations given in the previous section.

Table 4.10 Modelling results varying temperature and length of absorber

Rows	1	2	3	4
Strong solution mass flow rate (kg/h)	36.7	36.7	36.7	36.7
Strong solution concentration (kg NH3/kg)	0.298	0.298	0.298	0.298
Strong solution temperature (K)	305.6	305.7	307.35	307.57
Absorption length (m)	0.90	0.95	1.0	1.03

Fig. 4.18 shows the pattern of the absorption process as it occurs from bottom of the tube to the top for each tube row. They are similar in progression pattern from churn to slug and slug to bubbly flow. The horizontal lines indicate the transition from one flow pattern to the other. This is more pronounced in the slug flow region. This means that the absorption process occurs more in the slug flow region than the other two regions as shown. This is because there is high mass and heat transfer that takes place in this region as the vapour is absorbed into the liquid solution. It could also be depicted that the length at which the absorption is completed is different for each tube row and it increases from the first to the last row. This is because as the air flows over the tubes it cools the tubes and in the process increases in temperature as it flows past the first row which results in slower absorption rate in successive rows according to the air flow direction. In view of the effect of the air flow rate on the absorption process, the absorber height should be based on the longest absorption length which is the fourth row in this case.

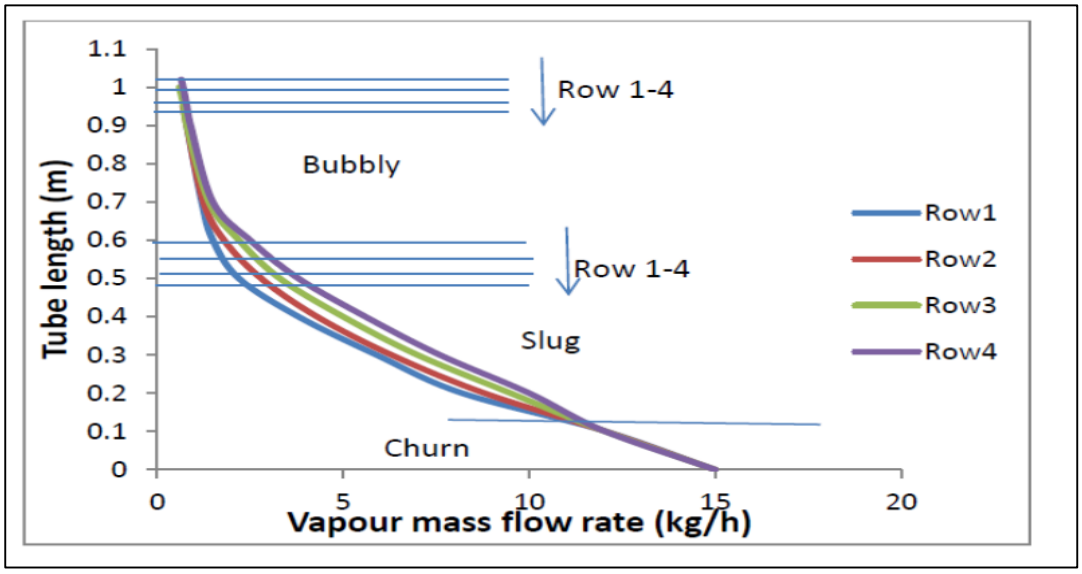

Figure 4.18 Absorption process along tube length

It can be deduced from this finding that the absorber height is greatly influenced by the slug flow region, which means that if the slug region is reduced, the absorber height will be reduced and vice versa. This can be achieved by adding Nano-particles to enhance the heat and mass transfer process which improves the thermal conductivity of the fluid, thereby increasing the rate at which absorption takes place leading to a shorter absorption length [130]–[138]. Other ways of performance enhancement are the addition of chemical surfactants, carbon nanotubes, and ultrasonic or magnetic fields [139]–[147].

It is also pertinent to study the behaviour of the liquid phase temperature along the length of the tube and cooling air temperature at the end of each tube row. During the absorption process inside the tube simultaneous heat and mass transfer take place and this affects the liquid phase and cooling air temperature. It can be deduced from Fig. 4.19 that both the liquid phase temperature and that of the cooling air reduces in the churn flow region and tends to increase again in the slug flow region before reducing further. The small increment noticed at the beginning of the slug flow is caused by the heat and mass transfer that is taking place in this

region leading to higher temperature. As the air flows across the bundle of the tubes it takes away heat from the tube surface, hence increases in temperature as it moves past the first through to the last row.

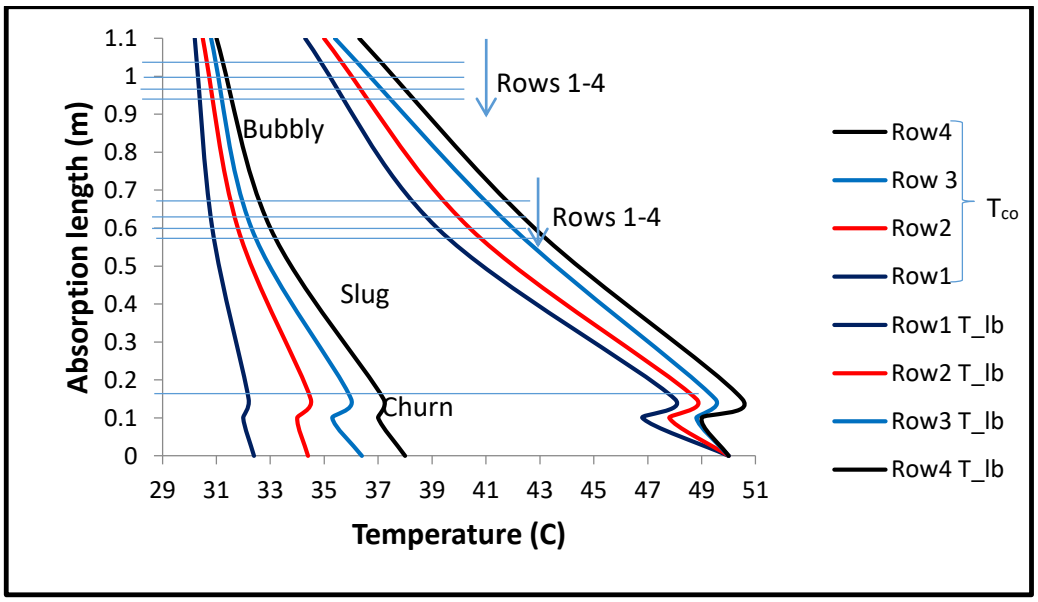

Figure 4.19 Liquid phase temperature, and air temperature along tube length in each row, and outlet of each row, respectively.

Sensitivity analysis was carried out to investigate the influence of varying any of the geometrical design parameters and operating conditions while keeping all other parameters constant. Figure 4.20a shows the effect of varying the fin spacing on the absorber performance. It could be seen that the fin spacing had a negative effect on absorption length implying that the fin spacing played an important role in sizing the absorber. Hence, the fin spacing must be the possible smallest taking into account the contact between the fins and the tubes, mechanical expansion and available manufacturing technology. On the other hand, Fig. 4.20b depicts the outer tube diameter influence on the absorber performance when varied. It shows that the tube length reduces with an increase in the outer tube diameter while there is high deterioration on

the absorption behaviour if the outer tube diameter becomes too low. The tube will require large amount of metal for manufacturing as the outer tube diameter increase which has an advert effect on the performance of the absorber. It could also be seen from both graphs that the tube rows have almost similar effect when these parameters are varied.

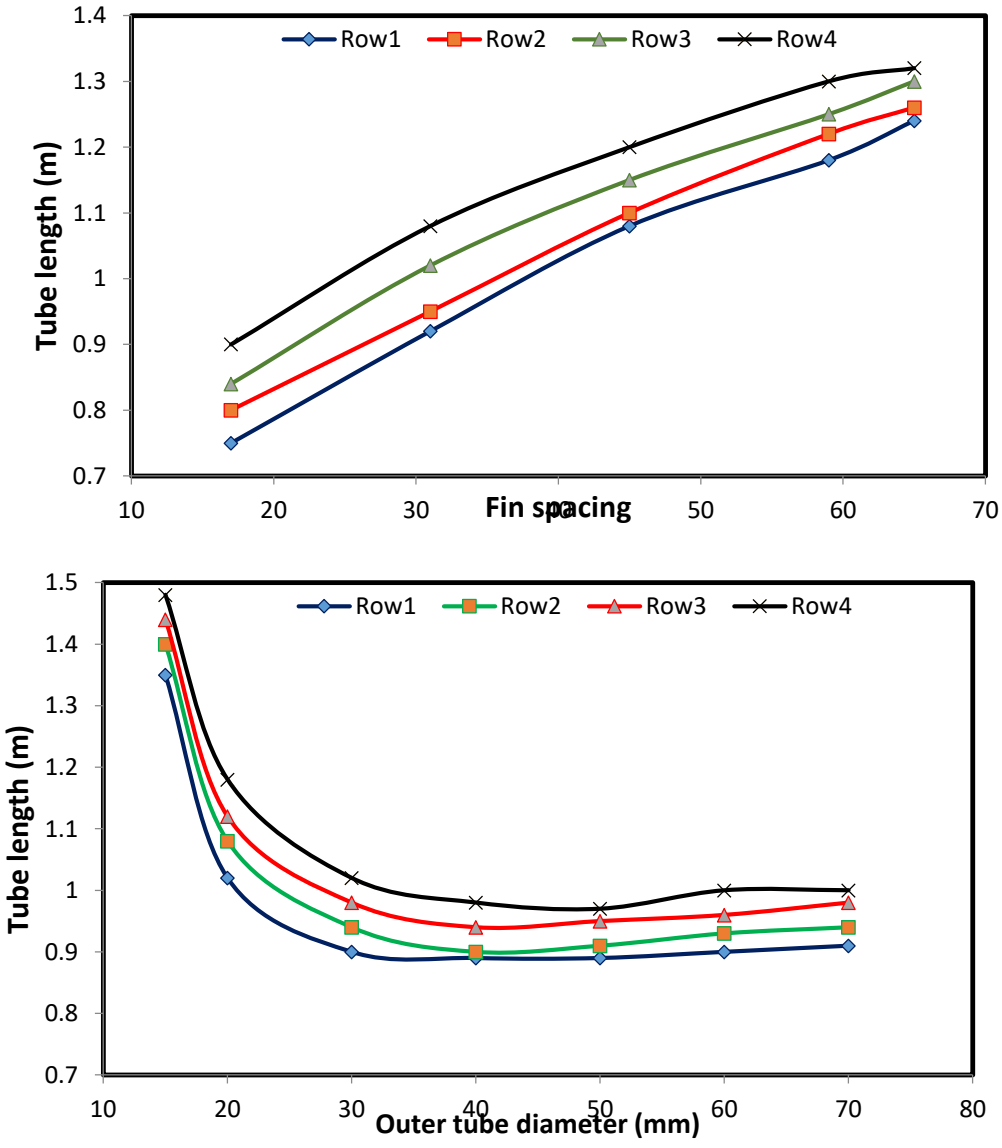

Figure 4.20 (a) Variation of fin spacing on tube length, (b) Effect of outer tube variation on tube length.

The cooling air velocity and temperature are also important parameters that need to be considered in the design as they help in selecting the size of fan for the cooling purpose. Figure 4.21a shows the air velocity influence on the absorption length. As the cooling air velocity increases, more heat can be removed from the tube surface as quickly as possible, thereby reducing the time taken to complete the absorption process. On the other hand, an increase in the air temperature causes an increase in the absorption length as depicted in Fig. 4.21b. This is because as the temperature of the cooling air increases, its capacity to carry away heat over the hot tube reduces thereby causing the absorption process to slow as it progresses from the bottom of the tube to the top.

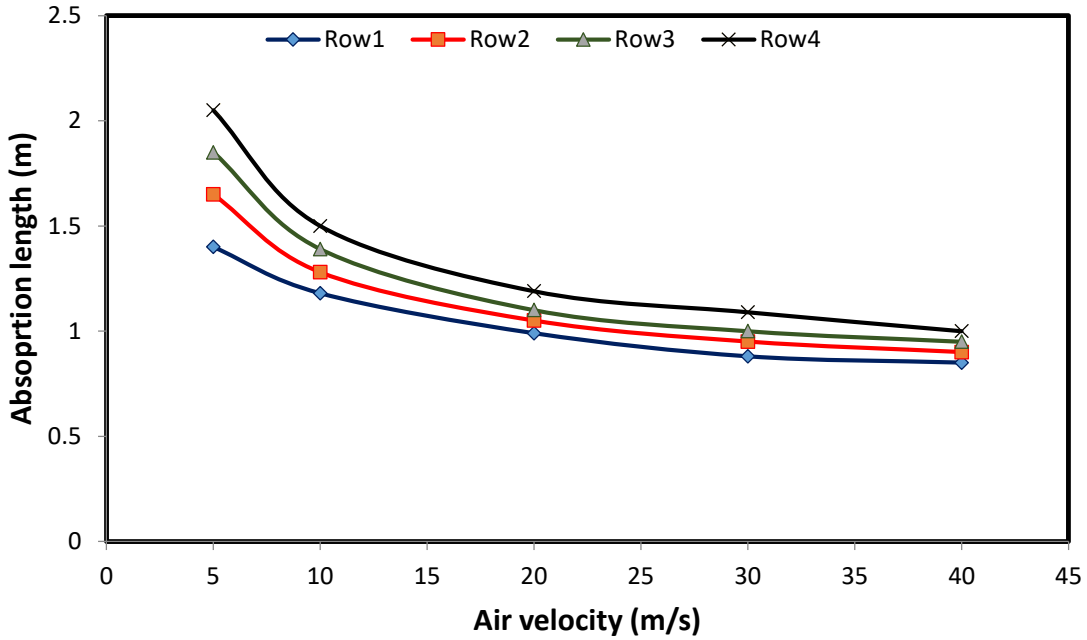

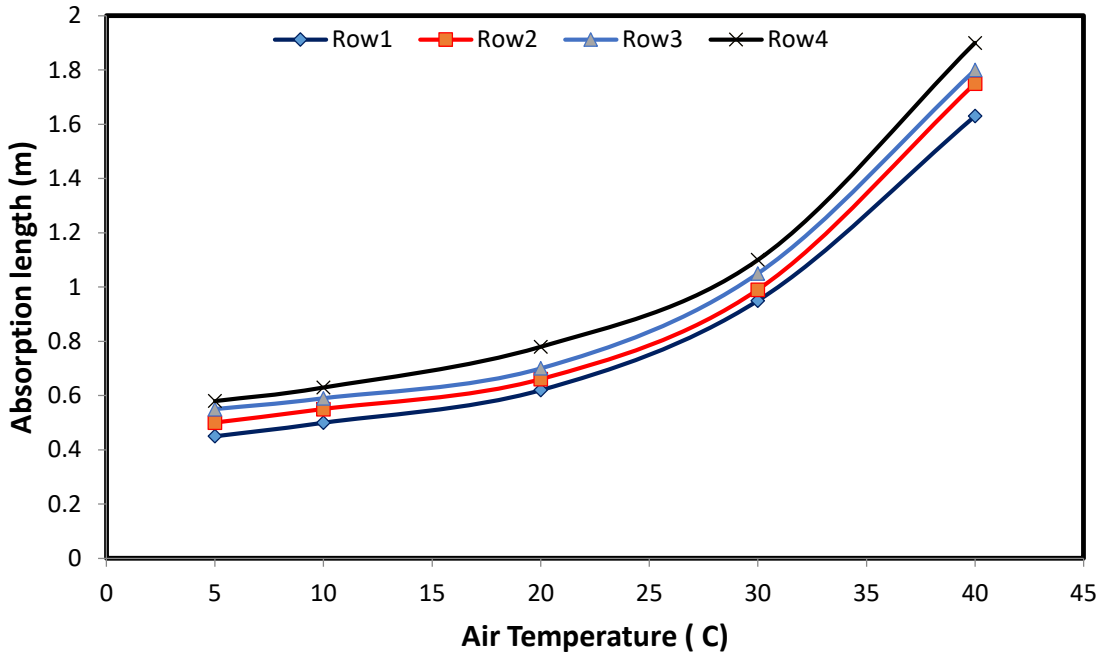

Figure 4.21 (a) Air velocity variation against absorption length, (b) air temperature influence on absorption length.

The effect of the tube spacing, called the pitch, likewise influences the performance of the absorber. As in Fig. 4.22, it is seen that as the pitch increases the absorption length of the tube reduces but up to an optimum point where the absorption length increases again. This is because as the pitch increases the finned tube surface area increases with constant air velocity reducing the volume of air available for cooling thereby reducing the air side heat transfer coefficient.

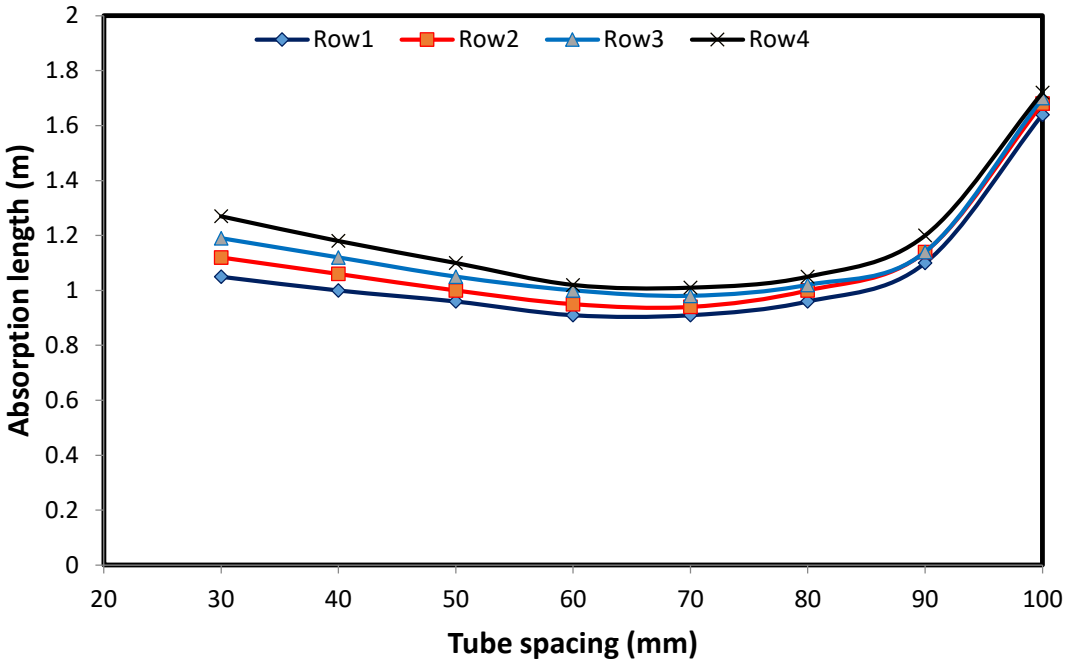

Figure 4.22 Effect of Pitch/tube spacing on Absorption length.

Furthermore, the interface and bulk liquid ammonia molar concentrations change as the absorption process progresses from the bottom of the tube to the top. As indicated in Fig. 4.23, the ammonia molar concentration of the bulk liquid increases along the tube length to the top which is higher in the churn and slug region than the bubbly region. The same scenario can also be noticed with interface liquid molar concentration but its value remains higher than that in the bulk liquid.

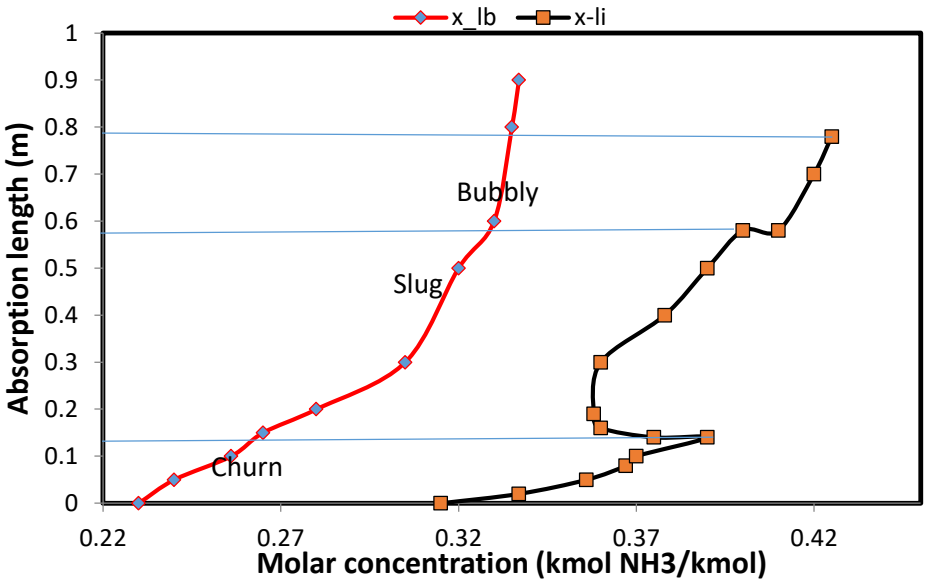

Figure 4.23 Molar concentration profile at the interface and bulk liquid phase.

Another parameter that is significant in the absorber design is the number of tubes. An increase in the number of tubes positively affects the absorption length and this is depicted in Fig. 4.24. It can also be deduced that as the number of tubes increases, the reduction in absorption length becomes less significant as it goes beyond a certain number. The adverse effect of this will be the large volume of material required for the shell side to hold all the tubes thereby increasing the space occupied by the absorber.

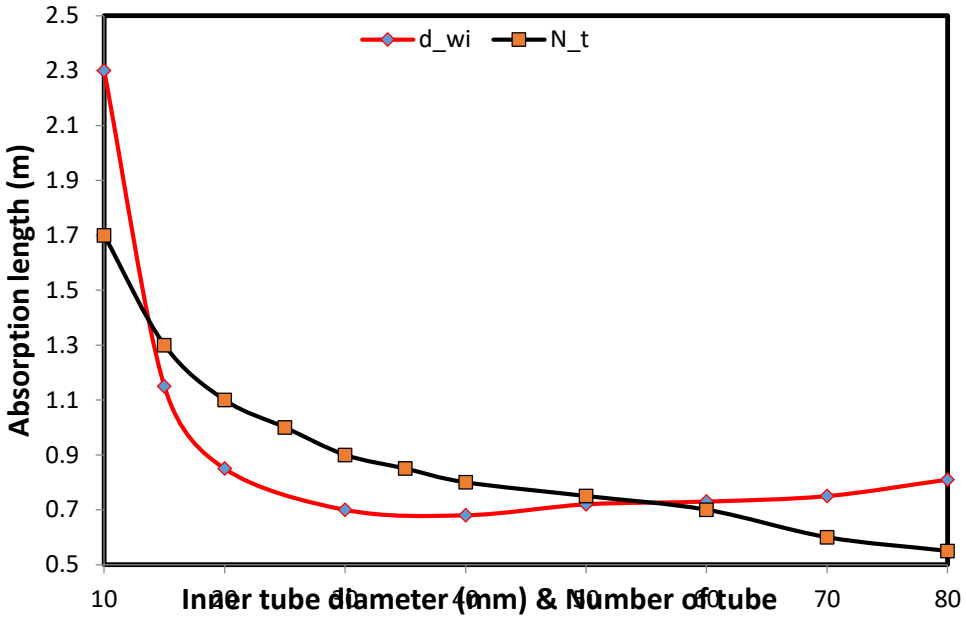

Figure 4.24 Number of tube and inner tube diameter influence on absorption length**.**

More so, an increase in the inner tube diameter also decreases the absorption length but negatively affects the absorption length beyond a certain point as it starts increasing again as seen in Fig. 4.23. Hence, there must be a compromise and technical decision taken to choose the inner diameter of the tube as it consequentially affects the absorption length. In this case, diameters above 40 mm negatively affect the absorption length. Therefore, there is a limit to which the diameter can be increased to get the shortest absorption length taken into consideration the effect it has on the absorption process and get a balance between material volume and absorber height.

4.4 Conclusions

A mathematical model has been developed for a helical coiled heat exchanger used as rectifier and a parametric analysis was carried out. Results showed that an increase in ammonia inlet temperature increased the heat transfer rate and effectiveness while an increase in the outlet temperature decreased the heat transfer rate and effectiveness. An increase in the helix diameter reduced the heat transfer rate in the coil side. It was also gathered that increasing the pitch reduces not only the number of turns of the coil and the length but also the heat transfer rate in the annulus and overall heat transfer coefficient.

There was an increase in the heat transfer rate at the coil side and in overall heat transfer coefficient when the coil inner diameter was increased. While an increase on the outer diameter of the coil reduced the heat transfer at the coil side but increased the heat transfer rate at the annulus. It also showed that an increase in the mass flow rate of ammonia increased the heat transfer rate at the annulus and overall heat transfer coefficient. Furthermore, increasing the mass flow rate of the solution increased the heat transfer rate at the coil side and overall heat transfer coefficient. More so, an increase in the inside diameter of the outer cylinder increased the volume available for fluid flow in the annulus but reduced both the heat transfer rate at the annulus and overall heat transfer coefficient.

A mathematical model was also built for a vertical tubular absorber that is cooled by air with ammonia-water as the working pair based on mass and energy balances and heat and mass transfer equations to analyse the absorption process along the tubes. The analysis has been made separately for the churn, slug and bubbly flow patterns that take place in the tubes during the absorption process.

The results showed how the absorption of the ammonia into the water progresses from the bottom of the tubes to the top in the absorber. It was vividly seen that the absorption length in each row was different due to the temperature of the cooling air. As the cooling air flows over the tubes it takes away the heat from the first row of tubes thereby exiting at higher temperature which becomes the inlet to the next row and so on. In view of this, the heat transfer rate of air reduces hence the increase in the absorption length in the preceding rows. This phenomenon was clear from the results as the last row had the highest absorption length hence becoming the absorber height. There existed simultaneous heat and mass transfer in the tubes during the absorption process thereby causing changes to the liquid phase temperature and that of the cooling air to take place. The liquid phase temperature reduced from the bottom of the tube and in the churn flow region, but tended to increase at the beginning of the slug flow region due to the heat and mass transfer reactions that took place before reducing again.

It was also depicted that fin spacing had important role to play in the sizing of the absorber. An increase in the fin spacing increased the absorption length and vice versa, nonetheless there was a limit to which the fin spacing could be reduced which depended on the available manufacturing technology. Furthermore, an increase in the outer tube diameter decreased the absorption length but also deteriorated at smaller outer diameter. Increased outer diameter will require large volume of metal for the manufacture of the tubes. The results also showed that a decrease in the air velocity increased the absorption length as the rate of heat removal was reduced due to low air velocity.

An increase in the tube spacing also reduced the absorption length but tended to increase it beyond a certain point, therefore there was an optimum point for the tube spacing. This was caused by the reduced volume of air available for cooling due to larger finned tube surface in increased tube spacing. It was also shown that the liquid bulk molar concentration increased as

the absorption process progressed from the bottom to the top of the tube, so also was the molar concentration of ammonia at the interface. Besides, this increase was higher in the churn flow region than in the slug and bubbly flow regions. The molar concentration at the interface was always higher than that in the bulk liquid.

An increase in both the number of tubes and inner tube diameter reduced the absorption length but there was a limit to which the inner diameter of tube could be increased beyond which the absorption length began to increase. It was shown from the analysis that the maximum inner tube diameter was 40 mm. On the other hand, increasing the number of tubes also made the absorber large, thereby increasing the volume of material used and compactness of the absorber would not be achieved.

5 Chapter 5

SYSTEM LEVEL MODELLING OF VAPOUR ABSORPTION REFRIGEARTION SYSTEM

This section considers the system level modelling of a one stage vapour absorption refrigeration system (VARS) followed by an investigation into the influence of various component operating parameters on the complete system. VARS is one that is driven by an external heat source which could either be from a direct gas burner, heat from solar energy or other means. Exhaust waste heat of a fuel cell is intended to be used in this case. A schematic of the proposed VARS and state points used in calculations is shown in Figure 5.1. Ammonia-water (NH_3H_2O) solution is the working pair used for this study where ammonia is the refrigerant and water is the absorbent. The single stage VARS works thus: at state point 1 NH_3H_2O solution is pumped into the desorber using a solution pump for pressurising the system. It is heated with waste exhaust heat from the fuel cell leading to desorption of ammonia vapour. As there could be some water vapour present in the evaporated ammonia, it is passed through a rectifier or vapour separator where pure ammonia is separated completely from the water vapour at state point 7, rejecting heat. The pure ammonia of about 99% concentration then flows into the condenser at point 9 where more heat is rejected and cools down to saturated liquid ammonia at point 10. The liquid ammonia passes through the refrigerant heat exchanger where it transfers heat to the vapour leaving the evaporator and further through an expansion valve at point 11 through to 12 before entering the evaporator. The refrigerant valve helps in reducing the high pressure liquid to lower pressure to allow evaporation.

The liquid ammonia at point 12 gains heat from the cooled space and exits as ammonia vapour at state point 13 to the absorber through the refrigerant heat exchanger where it mixes back with the water vapour leaving the rectifier to form a strong solution at point 1 and is then pumped back to the desorber for a repeat of the cycle. The mixing of the ammonia vapour and weak solution at the desorber produces heat which is rejected to the surrounding by a fan if it is an air cooled system as would be for this case.

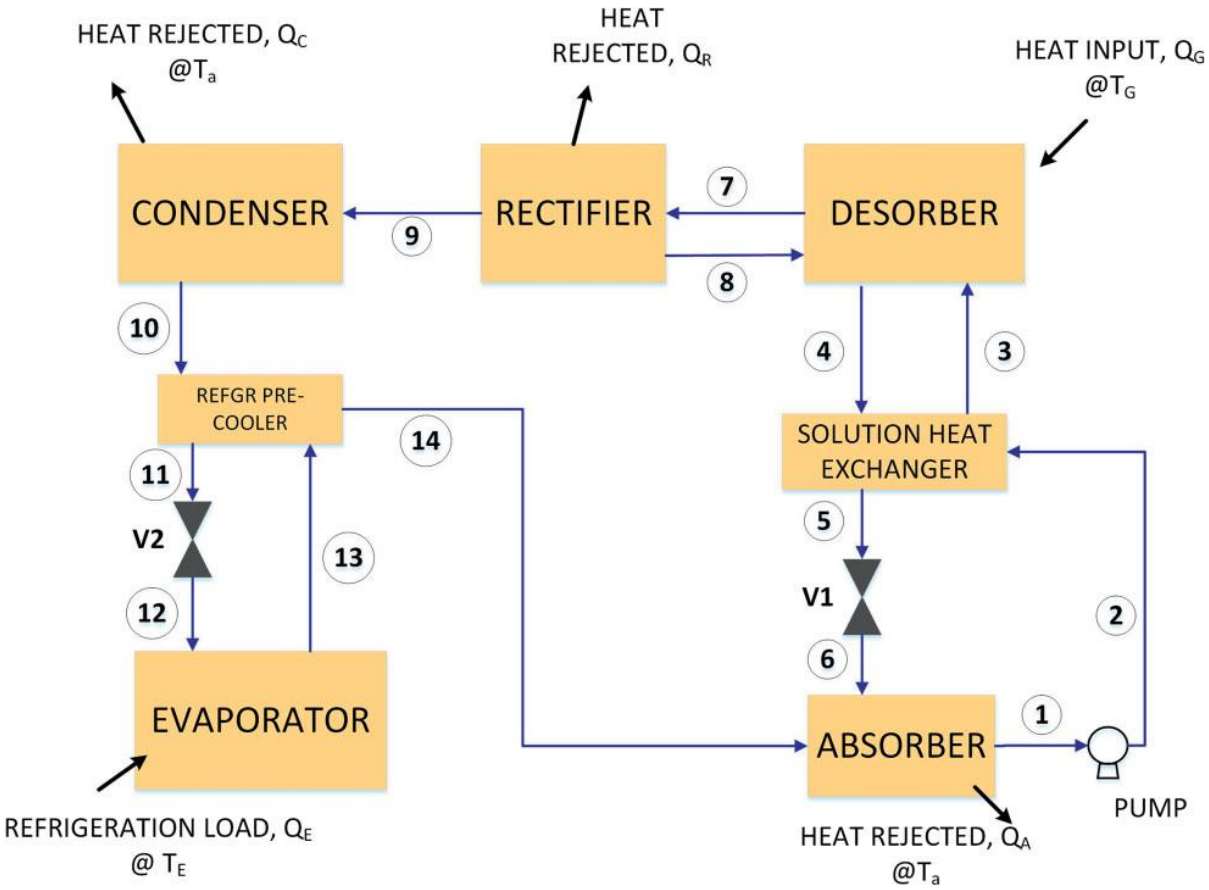

Figure 5.1Schematic of single stage vapour absorption system [5]

The flows at different state points within the cycle and assumptions made are as follows:

- pure ammonia vapour flows at state points 9, 13 and 14,
- condensed water with minute fraction of ammonia flows at state point 8,
- ammonia vapour mixed with water vapour flows at state point 7,
- weak solution (poor in ammonia) flows at state points 4, 5 and 6, and the concentration at these points are the same,
- ammonia liquid flows at state points 10, 11 and 12,
- Strong solution (rich in ammonia) flows at state points 1, 2 and 3, with the same concentrations,
- all the conditions are based on steady state,
- pressure drops in components and pipes are negligible,
- heat exchange occurs only at the absorber, desorber, rectifier, condenser, and evaporator,
- Pumps and expansion valves are frictionless or generate minimum heat so partial evaporation does not occur due to boiling.

Mass and energy balances were applied to each component being expressed here as a black box and the equations for each block were solved simultaneously using Engineering Equation Solver. Evaporator temperature was set at 15^{o}C as the system was first modelled for air-conditioning purposes and later set to -20^{o}C for refrigeration. Table 5.1 gives a detailed set of equations for each component.

Table 5.1 Mass and Energy balance Equations for VARS components.

Mass balance at Absorber	$\dot{m}_1 x_1 = \dot{m}_{14} x_{14} + \dot{m}_6 x_6$ $\dot{m}_1 = \dot{m}_{14} + \dot{m}_6$
Energy balance at Absorber	$\dot{m}_6 h_6 + \dot{m}_{14} h_{14} = Q_a + \dot{m}_1 h_1$
Mass balance for Pump	$\dot{m}_1 = \dot{m}_2$
Energy balance for Pump	$\dot{m}_1 h_1 + W_P = \dot{m}_2 h_2$
Pump Work	$WP = \dot{m}1 v1 (\frac{p2-p1}{\eta p})$
Mass balance for Solution Heat Exchanger*	$\dot{m}_4 = \dot{m}_5$ $\dot{m}_3 = \dot{m}_2$
Energy balance for Solution Heat Exchanger	$\dot{m}_4 h_4 + \dot{m}_2 h_2 = \dot{m}_5 h_5 + \dot{m}_3 h_3$
Mass balance at Desorber	$\dot{m}_8 x_8 + \dot{m}_3 x_3 = \dot{m}_7 x_7 + \dot{m}_4 x_4$ $\dot{m}_8 + \dot{m}_3 = \dot{m}_7 + \dot{m}_4$
Energy balance at Desorber	$\dot{m}_8 h_8 + \dot{m}_3 h_3 + Q_G = \dot{m}_7 h_7 + \dot{m}_4 h_4$
Mass balance at throttle valve V1	$\dot{m}_6 = \dot{m}_5$
Energy balance at throttle valve V1	$\dot{m}_6 h_6 = \dot{m}_5 h_5$
Mass balance at Condenser	$\dot{m}_9 = \dot{m}1_0$
Energy balance at Condenser	$\dot{m}_9 h_9 = \dot{m}_{10} h_{10} + Q_C$
Mass balance at Refrigerant pre-cooler	$\dot{m}_{10} + \dot{m}_{13} = \dot{m}_{11} + \dot{m}_{14}$
Energy balance at Refrigerant pre-cooler*	$\dot{m}_{10} h_{10} + \dot{m}_{13} h_{13} = \dot{m}_{11} h_{11} + \dot{m}_{14} h_{14}$
Mass balance at throttle valve V2	$\dot{m}_{11} = \dot{m}_{12}$
Energy balance at throttle valve V2	$\dot{m}_{11} h_{11} = \dot{m}_{12} h_{12}$
Mass balance at Evaporator	$\dot{m}_{12} = \dot{m}_{13}$
Energy balance at Evaporator	$\dot{m}_{13} h_{13} = \dot{m}_{12} h_{12} + Q_E$
Mass balance at Rectifier	$\dot{m}_7 x_7 = \dot{m}_9 x_9 + \dot{m}_8 x_8$ $\dot{m}_7 = \dot{m}_9 + \dot{m}_8$
Energy balance at Rectifier	$\dot{m}_7 h_7 = \dot{m}_9 h_9 + \dot{m}_8 h_8 + Q_R$

Where

$\dot{m}_{1----14}$ *Mass flow rates at various state points (kg/s)*

$h_{1----14}$ *Enthalpy at various state points (kJ/kg)*

Q_C *Heat rejected at the Condenser (kW)*

Q_G *Heat added at the Generator (kW)*

Q_E *Heat added at the evaporator/cooling load (kW)*

Q_a *Heat rejected at the absorber (kW)*

Q_R *Heat rejected at the Rectifier (kW)*

x *Ammonia mass fraction or concentration (wt%)*

v *specific volume of solution (m^3/kg)*

W_p *Work done by pump (kW)*

ηp *Pump efficiency (%)*

5.1 Coefficient of performance of vapour absorption refrigeration system (VARS)

There are two forms of the Coefficient of Performance for the system, one of which is the overall and the other is in terms of thermal energy only. These are calculated by Eqs. 5.1 and 5.2. Therefore, the COP of VARS can be defined as the ratio of the evaporator load to either the sum of the heat input and the pump work or just the heat input, as the case may be.

$$COP_{Overall} = \frac{Q_E}{Q_{G+}W_p} \quad \text{Eq. 5.1}$$

$$COP_{Thermal} = \frac{Q_E}{Q_G} \quad \text{Eq. 5.2}$$

The ammonia concentration is calculated from the following relationship by fixing the pressure and rejection temperature of the absorber

$$\log P = A - \frac{B}{T} \quad \text{Eq. 5.3}$$

Where

P *Operating pressure of the absorber (kPa)*

T *Exit temperature of the absorber (kPa)*

And

$$A = 7.44 - 1.767\,x + 0.9823\,x^2 + 0.3627\,x^3 \quad \text{Eq. 5.4}$$

$$B = 2013.8 - 2155.7\,x + 1540.9\,x^2 - 194.7\,x^3 \quad \text{Eq. 5.5}$$

The operating conditions or parameters for the base case are given in table 5.2, and were chosen based on practically achievable/expected figures, e.g. 15^{o}C for the evaporator exit temperature was chosen as expected for air-conditioning in reality, and 0.99 for the purity of ammonia at rectifier exit and evaporator/absorber inlet.

Table 5.2 Operating conditions set for base case system level modelling of VARS.

Absorber exit temperature	40^{o}C
Absorber/Evaporator pressure	1 bar
Condenser exit temperature	40^{o}C
Condenser/Desorber pressure	15 bar
Evaporator exit temperature	15^{o}C
Solution heat exchanger effectiveness	0.8
Refrigerant heat exchanger effectiveness	0.8
Pump efficiency	0.7
Ammonia mass fraction at rectifier exit/RHX exit	0.99
Ammonia mass fraction at evaporator inlet/ absorber inlet	0.99
Vapour quality at rectifier inlet/outlet	1
Vapour quality at evaporator outlet	0.998
Vapour quality at condenser exit	0
Vapour quality at state points 4 and 8	0
Mass flow rate of strong solution (kg/s)	0.0072

The results from the base case modelling of the VARS for a 1kW evaporator load is given in Table 5.3 at an evaporator temperature of 15^{o}C. These results were obtained from EES with the initial operating conditions as given in Table 5.2. EES was able to calculate all parameters

at any state point showing the quality of vapour or liquid, heat ejected or gained, and evaporator load.

Table 5.3 Output from base case simulation.

SP	ṁ(g/s)	T(°C)		VACS Parameters	Cooling load 1kW
1	7.2	40		Model cooling load (kW)	1.026
2	7.2	40.23		Desorber heat input (kW)	2.388
3	7.2	138.7		Condenser heat rejected(kW)	1.051
4	6.36	163.4		Absorber heat rejected(kW)	1.771
5	6.36	48.19		Rectifier heat rejected(kW)	0.6079
6	6.36	48.48		Work done by pump(kW)	0.01588
7	1.086	137.9		Refrigerant mass flow rate (g/s)	0.8401
8	0.2458	148.6		Strong solution mass flow rate (kg/s)	7.2
9	0.8401	75.95		Weak solution mass flow rate (g/s)	6.36
10	0.8401	40		COP(*thermal*)	0.4296
11	0.8401	25.88		COP (overall)	0.4267
12	0.0008401	-33.36		Strong solution concentration	0.233
13	0.8401	15		Weak solution concentration	0.133
14	0.8401	35			

From Table 5.3, with the initial set values, the overall and thermal COP were calculated as 42.67 and 42.96% respectively with heat input of 2.388kW while the heat rejection at the

condenser was 1.051kW. More so, results from the base case also show that the concentrations of the strong and weak solutions were 23.33 and 13.33% respectively as this was the target set from the modelling equations for desorption of ammonia from the strong solution to take place as explained further in section 5.2.7. The heat rejected at the absorber, rectifier, and condenser were 1.771, 0.6079, and 1.051 respectively. This rejected heat could be recycled back to the solid oxide fuel cell (SOFC) for pre-heating of the fuel and air entering the stack

5.2 Effect of operating conditions on Coefficient of Performance

As the COP for the base case is about 42% there is need to find strategies to improve the overall performance of the system by altering operating conditions to see which parameters/operating conditions are most influential so that the system can be optimised based on these findings.

5.2.1 Variation of Solution Heat Exchanger Effectiveness

Figure 5.2 shows the effect of varying the effectiveness of the solution heat exchanger (SHX) on other components. It can be deduced that the increase in the SHX effectiveness has no effect on the condenser heat rejected, and heat intake at the evaporator. This is due to no changes caused by the variation of the SHX effectiveness on flow rates and temperatures in and out of the condenser and evaporator. On the other hand, there is a drastic reduction in the heat added at the desorber and that rejected at the absorber. There is significant reduction in the heat that needs to be added at the desorber because an increase in the SHX effectiveness causes more heat to be transferred to the strong solution from the weak solution as they pass through the exchanger. This causes the strong solution temperature to be increased which in turn means less heat needed to heat up the ammonia for desorption. The same is applicable to the absorber

as the weak solution enters the absorber at reduced temperature after transferring the heat to the strong solution thereby reducing the heat to be rejected to the surrounding as the effectiveness of the solution heat exchanger increases.

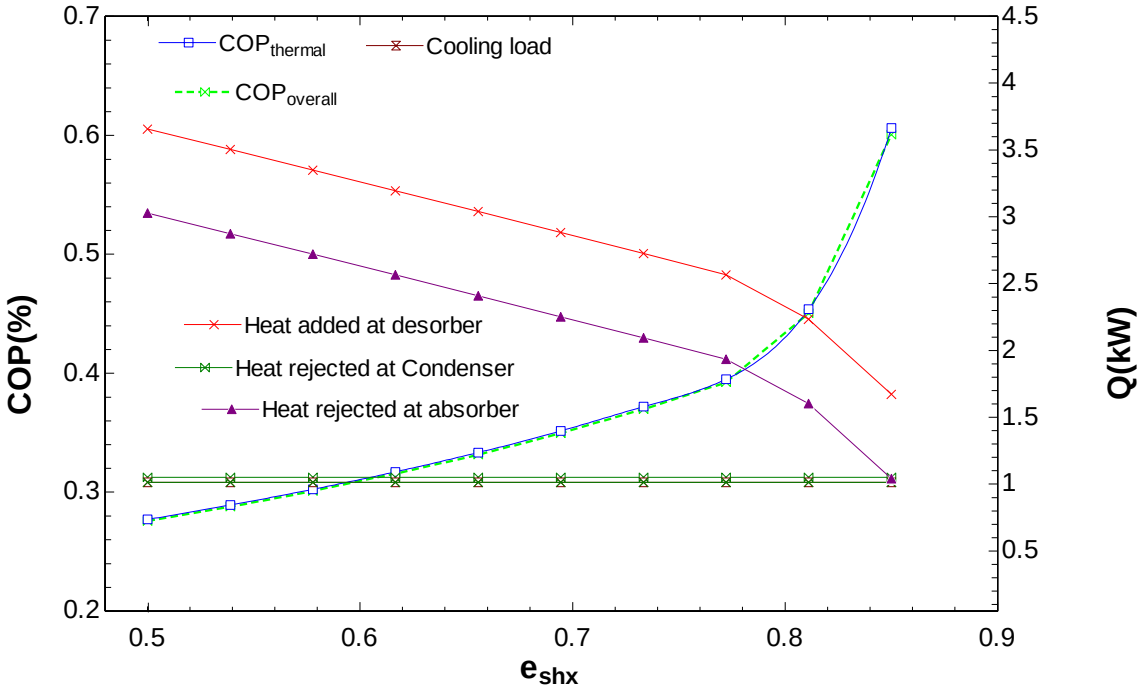

Figure 5.2 Solution heat exchanger effectiveness vs COP and heat load.

More so, an increase in the SHX effectiveness increases both the thermal and overall coefficients of performance. This is because, the thermal COP is a ratio of the evaporator load to the desorber added heat, and as the desorber heat is reduced while the evaporator load is constant, the thermal COP will actually increase. On the other hand, overall COP increases as well, as it is also the ratio of evaporator load to the sum of the desorber added heat and the pump work, but with evaporator load and pump work remaining the same and desorber heat being reduced due to the effectiveness increase of the SHX, the overall COP increases at about the same level as the thermal COP. This is evident as the heat input to the desorber is just 1.672kW as compared to the 2.388kW with the base case. More so, the heat rejected at the

absorber was reduced from 1.771kW to 1.041kW. Furthermore, COP (both thermal and overall) increased to 0.6061 and 0.6004kW from 0.4296 and 0.4267kW, respectively. In essence a 5% increase in the SHX effectiveness results in about 70% reduction in the desorber heat input and 41% overall COP increase.

5.2.2 Variation of absorber exit temperature

The effect of varying the exit temperature of the absorber on the evaporator load, heat input at the desorber, and COP (thermal and overall) is studied in this section. As seen in Fig. 5.3a, both overall and thermal coefficient of performance of the system increase with reduced absorber exit temperature. On the other hand, there is only little increase in cooling load, but a slow reduction in the heat needed to be added at the desorber is seen.

It is worthy of note that the temperature of the cooling medium for the absorber needs to be taken into consideration during the variation of the absorber exit temperature as it depends on that temperature (cooling medium). In the present study an air-cooled absorber is being considered, hence the ambient air temperature plays a crucial role in considering the limit to which the absorber temperature could be reduced. The ambient air is assumed to be at 30^{o}C, then the absorber temperature will be kept at 40^{o}C which is practically ideal for exchange of heat between the absorber and the cooling air as there should be at least 10^{o}K difference. If water were used as the cooling medium, say at a temperature of 5^{o}C, then the exit temperature could be reduced to about 15^{o}C which will lead to higher COP (both thermal and overall) as indicated in Figure 5.3a.

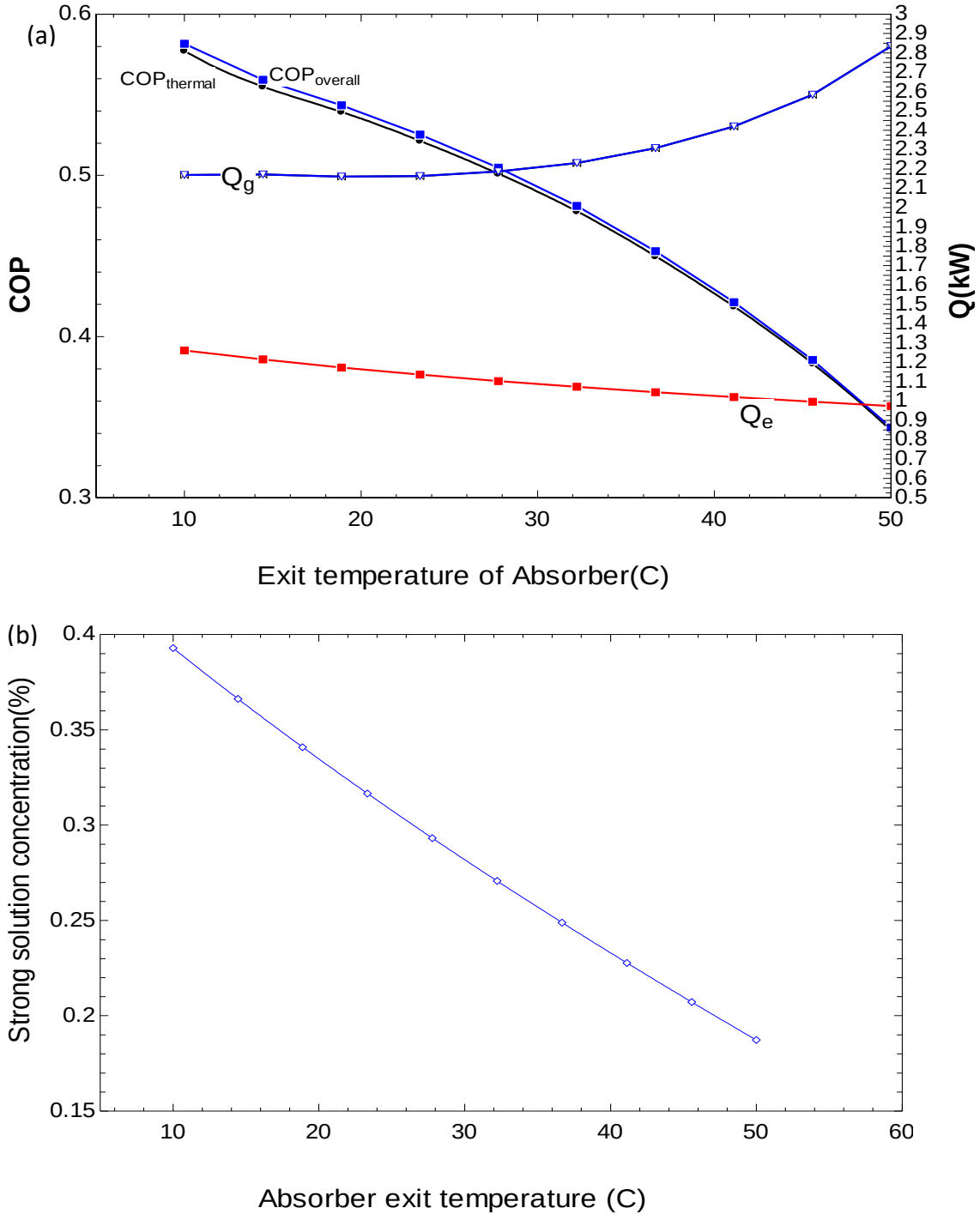

Figure 5.3 Absorber exit temperature influence on strong solution concentration, COP and heat load.

A reduction in the exit temperature of the absorber increases ammonia solubility leading to higher strong ammonia-water solution concentration which in turn increases the COP as evident in Fig. 5.3b due to more ammonia been vaporized at the desorber leading to an increase in amount of refrigerant for cooling. This is because the COP is directly proportional to the evaporator cooling load as seen in equation 5.1 and the cooling load is dependent on the mass flow rate as follows

$$Q_E = \dot{m}_{13} (h_{13} - h_{12}) \qquad \text{Eq. 5.6}$$

Therefore, as increased concentration causes an increase in ammonia flow rate, cooling load will eventually be increased, thereby increasing the COP.

5.2.3 Effect of condenser/desorber and evaporator/absorber pressures

When the desorber/condenser pressures are increased, the COP is reduced as shown in Figure 5.4. Increasing the absorber/evaporator pressure increases the COP due to the increase in concentration of the strong solution as shown in Fig. 5.5. It also shows the minimum condenser/desorber pressure at different absorber/evaporator pressures and the subsequent effect on the overall COP.

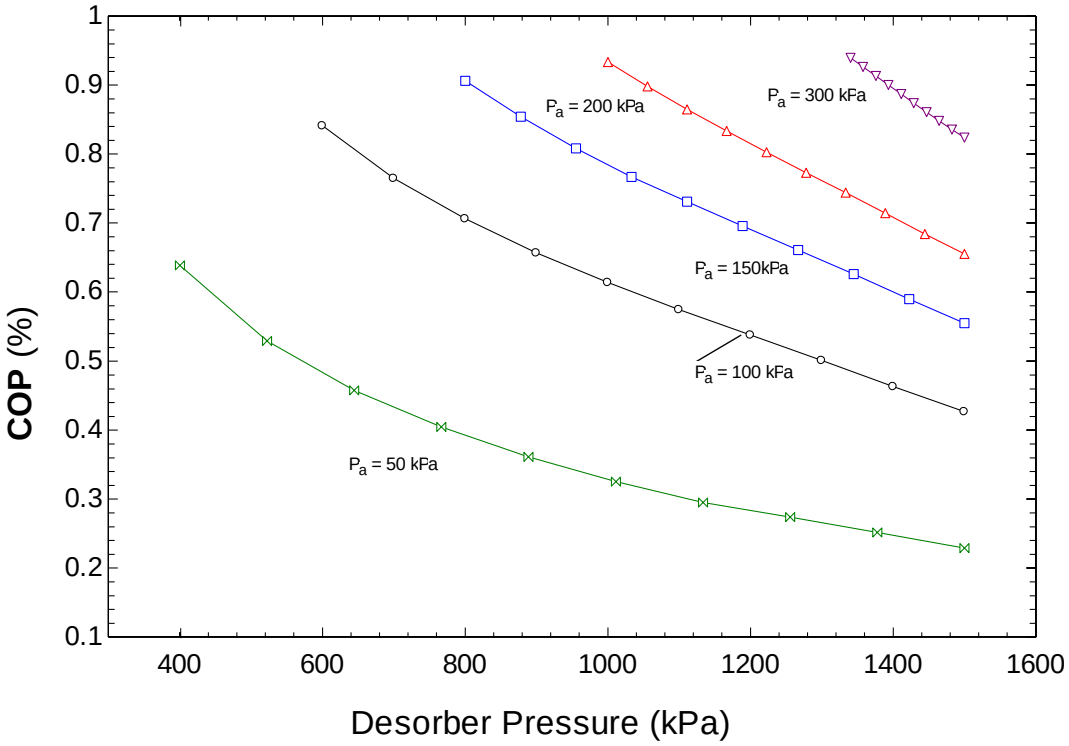

Figure 5.4 Desorber pressure effect on COP.

The effect of operating the system at varying absorber/evaporator pressures with every other parameter remaining constant as in the base case is depicted in Fig. 5.5. It can be seen that an increase in absorber/evaporator pressure increases the ammonia concentration in the strong solution. The COP increases as well. But there is a limit to which the pressure can be increased beyond which the COP is greater than 1. It should be noted that at high absorber/evaporator pressures the COP becomes greater than 1 which is not feasible as the VARS modelled here is a single stage type and cannot be greater than 1. Further analysis shows that the pressure cannot rise beyond 405 kPa at which the COP is greater than 1 in the base case. In essence, the maximum pressure could be set at 400 kPa which gives a COP of 0.9883 with an ammonia concentration of 0.4491. Interestingly, when the absorber/evaporator pressure is increased beyond 750 kPa, the inlet temperature of the evaporator becomes greater than the outlet which

is not supposed to be the case as there is heat input at the evaporator which means the exit temperature should be greater than the inlet. But it should be noted that at this same pressure of 750 kPa the COP is about 1.945 which is not practically feasible. As said earlier the pressure was adjusted to 400 kPa where the COP was in the range of acceptability and the temperature difference between the inlet and the outlet of the evaporator was 276.08 K.

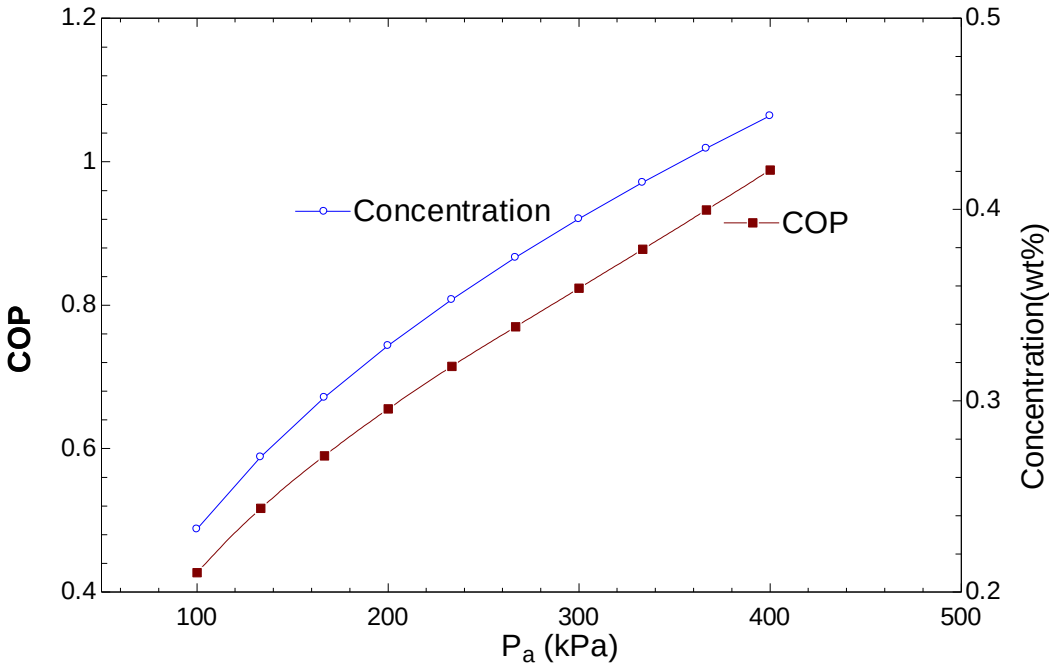

Figure 5.5 Absorber pressure influence on the COP and solution concentration.

At any specific desorber pressure there is a maximum absorber pressure beyond which the COP is greater than 1. Table 5.4 shows the maximum absorber pressure at any given desorber pressure and the corresponding ammonia concentration. This analysis is presented graphically in Figure 5.6.

Table 5.4 Maximum Absorber/Evaporator pressure at specific Desorber pressure

Desorber pressure (bar)	Maximum Absorber pressure (bar)	COP at maximum absorber pressure	Concentration (%)
15	4	0.988	44.9
13	3	0.969	39.5
11	2.4	0.976	35.8
9	1.9	0.972	32
7	1.52	0.996	28.9

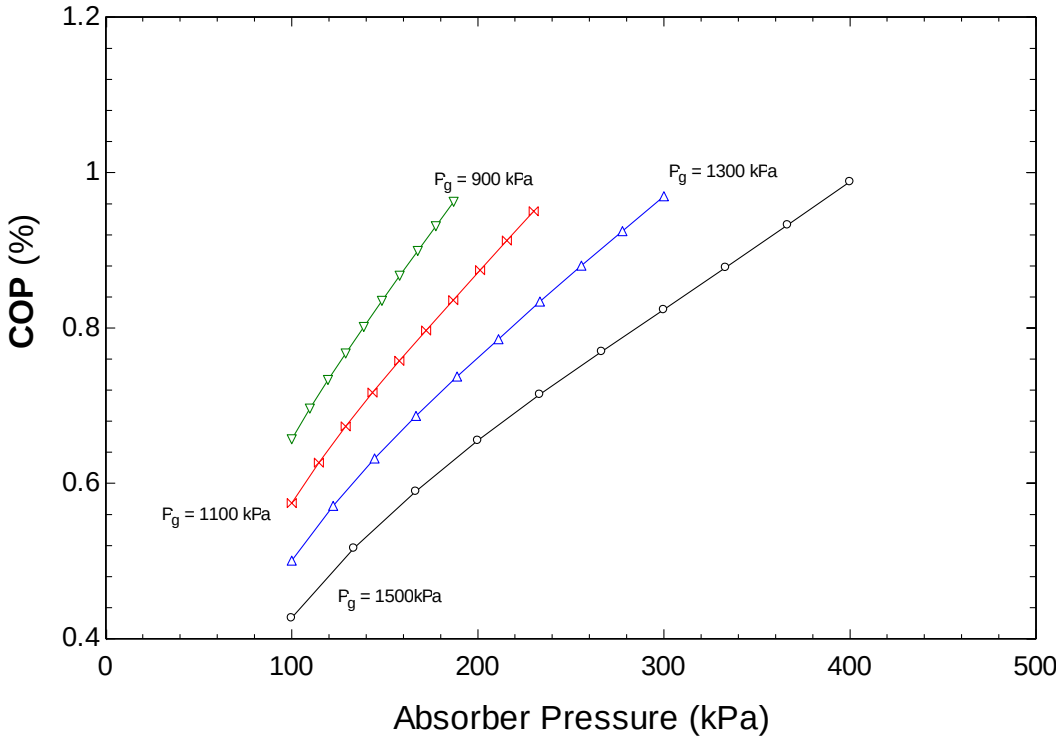

Figure 5.6 Variation of COP with absorber pressure at different desorber pressures**.**

5.2.4 Effect of Condenser Exit Temperature, Solution Pump Efficiency and Refrigerant Heat Exchanger Effectiveness

There is no significant effect caused by the refrigerant heat exchanger effectiveness on the overall COP, as can be seen in Figure 5.7b. More so, it can be seen that increasing the efficiency of the solution pump reduces the work to be done by the pump but does not have any effect on the overall COP as shown in Fig. 5.7a; hence operating the pump at higher efficiency is unnecessary as even at a lower efficiency nearly the same COP is achieved. This is because the overall COP is a function of the ratio of the cooling load to the sum of the heat input at the desorber and the pump work as in Eq. 5.1.

The pump work is inversely proportional to the pump's efficiency as given in Eq. 5.7

$$W_P = \dot{m}1 v_1 \left(\frac{p2-p1}{\eta p}\right) \qquad \text{Eq. 5.7}$$

It can be deduced from Eq. 5.7 that increasing the efficiency of the pump will reduce the pump's work while keeping every other parameter constant. This reduced pump work will not cause any significant change to the overall COP as it is negligible compared to the heat input at the desorber as shown in Eq. 5.1. This explains the reason of little significance in the changes of COP when the pump's efficiency is increased.

Furthermore, a reduction in the condenser exit temperature has only little effect on the overall and thermal coefficient of performance, hence varying it does not change the system performance as shown Fig. 5.7c

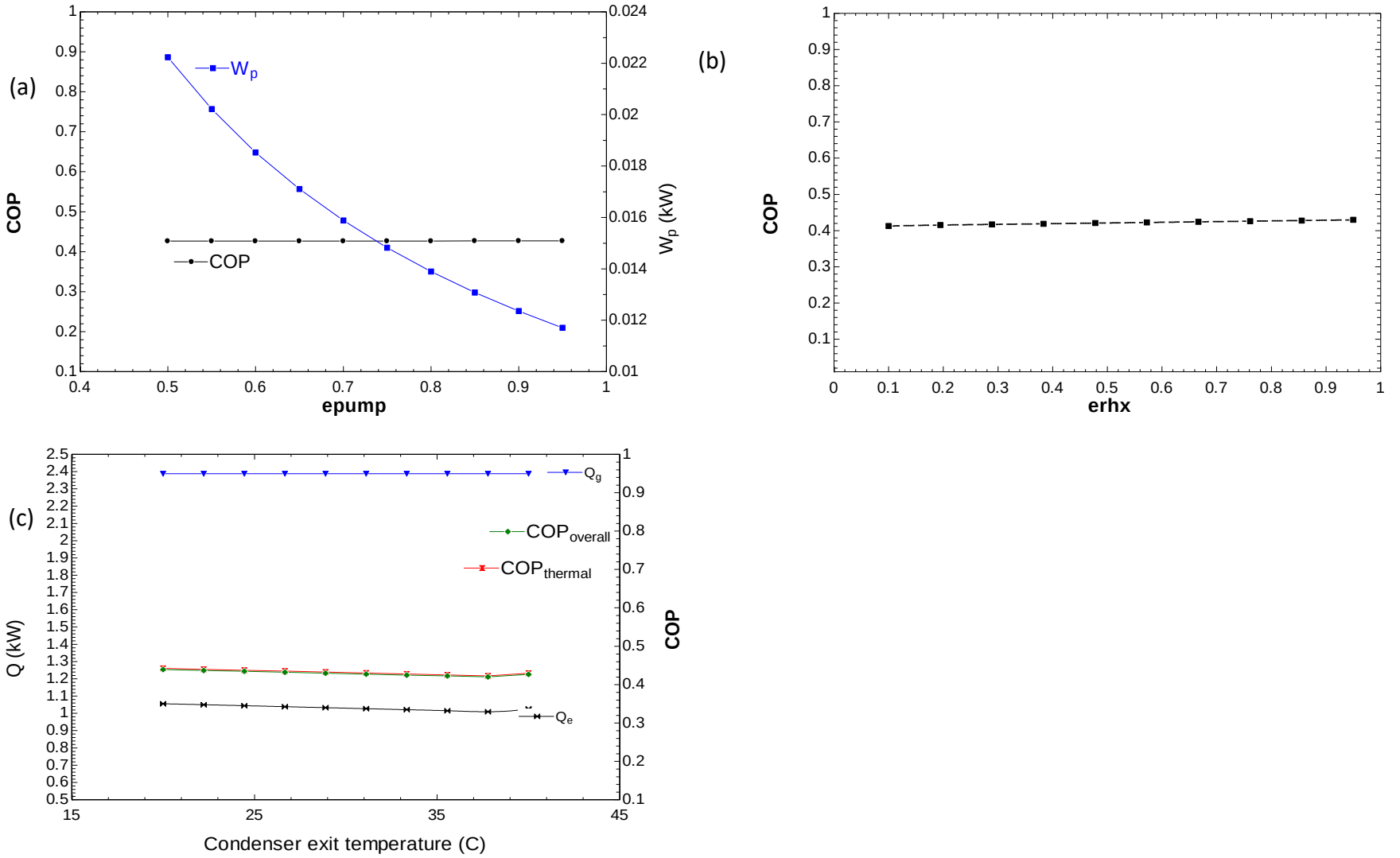

Figure 5.7 Variation of condenser exit temperature, refrigerant HX effectiveness and pump efficiency

5.2.5 Effect of Evaporator Temperature on COP, cooling load and heat input at Desorber

The effect of the variation of evaporator exit temperature on the COP, cooling load, and heat input at the desorber is shown in Fig. 5.8. Simulation results showed that there is no significant effect for the evaporator temperature on the cooling load, heat input, and COP.

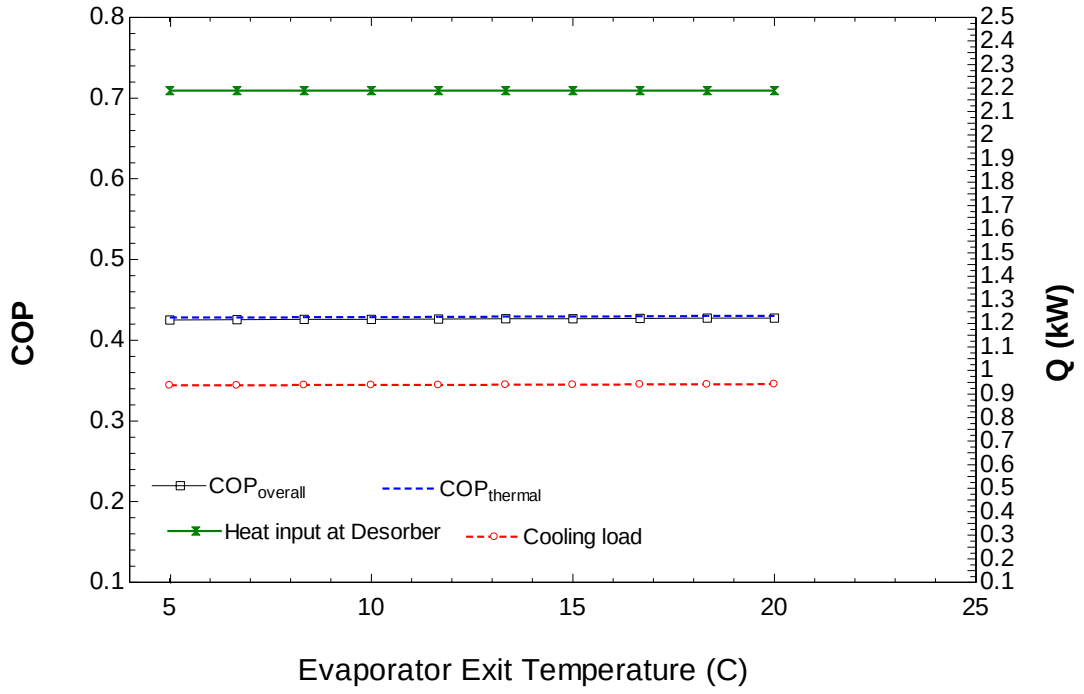

Figure 5.8 Variation of Evaporator temperatures with COP, Cooling load, and Heat Input

This is because during phase change, the thermal energy created is used for breaking the molecules (liquid to vapour) so the temperature does not have any significant effect but the entropy and enthalpy change. This can be explained with Eq. 5.8. Setting the outlet temperature of the evaporator at 15^{o}C results in outlet and inlet enthalpy (h_{13} and h_{12}) of 1329 and 107.3

respectively. When the temperature is set to -20^{o}C, it results in 1246 and 35.25 respectively for the outlet and inlet enthalpy. This implies that the enthalpy difference at 15^{o}C and -20^{o}C are 1221.7 and 1210.75, respectively. Substituting these values in Eq. 5.8 with the refrigerant flow rate been constant gives 1.082 and 1.073 respectively of cooling or evaporator load at 15^{o}C (air-conditioning) and -20^{o}C (refrigeration). From the foregoing, it can be seen that there is no significant effect of the evaporator temperature on the cooling or evaporator load which explains why there is no COP change whether the vapour absorption cooling system is operated in air-conditioning or refrigeration mood.

5.2.6 Variation of mass flow rate of strong solution

With every other parameter remaining constant as in the base case, the effect of the variation of the mass flow rate on the cooling load is analysed here. It can be seen in Figure 5.9a that increasing the mass flow rate of the strong solution increases the cooling load but has no effect on the COP of the system. The reason for this is that there is an increase in the mass flow rate of the refrigerant that goes into the evaporator thereby increasing the cooling load. This phenomenon can be best explained with equation 5.8

$$Q = \dot{m} * h_{13\text{-}12} \qquad \text{Eq. 5.8}$$

Where

Q	Cooling load (kW)
$\dot{m}$	Mass flow rate of the refrigerant at the evaporator, (kg/s)
$h_{13\text{-}12}$	Outlet and inlet enthalpy difference at the evaporator, (J/kg)

From above, as the cooling load is a function of the mass flow rate, and enthalpy difference, an increase in the mass flow rate of the refrigerant will increase the cooling load while the enthalpy difference remains constant. This process is also seen in the Figure 5.9b as the mass flow rate of the strong solution increases so does that for the refrigerant. As the mass flow rate of the refrigerant increases there is more refrigerant to be separated which results in higher heat input. In essence, with all conditions met for a particular load, every other parameter can be left constant while changing the mass flow rate of the strong solution can be used to control load fluctuations.

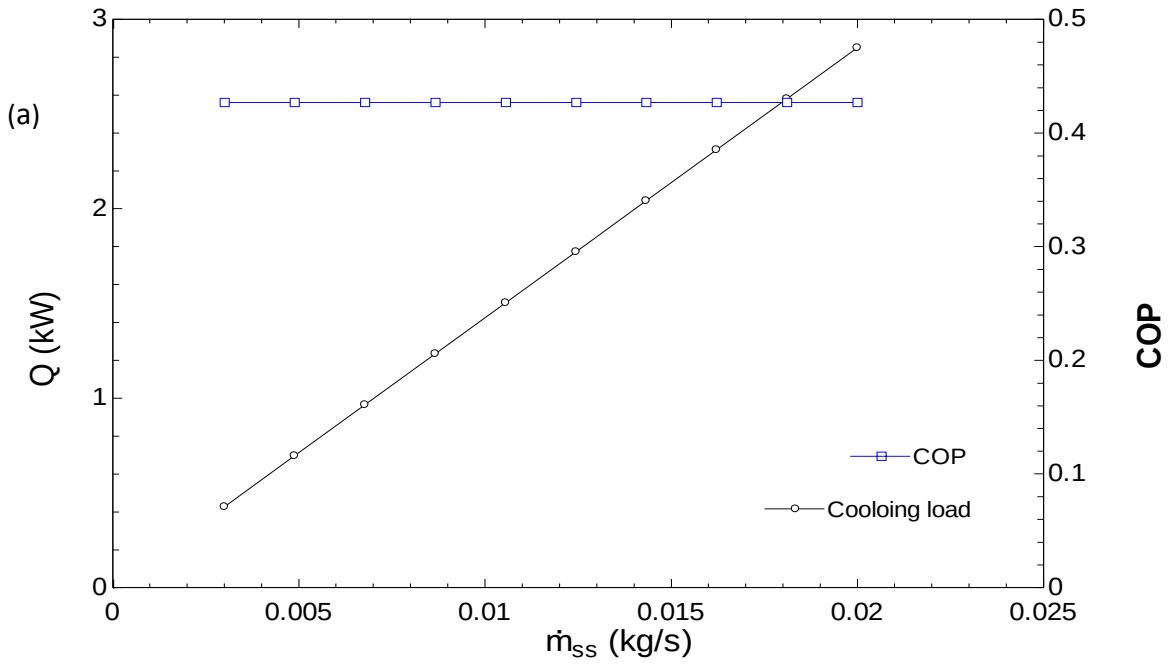

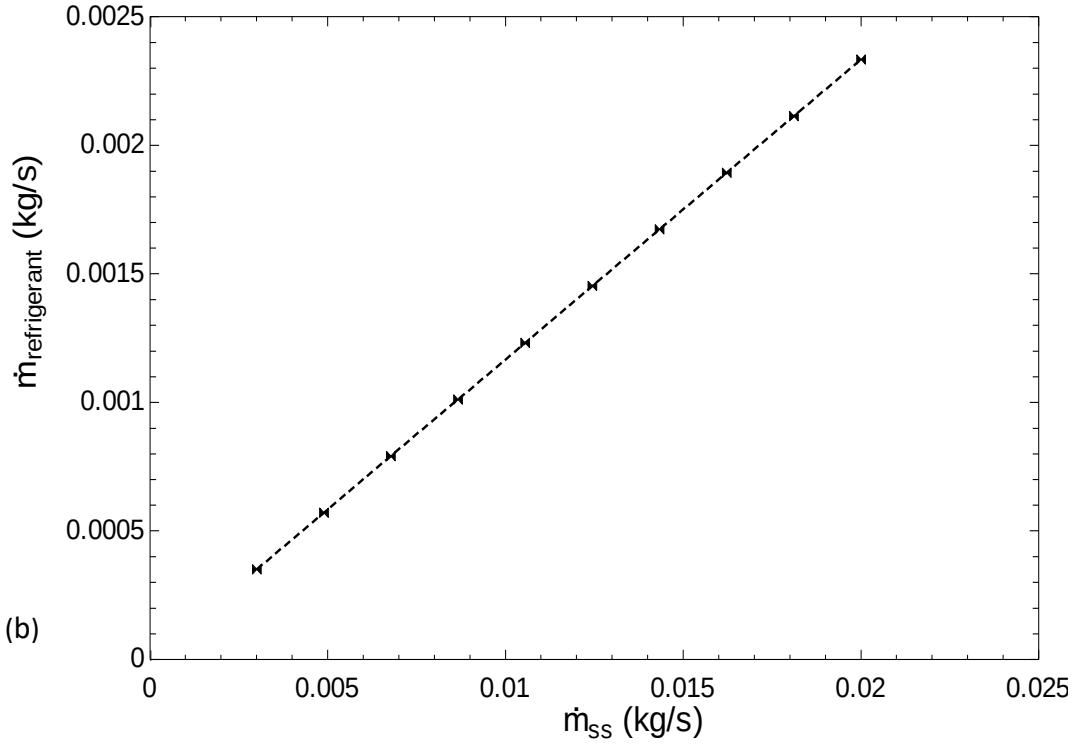

Figure 5.9 Variation of strong solution mass flow rate vs COP, cooling load, refrigerant mass flow rate.

5.2.7 Effect of Concentration difference between strong and weak solution

Figure 5.10 shows the effect of the concentration difference between the strong and weak solution on COP, cooling load, and heat input at the generator. As the difference between the two solutions increases so does the COP (thermal and overall) which is due to the increased mass flow rate of the refrigerant at the inlet of the evaporator leading to increasing cooling power as depicted in Fig. 5.9, thereby increasing the COP. For the ammonia vapour to be separated from the strong solution the minimum concentration difference should be 5% [148]. There is also a theoretical maximum limit of the concentration difference which was found from the simulation result to be 15% above which the temperatures in and out of the solution

heat exchanger of the returning weak solution becomes negative (state points 5 and 6). This might lead to freezing and hindering of the flow of the weak solution between the desorber and absorber.

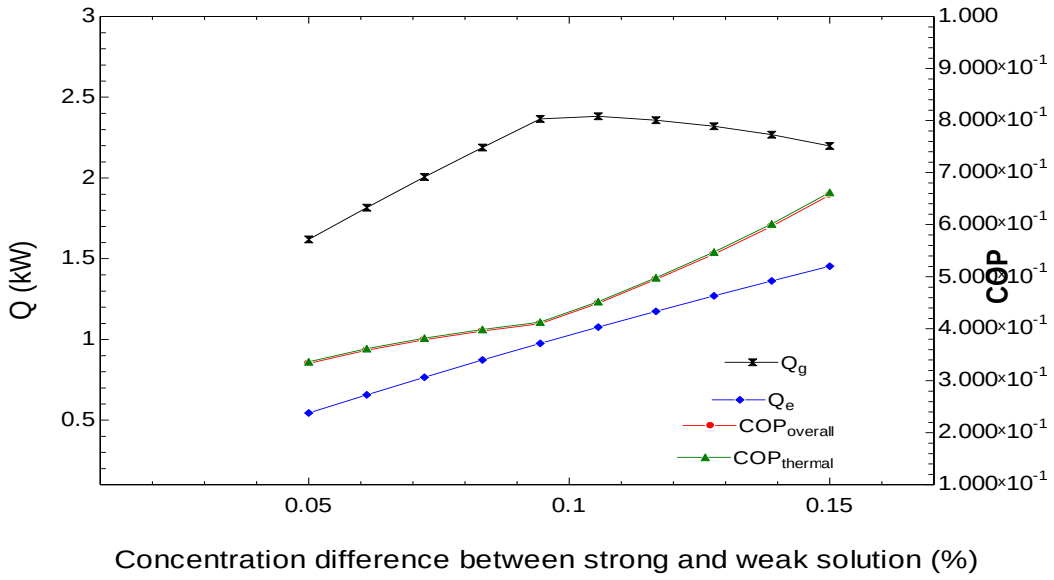

Figure 5.10 Variation of concentration difference between strong and weak solution.

5.2.8 Summary overview of the influence of operating parameters

It can be deduced from the simulation that every parameter has its own degree of influence on other parameters but the most influential are the absorber and desorber pressure, concentration difference, absorber exit temperature, and solution heat exchanger effectiveness. The final operating parameters for the system after the optimization processes to improve the COP are presented in Table 5.4.

Table 5.5 Final operating parameters after optimization.

Parameter	Value	State point
Absorber exit temperature	40^{o}C	1
Absorber/Evaporator pressure	1.5 bar	1
Condenser exit temperature	40^{o}C	10
Condenser/Desorber pressure	15 bar	2 to 5,7 to 10
Evaporator exit temperature	15^{o}C	
Solution heat exchanger effectiveness	0.86	
Refrigerant heat exchanger effectiveness	0.86	
Pump efficiency	0.7	
Ammonia mass fraction at rectifier exit/RHX exit	0.99	9
Ammonia mass fraction at evaporator inlet/ absorber inlet	0.99	12-14
Vapour quality at rectifier inlet/outlet	1	7,9
Vapour quality at evaporator outlet	0.998	13
Vapour quality at condenser exit	0	10
Vapour quality at state points 4 and 8	0	4,8
Mass flow rate of strong solution (g/s)	6.6	1-3

The results showing the mass flow rates and temperatures at various state points are given in Table 5.5 with the values of heat input, absorber heat rejected, condenser heat rejected, and that of the rectifier, among others

Table 5.6 Output for the final operating parameters.

SP	ṁ(g/s)	T(°C)		VAS Parameters	Cooling load 1kW
1	6.6	40		Model cooling load (Kw)	1.004
2	6.6	40.23		Desorber heat input (kW)	1.119
3	6.6	134.3		Condenser heat rejected(Kw)	1.028
4	5.778	149.6		Absorber heat rejected(kW)	0.7899
5	5.778	12.14		Rectifier heat rejected(kW)	0.3193
6	5.778	12.45		Work done by pump(kW)	0.01431
7	0.938	124.7		Refrigerant mas flow arte	0.8217
8	0.1162	167.2		Strong solution mass flow rate (kg/s)	6.6
9	0.8217	75.95		Weak solution mass flow rate (kg/s)	5.778
10	0.0008217	40		COP(thermal)	0.8965
11	0.0008217	24.18		COP (overall)	0.8852
12	0.8217	-24.97		Strong solution concentration	0.2868
13	0.8217	15		Weak solution concentration	0.1868
14	0.8217	36.5			

5.3Discussion

Results from the system simulation show how varying some parameters affect others and improves the system COP towards the optimum operating range at which the system is best to operate. Most parameters have an effect on the overall system but at different levels. The most sensitive parameters were the effectiveness of the solution heat exchanger, the pressures at the absorber and desorber, and the outlet temperatures of both the absorber and desorber. Increasing the solution heat exchanger (SHX) effectiveness transferred more heat from the weak solution returning from the rectifier to the strong solution going into the desorber thereby reducing the heat to be added at the desorber. This also reduced the heat to be rejected at the absorber as the returning weak solution enters the absorber with less heat.

An increase in SHX effectiveness increased both the thermal and the overall COP as this is the ratio of the cooling load to the supplied heat. A reduction in the heat added at the desorber would increase both COP but does not have any effect on the flow rate and temperatures at the condenser and evaporator. Results showed that the heat added at the desorber reduced from the base case of 1.771 to 1.041 kW thereby increasing the COP from 42 to 60%.

Absorber exit temperature reduction increased both overall and thermal COP but had a limit depending on the surrounding temperature, if the absorber is air cooled. If the absorber is air cooled, as in the case discussed here there should be a minimum of $10^{o}C$ difference for exchange of heat to take place between the cooling medium (air) and the absorber.

An increase in desorber/condenser pressure reduced the overall and thermal COP. On the other hand, increasing the absorber/evaporator pressure increased the COP. This effect on the COP was due to the ammonia concentration increase or reduction when the pressures were altered. However, there was a limit taking into consideration as the overall COP for a single step VARS

should not be greater than 1. If the absorber/evaporator pressure was increased up to 400 kPa the COP increases to 0.98 from 0.42 and the ammonia concentration in the strong solution increased from 23% to 44%. Beyond this pressure level, the COP was larger than 1 which is not theoretically feasible.

The mass flow rate of the strong solution is another important parameter in the system. An increase in the mass flow rate increased the cooling load at the evaporator but did not affect the COP. As the strong solution flow rate increased, the flow rate of the refrigerant at the desorber increases, thereby increasing the heat input.

Based on the limitations and band of operating the system, and after optimization, Table 5.7 shows the final parameters used for the simulation of the system.

Table 5.7 Optimised Parameters for the VAS for Air-conditioning.

Ammonia concentration difference	10%
Condenser and absorber rejection temperature	40^{o}C
Absorber/Evaporator pressure	1.4bar
Condenser/Desorber pressure	15bar
Effectiveness of SHX/RHX	86%
Pump efficiency	70%

Table 5.8 and 5.9 show a comparison of the system based on different loads for refrigeration and air-conditioning bearing in mind that the evaporator temperature was fixed as 15^{o}C for air-conditioning and -20^{o}C for refrigeration.

Table 5.8 Parameters for air-conditioning loads of 1, 5, 10 and 20 kW.

System Parameters	1 kW	5 kW	10 kW	20 kW
Cooling load	1.082	5.112	10.01	20.0
Desorber heat input	1.263	5.962	11.68	23.32
Condenser heat rejected	1.108	5.234	10.25	20.48
Rectifier heat rejected	0.385	1.802	3.529	7.048
Absorber heat rejected	0.8708	4.112	8.055	16.09
Pump work	0.01567	0.07402	0.145	0.2895
Strong solution mass flow rate(g/s)	7.2	34.0	66.6	133.0
Weak solution flow rate(g/s)	6.314	29.82	58.41	116.6
Refrigerant flow rate (g/s)	0.8859	4.183	8.194	16.36
Strong solution concentration (%)	27.72	27.72	27.72	27.72
Weak solution concentration (%)	17.72	17.72	17.72	17.72
Overall COP	0.8468	0.8468	0.8468	0.8468
Thermal COP	0.8573	0.8573	0.8573	0.8573

Table 5.9 Parameters for Refrigeration at 1, 5, 10 and 20kW

System Parameters	1 kW	5 kW	10 kW	20 kW
Cooling load	1.073	5.067	10.13	20.86
Desorber heat input	1.263	5.962	11.92	24.55
Condenser heat rejected	1.108	5.234	10.47	21.55
Rectifier heat rejected	0.3815	1.802	3.604	7.419
Absorber heat rejected	0.8612	4.067	8.134	16.75
Pump work	0.01567	0.07402	0.148	0.3048
Strong solution mass flow rate(g/s)	7.2	34	68	140
Weak solution flow rate(g/s)	6.314	29.82	59.63	122.8
Refrigerant flow rate (g/s)	0.8859	4.183	8.367	17.23
Strong solution concentration (%)	27.72	27.72	27.72	27.72
Weak solution concentration (%)	17.72	17.72	17.72	17.72
Overall COP	0.8314	0.8394	0.8394	0.8394
Thermal COP	0.8498	0.8498	0.8498	0.8498

From Tables 5.8 and 5.9, it can be seen that there is not much difference between the parameters for refrigeration and air-conditioning operation at each given cooling load. The difference is simply the evaporator exit temperature, which does not have a significant effect on the COP, heat input at the desorber, and the cooling load at each given or desired operating which can be seen in Figure 5.11a and b. It can be seen from Fig. 5.11a that the heat added at the generator

(desorber) for refrigeration and air-conditioning operation overlay one another showing that they have all the same quantity of heat for the desired evaporator load. More so, the heat rejected at the condenser and absorber are practically of the same quantity as seen from Fig. 5.11a because they are on same line path. As can also be seen by comparing Tables 5.8 and 5.9.

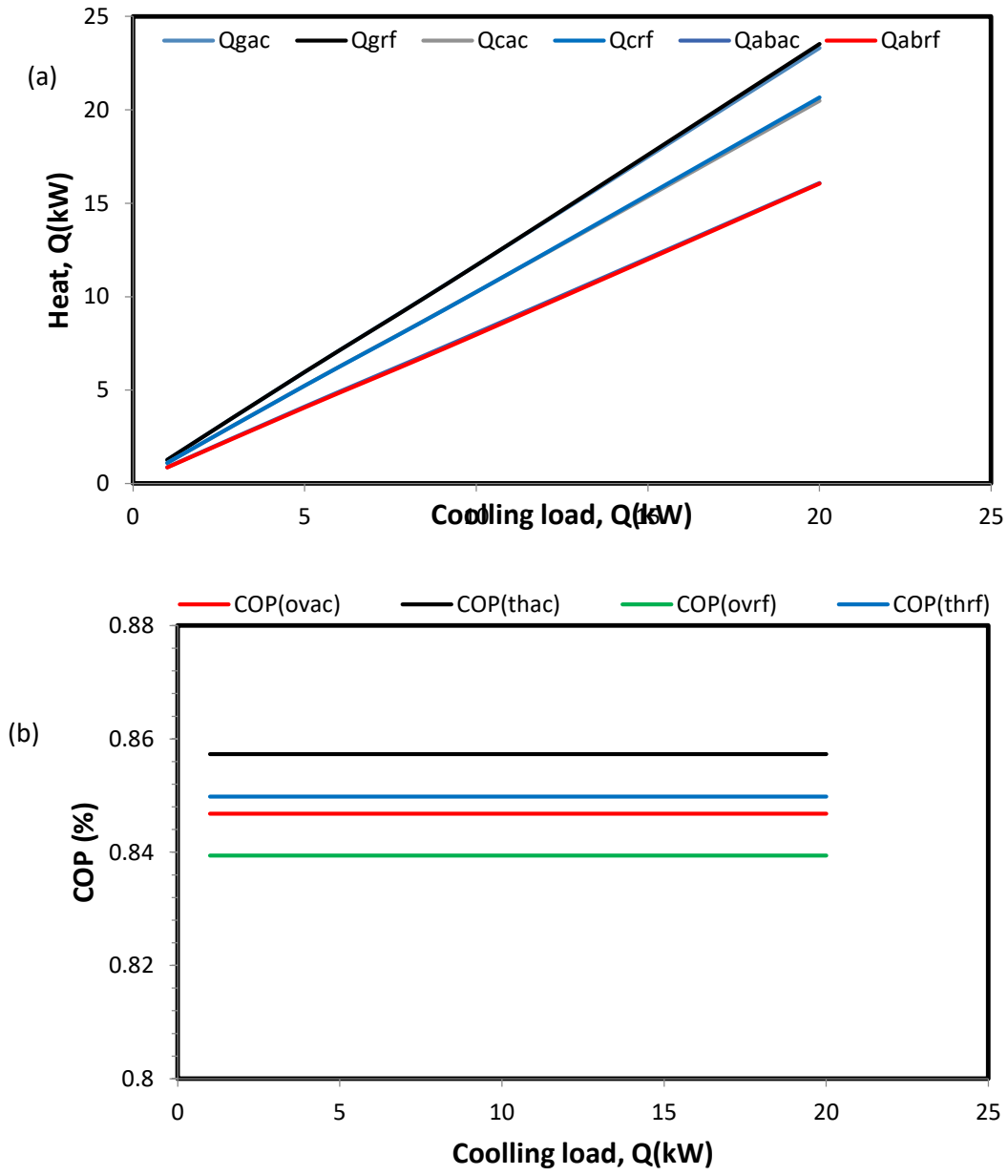

Figure 5.11Comparison of (a) heat added at desorber and rejected at condenser/absorber (b) thermal/overall COP for refrigeration and air-conditioning.

The overall and thermal coefficient of performance, for 1kW, 5kW, 10kW and 20kW cooling load for both refrigeration and air-conditioning remain constant as seen in Fig. 5.11b. The overall COP for air-conditioning was 0.8468 and that of refrigeration was 0.8394, while the thermal COP were 0.8573 and 0.8498, respectively, for air-conditioning and refrigeration operation. This shows that the COP (thermal and overall) is almost the same no matter the mode of operation at any desired evaporator load. Even the mass flow rates of the strong and weak solution, refrigerant flow rate at each desired cooling load do not differ much, as seen in Tables 5.8 and 5.9. This implies that the evaporator exit temperature, which determines the condition of refrigeration or air-conditioning, does not have an effect on the desired cooling load. This seems to be mainly determined by the mass flow rate, because the thermal energy generated is used to break the molecules during the phase change from liquid to vapour and only the entropy and enthalpy change. The change in enthalpy during this phase in both the modes of operation results in almost the same enthalpy difference (outlet enthalpy – inlet enthalpy) and since the flow rate of the refrigerant is the same; it results in the same evaporator load.

6 Chapter 6

EXPERIMENTAL RESULTS AND ANALYSIS

The foundation of the experimental pattern has been laid at Chapter 3 where step-by-step procedures have been set out towards achieving a successful experimental investigation. Based on this background, this chapter is dedicated to detail experimental analysis of the solid oxide fuel cell (SOFC) exhaust heat driven vapour absorption refrigeration system (VARS).

6.1 SOFC cathode exhaust heat recovery through double pipe heat exchanger

Fig. 6.1 shows a schematic of the heat recovery part with the double pipe heat exchanger and Table 6.1 showing the dimensions of the heat exchanger (DPHX). Detailed modelling of the DPHX had been carried out in Chapter 4 and, the various procedures to be followed for this part of the experiment have been presented in Chapter 3 (section 3.3.1) of this thesis. The sub-system evaluated here consist of the thermal oil storage tank, thermal oil pump, air blower, electric heater, and the internally finned double pipe heat exchanger.

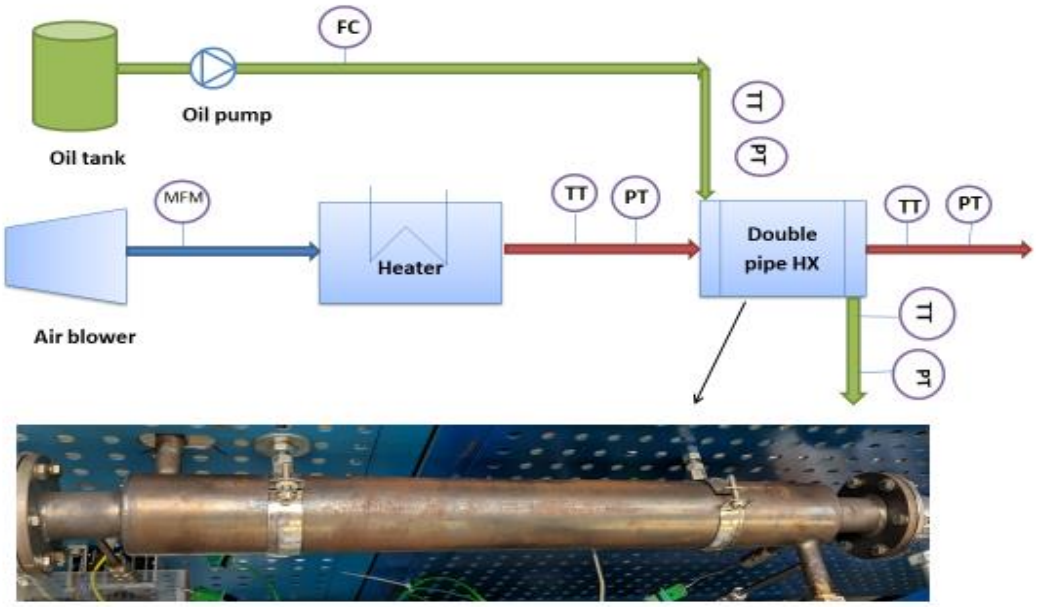

Figure 6.1Schematic of experimental test rig and installed DPHX pictorial view

(TT- temperature transmitter, PT- pressure transmitter, MFM – mass flow meter, FC- flow controller/meter)

Table 6.1 Geometrical details of double pipe heat exchanger [1]

Parameter	**Value**
Fin height (mm)	8
Fin thickness (mm)	4
Number of fins N	4
Length of finned tube L (mm)	500
Inner diameter of inner tube (mm)	30
Outer diameter of inner tube (mm)	34
Inner diameter of outer tube (mm)	56
Outer diameter of outer tube (mm)	62

6.1.1 Results and discussion

Figs. 6.2 and 6.3 are the experimental results of the effect of the cathode exhaust and thermal oil flow rates variation on the temperatures. The fuel cell cathode exhaust flow rate was varied between 30.19 g/s and 50 g/s while the oil flow rate was between 2 g/s and 16 g/s. These flow rates were arrived at after series of experiments were carried out to find the best operating range of the test rig: Operating the air blower below 30.19 g/s will result in the heater temperature going above 649 ^{0}C and will lead to damage of heating elements as recommended by the manufacturer. The maximum flow rate of the air blower was 55 g/s as per manufacturer's technical data, therefore a decision was made to operate the blower at maximum flow rate of 50 g/s allowing an allowance of 5 g/s. On the other hand, the oil pump maximum flow rate was limited to be 20 g/s through the LabVIEW control, hence operating it at maximum of 16 g/s to allow for 4 g/s allowance above which there was fluctuation in the oil pump flow which will lead to in-accurate data.

It can be seen from Fig. 6.2 that the cathode exhaust temperature was just above 600 ^{o}C when the variation was started at which point the inlet and outlet temperatures of the heat transfer oil were 106 and 260 ^{o}C respectively. The outlet temperature of the thermal oil after being heated up by the cathode exhaust heat in the DPHX stabilized at 186^{o}C while the inlet temperature was at 147 ^{0}C for the rest of the test at this steady state. This means that there was a temperature gain of 39 ^{0}C by the thermal oil in one pass as it flows through the DPHX. Furthermore, at this steady state, the inlet and outlet temperatures of the exhaust were 342 and 329.9 ^{o}C respectively, as seen in Fig 6.2.

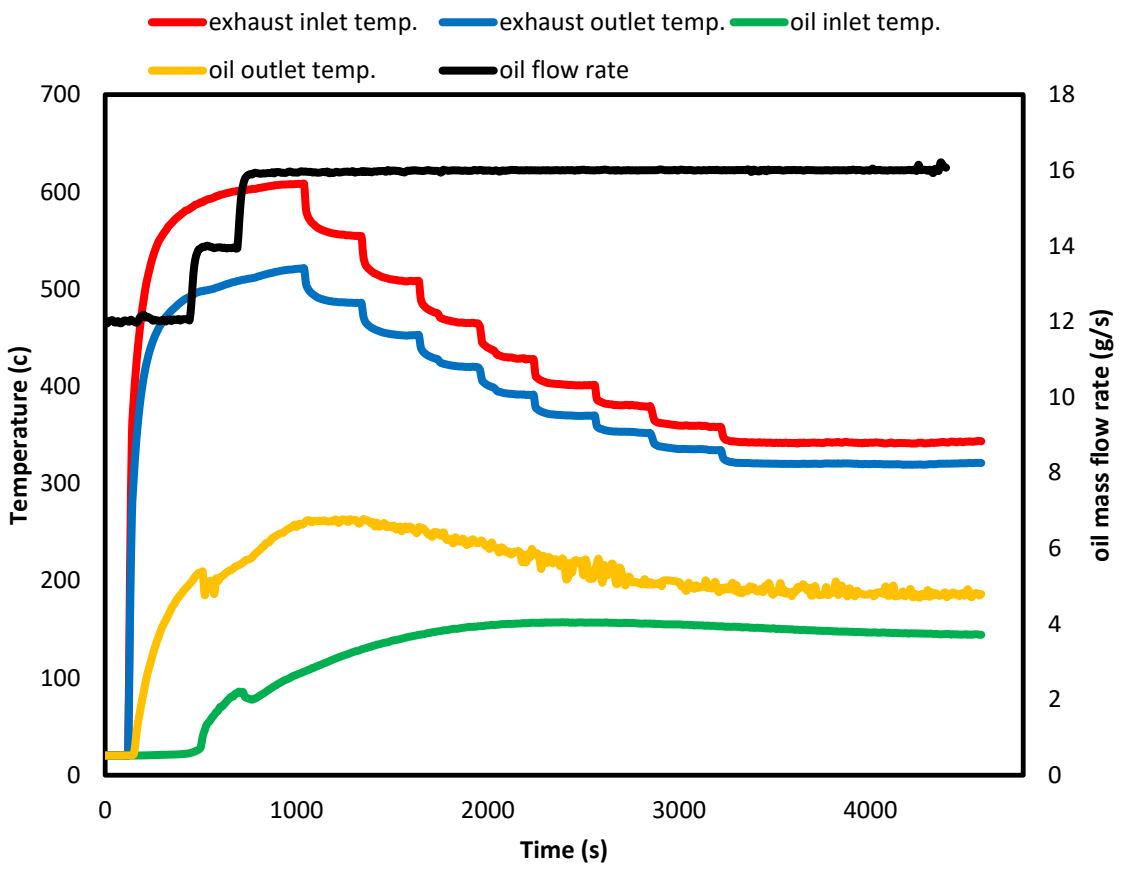

Figure 6.2 Effect of SOFC cathode exhaust flow variation on temperatures

Fig.6.3 shows the temperature profile when the oil flow rate was varied. At the steady state when the oil flow rate was 16 g/s with exhaust flow rate at 30.19 g/s, the exhaust inlet and outlet temperatures were 600 and 545 ^{o}C, respectively. On the other hand, the oil inlet and outlet temperatures were 112 and 203 ^{o}C. Figure 6.3 shows that at each step increase of the oil flow rate, the exit oil temperature reduced. This was because at increased oil flow rate with the exhaust flow rate kept constant at 30.19 g/s, the residence time of the oil in the DPHX reduced thereby reducing the heating up time leading to less heat transfer from exhaust to thermal oil.

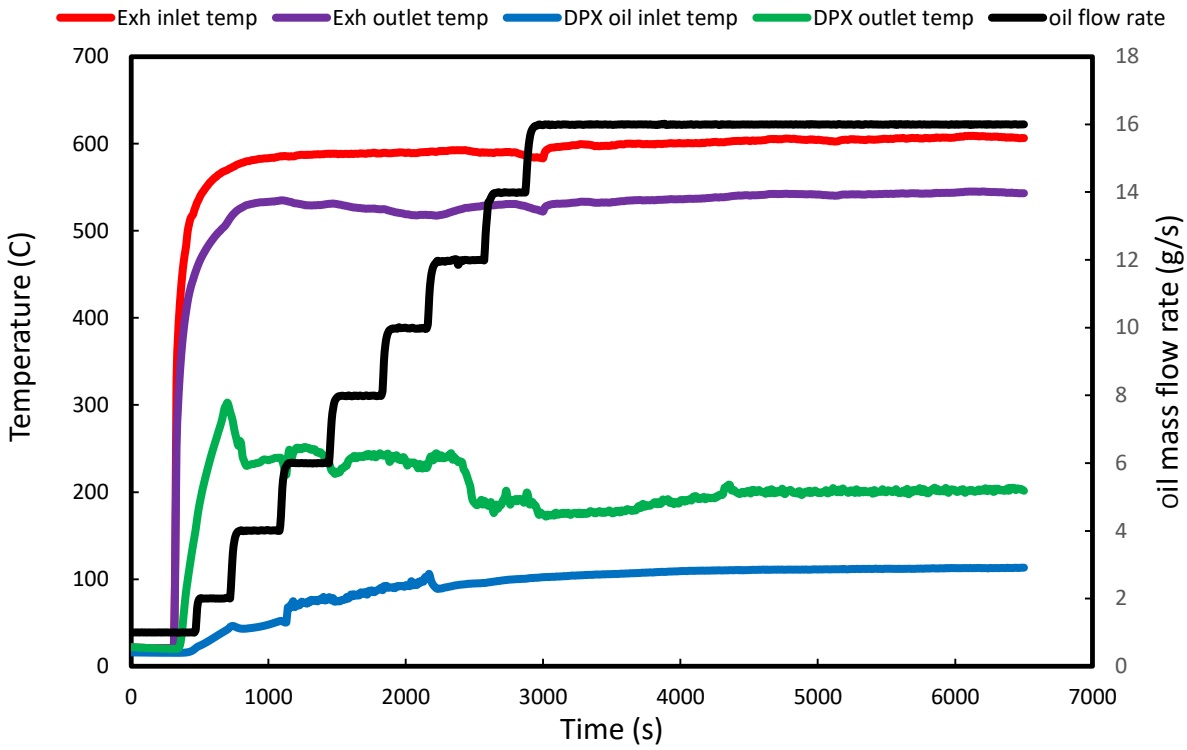

Figure 6.3 Effect of thermal oil flow rate variation on temperatures.

6.1.2 Determination of the heat transfer rate and heat exchanger effectiveness

Based on the experimental results as shown in Figs. 6.2 and 6.3, the heat transfer rate was determined using Eq. 6.1. This gave an insight into the available useful heat that was harnessed from the SOFC cathode exhaust which could serve as input heat at the desorber of vapour absorption refrigeration system to meet a desired evaporator load.

$$\dot{Q} = \dot{m}_o C_p (T_{oo} - T_{oi}) \qquad (6.1)$$

Where

$\dot{Q}$ *Heat transfer rate (kW)*

$\dot{m}_o$ *Mass flow of thermal oil (kg/s)*

C_p *Specific heat capacity of thermal oil (2.3 KJ/kg-K)*

T_{oi}, T_{oo} *Inlet and outlet temperature of thermal oil (^oC)*

An investigation into the impact the thermal oil flow rate variation had on the heat transfer rate was carried out. Figure 6.4 shows that an increase in the thermal oil flow rate with the cathode exhaust flow rate kept constant at 30.19 g/s, the heat transferred to the thermal oil reduced. This was due to less residence time in the DPHX of the thermal oil as explained earlier. It can be seen that there was a maximum heat transfer rate of 4.2 kW (at oil flow rate of 10 g/s) from 0.014 at the beginning of the experiment which steadied off at 3.2 kW at an oil flow rate of 16 g/s for the rest of the duration of the experiment. This can also be explained in the reduction of the temperature gained (from 260 ^{0}C to 88.2 ^{0}C) by the thermal oil in one pass as it flowed through the DPHX. This implied that 3.2 kW of heat was recovered from the fuel cell exhaust at exhaust and oil flow rates of 30.19 g/s and 16 g/s, respectively.

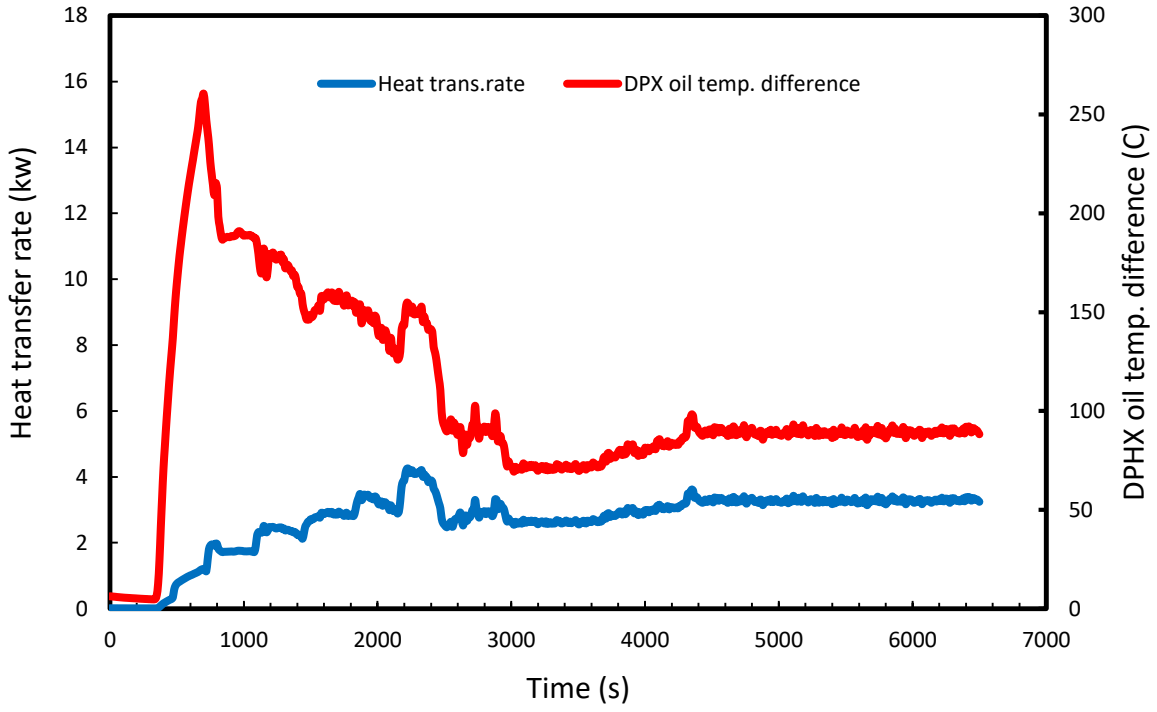

Figure 6.4 Amount of heat recovered from fuel cell exhaust by thermal oil.

Fig. 6.5 shows the temperature profile of the thermal oil when it exits the desorber and flows back into the thermal oil tank after transferring heat to the strong ammonia solution which will then be pumped back into the DPHX for the repeat of the cycle as this is a closed loop.

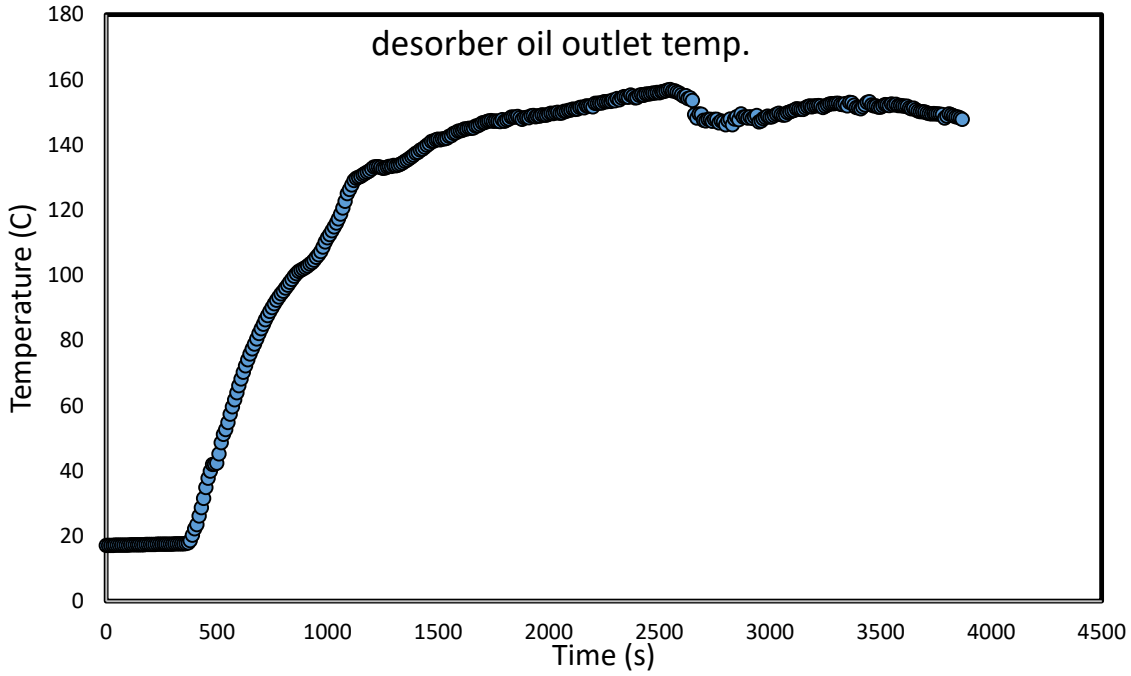

Figure 6.5 Thermal oil temperature at desorber outlet.

It can be seen that at a thermal oil flow rate of 16 g/s, the oil exits the desorber at a temperature of 150 ^{o}C. In essence, this is supposed to be the inlet oil temperature at the DPHX as compared to the one in Fig. 6.3 at 112 ^{o}C. This difference is seen because when the thermal oil returns back to the storage tank it enters at the top of the tank while it is pumped out through the bottom. This leaves the top part of the oil in the tank at higher temperature than the bottom. Therefore, using Eq. 1, the actual heat transfer rate was only 1.84 kW as against that in Fig. 6.4 at an oil flow rate of 16 g/s and cathode exhaust flow rate of 30.19 g/s.

On the other hand, the heat transfer rate during the cathode exhaust flow variation is shown in Fig. 6.6. There was a reduction in the heat transfer rate at every incremental step which steadied at 1.5 kW at an exhaust flow rate of 50 g/s. This reduction was due to less residence time of the cathode exhaust flow in the DPHX thereby reducing the time taken to heat the thermal oil.

More so, there was a decrease in the oil inlet temperature at increased exhaust flow rate as shown in Figure 6.2, leading to a reduction in the delta T (inlet and outlet temperature difference) of the exhaust and consequently reduced heat transfer rate.

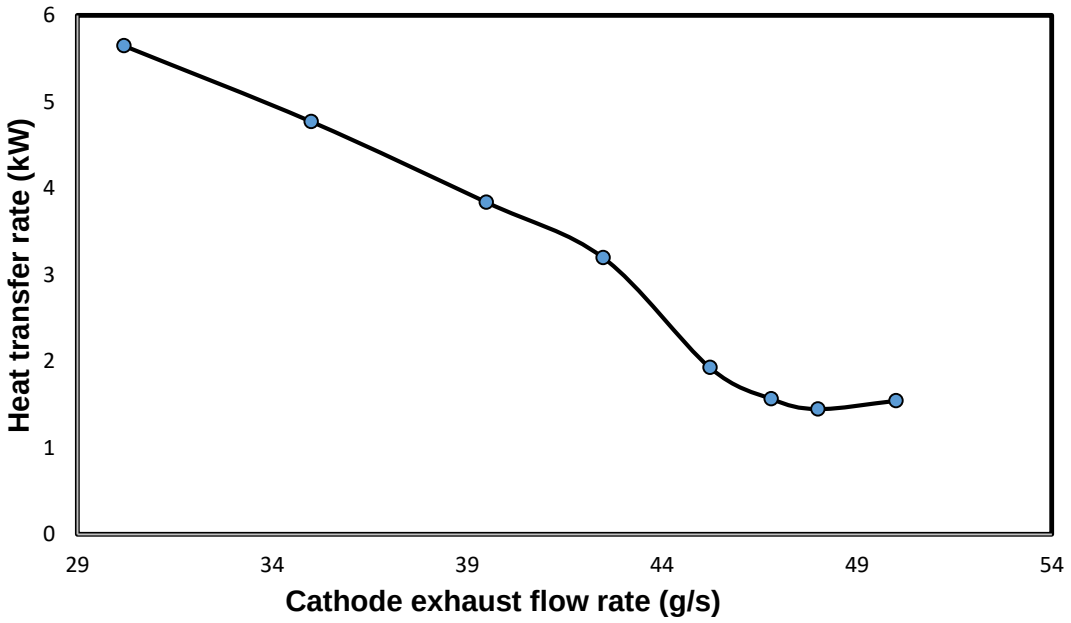

Figure 6.6 Effect of cathode exhaust flow rate variation on heat transfer rate.

The effectiveness of the DPHX was determined using Eq. 6.2

$$\mathcal{E} = \frac{heat\ transfered\ to\ oil}{maximum\ heat\ transferrable\ (q_{max})} \qquad \text{Eq. 6.3}$$

Table 6.2 shows a summary of the experimental results based on the foregoing analysis

Table 6.2 Experimental results of internally finned double pipe heat exchanger

Parameter	Value
Oil mass flow rate (kg/s)	0.016
Oil inlet temperature (K)	423
Oil outlet temperature (K)	473
Cathode exhaust flow rate (kg/s)	0.03019
Exhaust inlet temperature (K)	873
Exhaust outlet temperature (K)	818
Effectiveness (%)	12.22
Overall heat transfer (W/m^2-K)	60.15
Oil Heat gain (kW)	1.84
Temperature gained by oil (K)	50

6.2 Integration of the hot thermal oil with desorber and rectifier of the VARS

This section gives an experimental analysis of the performance of the desorber (plate heat exchanger) when the hot thermal oil and the strong ammonia-water solution flow through. It is worth noting that only the mass flow rates of the thermal oil and the strong ammonia-water solution can be controlled. These mass flow rates changes affect the inlet and outlet temperatures of the oil and the solution at the desorber. Before the strong solution enters the

desorber, it first passes through the rectifier where it gains heat from the ammonia vapour that flows into the condenser, causing partial condensation and increased temperature of the solution. In this manner, the rectifier works both as a vapour separator and solution heat exchanger. Figure 6.7 shows the piping and instrumentation diagram of the system while Figs. 6.8 and 6.9 are the rectifier and desorber temperatures profile respectively. Figure 6.8 shows that the strong solution leaving the solution tank was at a temperature of about 17 ^{0}C when it entered the rectifier and gradually increased to 116 ^{o}C at the outlet of the rectifier before entering the desorber. In this manner, the amount of heat to be added at the desorber by the thermal oil for desorption of ammonia to take place was drastically reduced.

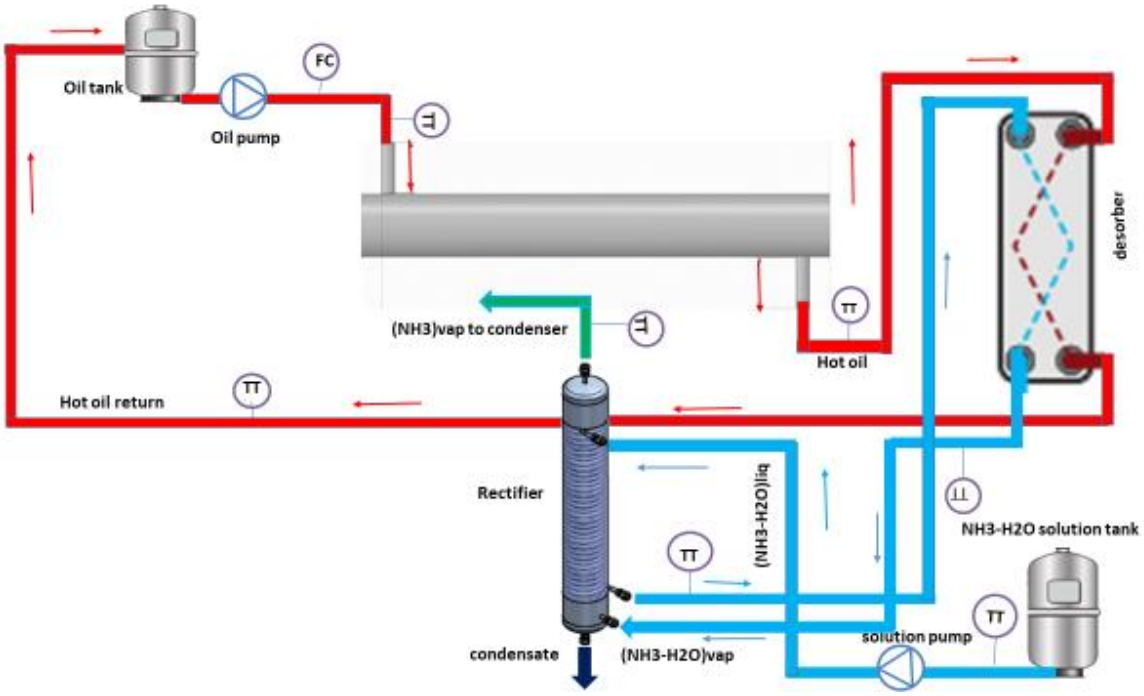

Figure 6.7 Schematic integration of thermal oil circuit, desorber and rectifier.

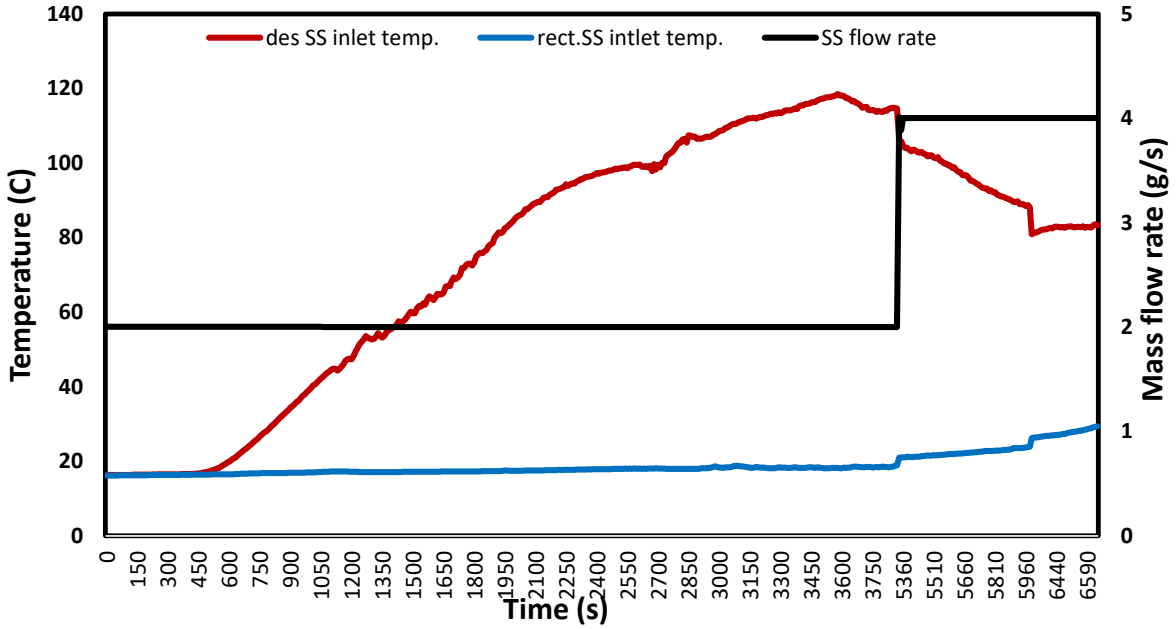

Figure 6.8 Strong solution temperature profile in rectifier.

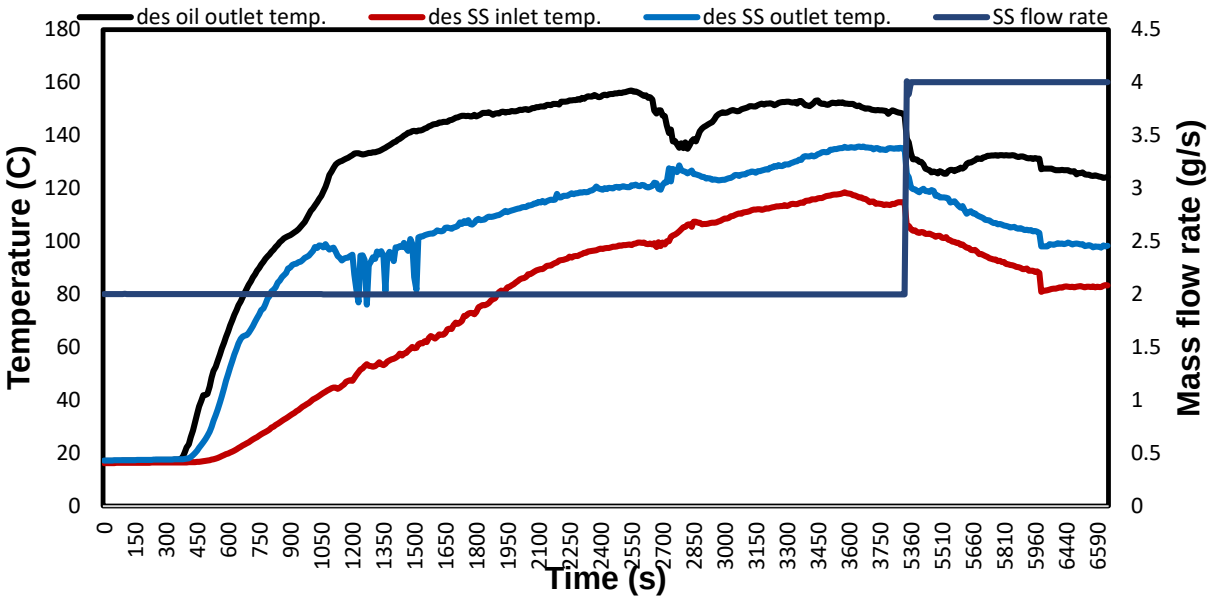

Figure 6.9 Temperature profile in desorber.

Figure 6.9 shows the temperature profile of the thermal oil at the exit of the desorber and the inlet and outlet temperatures of the strong ammonia-water solution. It can be seen that the thermal oil temperature exits the desorber at steady state of about 150 ^{0}C at oil and strong solution flow rates of 16 g/s and 2 g/s, respectively. When the strong solution flow rate was increased from 2 g/s to 4 g/s with the thermal oil kept constant at 16 g/s, the temperatures were seen to be reducing. This was due to the fact that the strong solution residence time in the desorber was reduced due to increased flow rate, thereby reducing the heat exchange between the thermal oil and the solution. This will mean that less or not enough ammonia desorption will take place which invariably will result in less cooling at the evaporator.

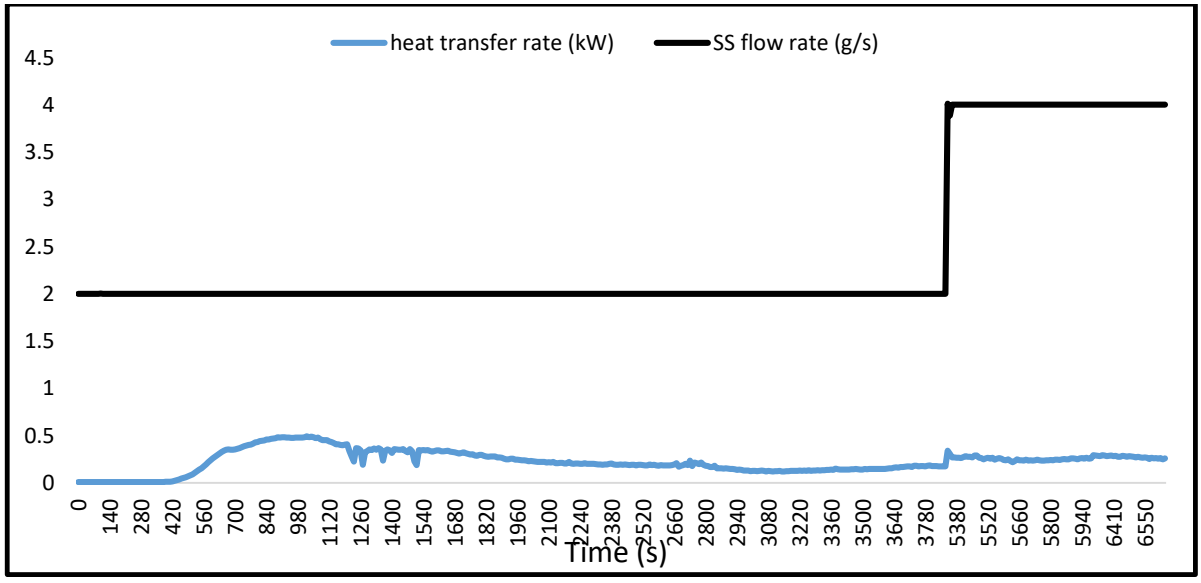

Figure 6.10 Heat transfer rate in the plate heat exchanger desorber.

Figure 6.10 shows the heat transfer rate in the desorber. There was a maximum value of 0.5 kW at an oil flow rate of 2 g/s which reduced to 0.3 kW until the oil flow rate was increased to

4 g/s. The low heat transfer rate was due to a low solution mass flow rate and low temperature gained from the thermal oil which was $\Delta = 19\ ^{o}C$ in one pass at the desorber. At an oil flow rate of 4 g/s, the heat transfer rate seems to increase a little even if the inlet and outlet temperatures of the ammonia-water strong solution reduced as seen in Fig. 6.9. This is because the heat transfer rate is a product of the mass flow rate, specific heat capacity and the temperature difference between the inlet and outlet of the desorber. The influence of the mass flow rate at this stage was higher than that of the temperature difference hence the increase in heat transfer rate. But it is worthy to note that this does not lead to increased desorption of the ammonia vapour from the solution as temperature is reduced hence, less vaporization resulted in less cooling at the evaporator. This means that a delicate balance needs to be struck between flow rates, (absolute) temperature levels and required cooling power.

6.3 Integration of condenser and evaporator of the VARS

After successfully integrating the desorber and rectifier with the thermal oil circuit and experimental analysis carried out, the condenser and evaporator were integrated to the rest of the VARS system. Figure 6.11 shows the piping and instrumentation diagram of the complete VARS after integrating the condenser and evaporator. There are two zones (high and low pressure) on the system. The high pressure zone consists of the desorber, rectifier, and condenser, while the low pressure zone is made up of the absorber and evaporator. The expansion valves, one each at the condenser and rectifier outlets are used to reduce the high pressure fluid to low pressure as it circulates through the circuit.

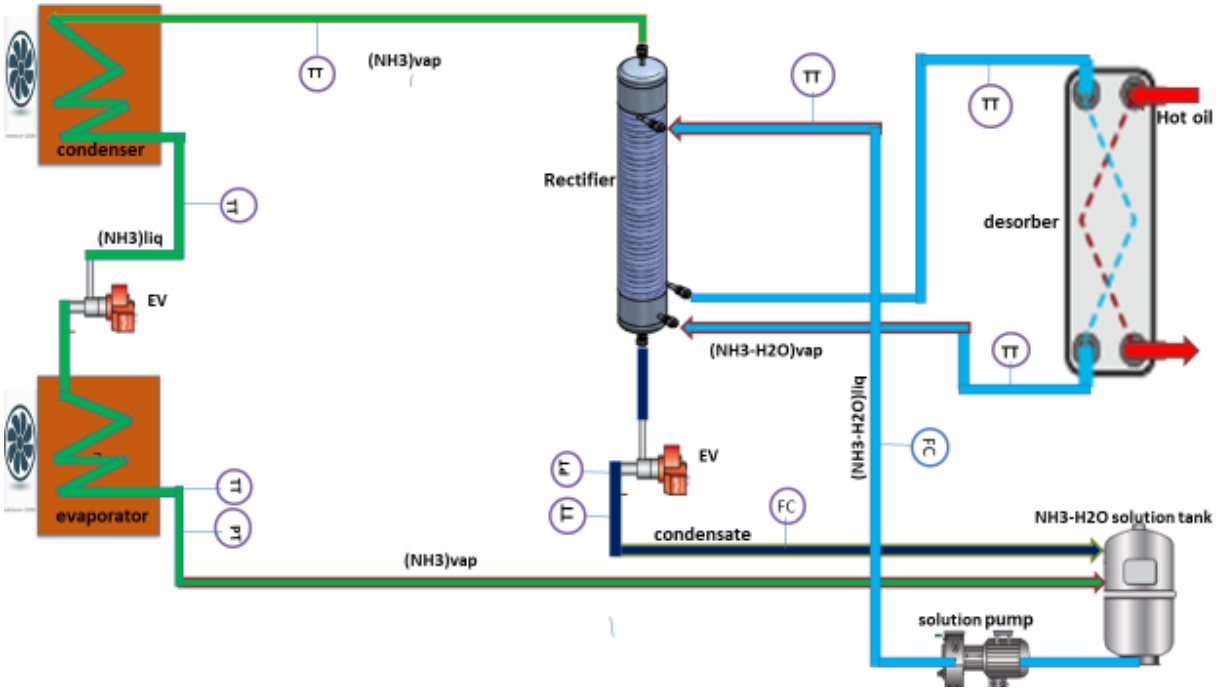

Figure 6.11 Complete VARS with integrated condenser and evaporator.

The pure ammonia vapour leaving the rectifier flowed into an air cooled condenser where it rejected heat to the surroundings thereby liquefying. The liquid ammonia flowed through an expansion valve where it further lost heat and pressure was reduced before entering the evaporator. The liquid ammonia absorbed heat from the refrigerated space via the evaporator and turned into vapour, causing the cooling effect. It then flowed back into the ammonia-water solution tank where it combined with the condensate from the rectifier to form the strong solution. This was then pumped back into the desorber for repeat of the cycle.

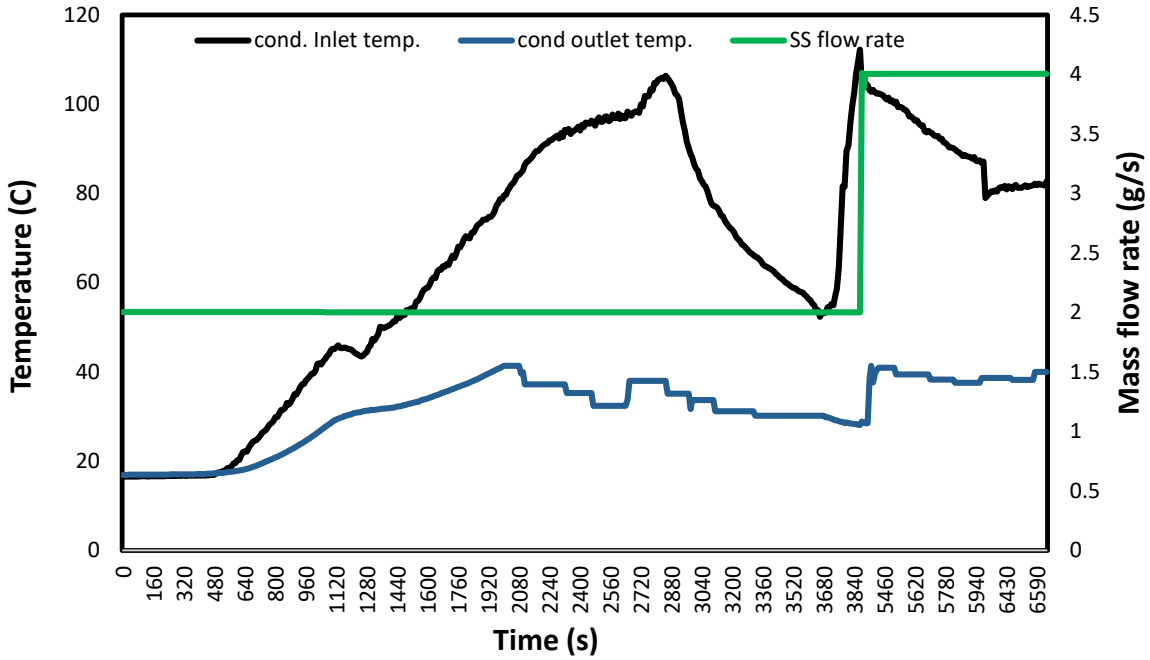

Figure 6.12 Refrigerant temperature profile in condenser.

With the fuel cell cathode exhaust, thermal oil, and strong ammonia-water solution flow rates at 30.19 g/s, 16 g/s and 2 g/s respectively, the temperature profile in the condenser was as shown in Fig. 6. 12. It can be seen that heat removal by the cooling fan on the condenser was effective. This is because the high inlet temperature of the ammonia vapour at the condenser was reduced to a reasonable value but not above 40 ^{0}C before it flowed through the expansion valve and into the evaporator. It can be seen that the inlet temperature increased until a point where it exhibited sharp reduction before increasing back to higher temperature. The sudden drop in temperature could be due to the cold solution flowing downward in the rectifier absorbing more heat in few seconds than earlier. The higher temperature did not last long but rather reduced when the strong solution flow rate was increased to 4 g/s.

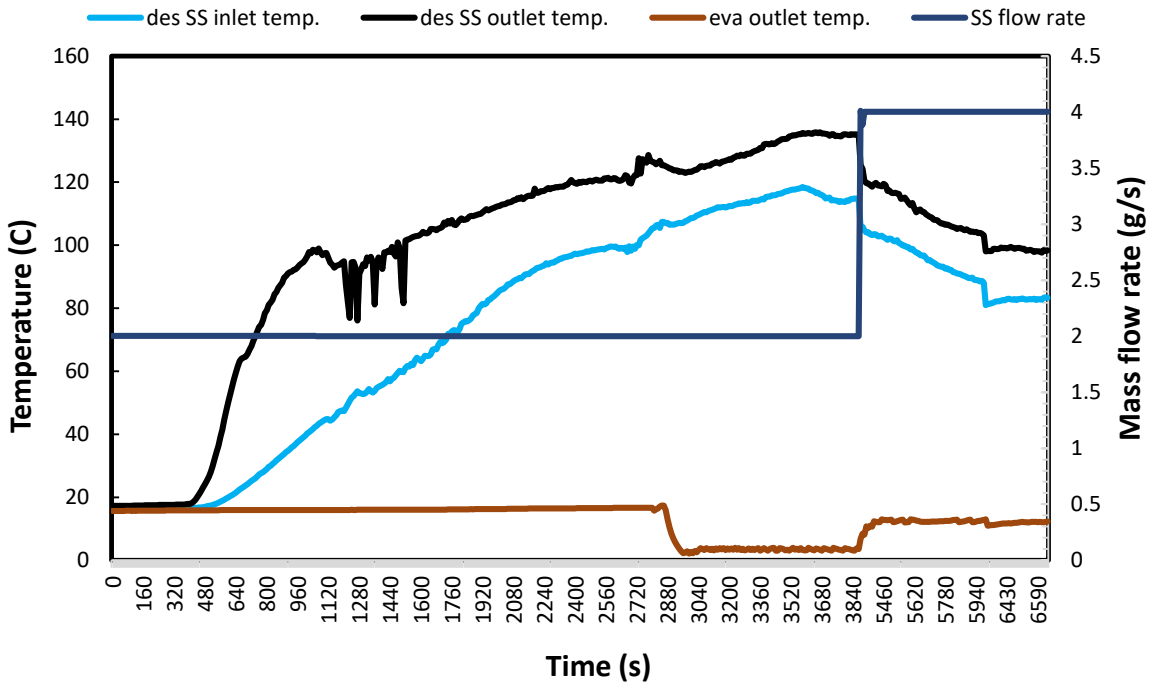

Figure 6.13 Temperature profile in desorber and evaporator.

Figure 6.13 shows the combined temperature profile in the desorber and evaporator with respect to the strong ammonia-water solution flow rate. It can be seen that, with the desorber inlet and outlet temperatures rising, the evaporator temperature was constant at about 17 ^{0}C until after 52 minutes it reduced to approximately 4 ^{0}C with the oil flow rate at 2 g/s. It was observed that the cooling started when the desorber exit temperature reached 120 ^{0}C and the lower pressure side was 3.5 bar. This reduced evaporator temperature was maintained until the solution flow rate was increased to 4 g/s when the evaporator temperature starts to increase. This is because at increased solution flow rate there is reduced residence time of the solution in the desorber leading to reduced heat exchange between the hot oil and the solution causing a reduction in the solution inlet and outlet temperatures as seen in Fig. 6. 13. This results in

less ammonia desorption from the solution due to a lack of heat, thereby causing reduced cooling at the evaporator.

6.4 Conclusions

The focus on this chapter was on the analysis of the experimental results to identify the cooling temperature achieved and the performance of the complete system. It started with the component test analysis, moving to the complete system performance tests. The following findings were made based on the experiment carried out:

i. Firstly, the coupling heat exchange was attached to the simulated fuel cell exhaust with a coupling heat transfer fluid to investigate the amount of heat that could be recovered. Results showed that a total of 1.84 kW of heat was recovered which represents a coupling heat exchanger effectiveness of 0.1222. This heat transfer rate was achieved at an exhaust and thermal oil flow rates of 30.19 g/s and 16 g/s, respectively. An increase in the exhaust and thermal oil flow rate led to a decrease in the heat transfer rate and vice-versa.

ii. The use of the rectifier as the solution heat exchanger and at the same time vapour separator improved the system compactness. Results show that the solution gained temperature of about 100 ^{0}C as it flowed through the rectifier before entering the desorber. This also led to the earlier explanation of the reduced heat transfer between the thermal oil and the solution in the desorber as it required only a little heat for ammonia desorption to take place.

iii. The experimental results also showed that a cooling effect was achieved after 52 minutes at the evaporator with temperature down to 4 ^{0}C. This result was at an oil and

solution flow rate of 16 g/s and 2 g/s. It was also observed that the cooling effect started at desorber temperature of 120^0C.

7 Chapter 7

MODEL VALIDATION WITH EXPERIMENTAL RESULTS

Having established the experimental setup, the final key section in this thesis will be the investigation into matching the modelling work from Chapters 4 and 5 with the experimental data in order to determine the accuracy of prediction of the output and performance of the various components of the VARS system. It is on this basis this chapter will bring together the modelling and experimental work done thus far.

7.1 Validation of the coupling heat exchanger

A detailed numerical modelling analysis of the internally finned coupling double heat exchanger was presented in Chapter 4, and the experimental results analysed in Chapter 6 were used to validate the model here. It was shown in Chapter 4 that there was a minimum thermal oil inlet temperature at every exhaust flow rate when the thermal oil flow rate and outlet temperature and exhaust inlet temperature were fixed. The effect of varying the exhaust and thermal oil flow rates were also analysed. Table 7.1 gives the heat exchanger performance from the model and experiment, while Figure 7.1 shows the comparison between the model output and experiment at varying cathode exhaust flow rates. The exhaust outlet temperature was fixed at 873 K, the thermal oil inlet and outlet temperatures, and mass flow rate were fixed at 423 K, 473 K, and 0.016 kg/s respectively. The exhaust flow rate was varied between 0.0057 and 0.06 kg/s based on these conditions.

Table 7.1 Comparison of the model and experimental values

Parameter	Model	Experiment	Difference
Oil flow rate (kg/s)	0.02	0.016	0.004 (20%)
Oil inlet temperature (K)	423	423	-
Oil outlet temperature (K)	473	473	-
Exhaust flow rate (kg/s)	0.038	0.03019	0.00781 (20.6%)
Exhaust inlet temperature (K)	873	873	-
Exhaust outlet temperature (K)	818.4	818	0.4 (0.049%)
Effectiveness (%)	12.14	12.22	0.02 (0.18%)
Overall heat transfer (W/m^2-K)	75.15	60.15	15 (19.96%)
Oil Heat gain (kW)	2.3	1.84	0.46 (20%)
Temperature gained by oil (K)	50	50	-

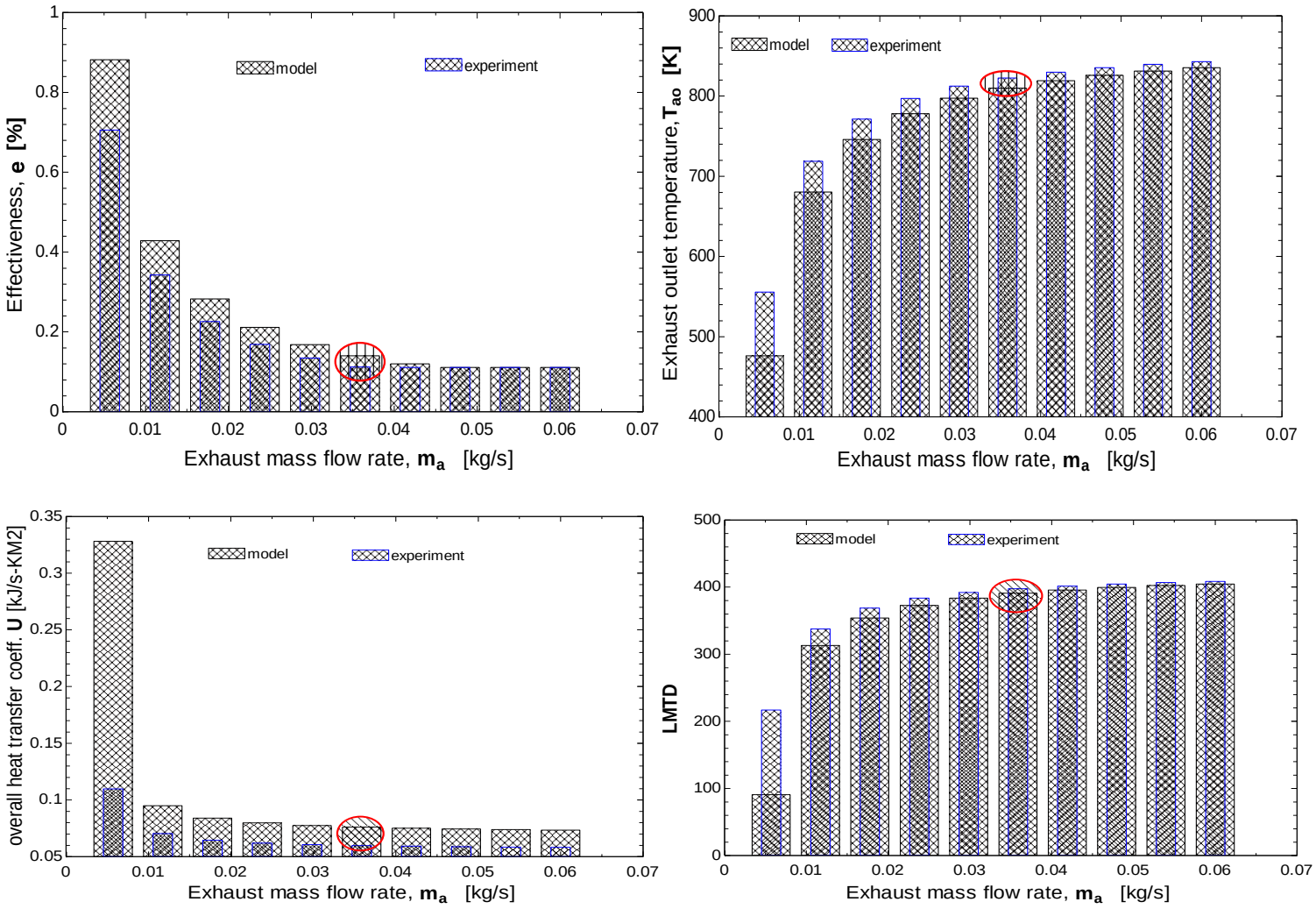

Figure 7.1Double pipe heat exchanger model and experimental results comparison

It can be seen in Figure 7.1 that, the model results offered close match to the experimental results and lies at the red circled area. There was some difference between the model and experiment in the exchanger effectiveness, exhaust outlet temperature, thermal oil heat gained, and overall heat transfer coefficient. This was due to a difference between the assumptions in the model and the actual experimental data for the thermal oil and cathode exhaust mass flow rates as shown in Table 7.1. In the model, the oil and exhaust flow rates were assumed to be 0.02 kg/s and 0.038 kg/s, while it was 0.016 kg/s and 0.03019 kg/s respectively from the experiment. It was also observed that, when the experimental values (thermal oil and exhaust flow rates) were used in the model to determine whether it predicted the experimental results when fed with the correct settings, which it did. The low heat exchanger effectiveness was due to the high exhaust mass flow rate of 0.03019 kg/s which represents a volume flow rate of 24.65 L/s. From this, it can be said that the presented model depicts and predicts the performance of the heat exchanger with sufficient accuracy.

It can also be observed from Figure 7.1 that, if a cathode exhaust flow rate of 0.0057 kg/s (4.653 L/s) were used, the heat gained by the thermal oil, overall heat transfer coefficient, and heat exchanger effectiveness would be 1.84 kW, 98.96 W/m^2-K, and 64.74 %, respectively. This implies that the same amount of heat would be recovered at a lower exhaust flow rate with higher heat exchanger effectiveness. Therefore, there will be 81.1 and 39.22 % improvement in the exchanger effectiveness and overall heat transfer coefficient respectively. More so, at an exhaust flow rate of 0.00453 kg/s (3.698 L/s) at the same experimental conditions gave 81.46% and 148.4 W/m^2-K respectively for the effectiveness and overall heat transfer. This shows effectiveness and overall heat transfer improvement of 85 and 59.5 % respectively and still recovered the same 1.84 kW of heat. However, the lower exhaust flow rates were not used on

the test rig due to limitations in operating conditions of the electric heater employed for the experiment as explained in section 6.1.1.

It was shown in Chapter 5 that, at COP of 0.7 the heat required at the desorber of a single effect VARS to achieve a 1 kW cooling load at refrigeration temperature of -20 ^{0}C was 1.43 kW. Therefore, the heat recovered from the heat exchanger in the experimental setup was definitely sufficient to meet the 1 kW cooling load demand of a small refrigerated truck. The experimental cathode exhaust flow rate of 0.03019 kg/s (24.65 L/s) represents a 5 kWe SOFC stack exhaust flow rate, while 0.00453 kg/s (3.698 L/s), and 0.0057 kg/s (4.653 L/s) both represent a 1 kW SOFC stack. Therefore, a 5 kWe SOFC when employed on a small refrigerated truck at exhaust flow rate of 24.65 L/s will meet a 1 kW cooling/refrigeration load with the coupling heat exchanger recovering 1.84 kW heat. Hence, from the aforementioned analysis, it would rather be ideal to use 1 kW SOFC on board the small refrigerated truck which will still deliver same amount of heat to meet the same refrigeration load at reduced exhaust flow rate. A 5 kW SOFC on small truck will lead to oversized system, increased volume footprint, and increased capital due to higher cost.

7.2Validation of the vapour absorption refrigeration system model

This section is dedicated to the validation of the vapour absorption refrigeration system with the experimental results as presented in Chapter 6. In both the model and experiment, the inlet and outlet temperatures were used to validate each component in the model. The experimental values as presented in Table 7.3 are averages across the range of temperatures within which the cooling effect took place at the evaporator, as shown in Figure 7.2. The evaporator inlet

temperature could not be determined from the experiment as there was no temperature sensor installed on the test rig on the low pressure outlet of the expansion valve.

Table 7.2 Comparison of the VARS model and experimental results

Model values					
Parameter	Absorber	Generator	Rectifier	Condenser	Evaporator
Inlet temperature (K)	311.24	408.2	410.9	348.95	239.62
Outlet temperature (K)	313	410.9	348.95	313	277
Experimental values					
Inlet temperature (K)	310	384	402.5	347	239.63
Outlet temperature (K)	293	402.5	347	307	277
Validation					
Inlet temperature (K)	300.48	387.1	396.6	348.95	239.63
Outlet temperature (K)	293	386.6	348.95	307	277

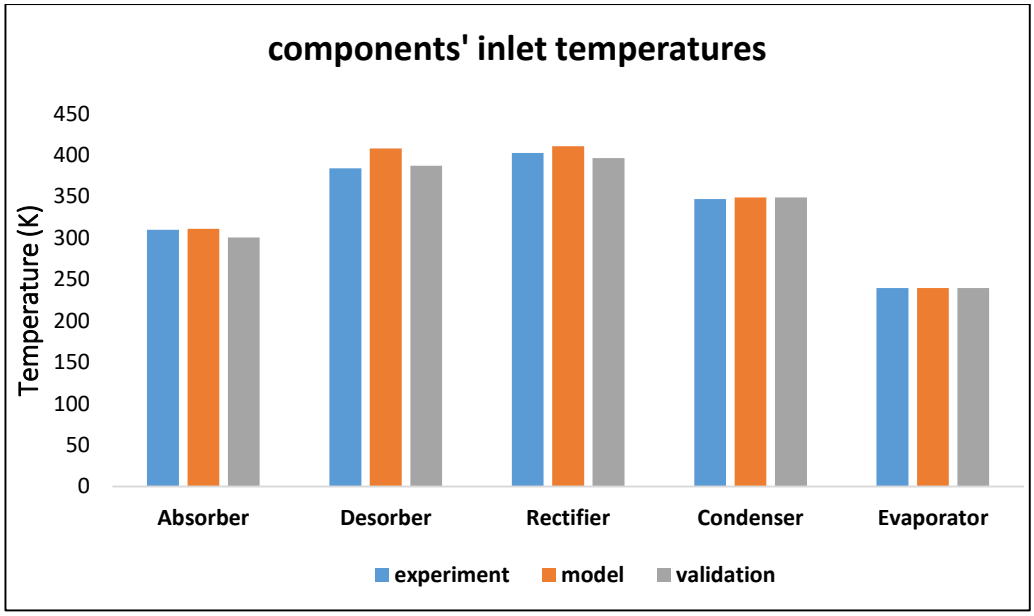

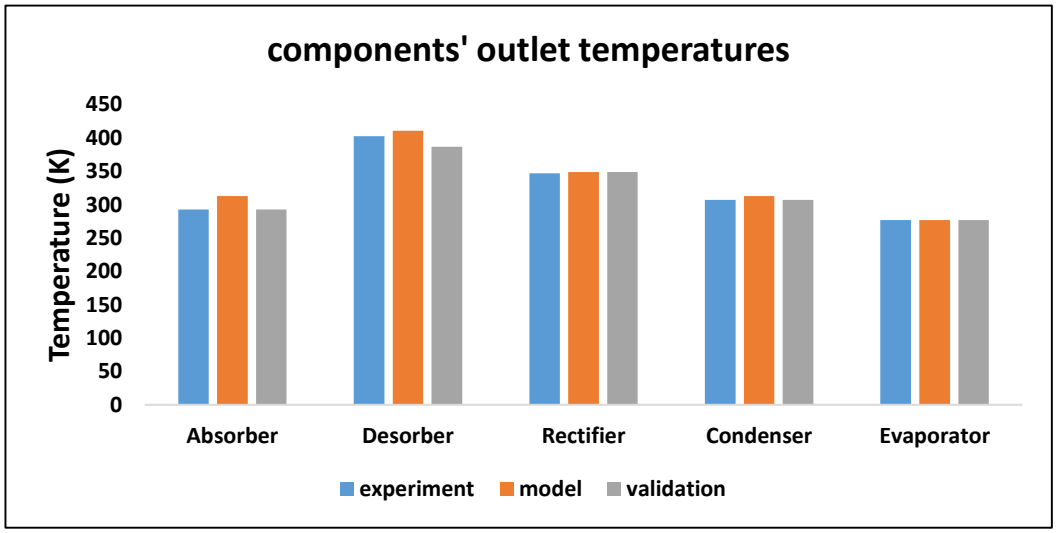

Figure 7.2 Graphical comparison of VARS model and experimental results

It can be seen from Figure 7.2 that the absorber inlet temperature was in good agreement between the model and experiment with a difference of just 0.4 %, while it was a 3.5% between the model and validated result. Validation or validated value/result here means when the experimental values are used as input values in the model to find out if the model predicts

accurately the experimental values. The model outlet temperature differed with that of the experiment and validated result with 6.8 %. At the desorber, the difference in the inlet temperature between the model and experimental value was 6.3 %, while it was 5.5 % between the model and validated value. The outlet temperature difference at the desorber between the model and experiment was 2.1 %, and it was 6.3 % difference between the model and validated value. There was 2.1% inlet temperature difference between the model and experiment at the rectifier, and 3.6 % between the model and validated value. On the other hand, the rectifier's outlet temperature was 0.6 % difference between the model and experimental value but there was no difference between the model and validated value.

There was no observed difference in the condenser inlet temperature between the model and validated result, while a 0.56 % was observed between the model and experimental value. A 2% outlet temperature difference was observed between the model and experiment, and likewise between the model and validated result. The outlet temperature was the same for the model, experiment, and validated value but a 0.005 % inlet temperature difference was observed both between the model and experiment, and model and validated result.

From the ongoing, it can be seen that the percentage difference was between 0.005 and 6.8 % with the maximum at the absorber outlet temperature which can be considered as an acceptable range.

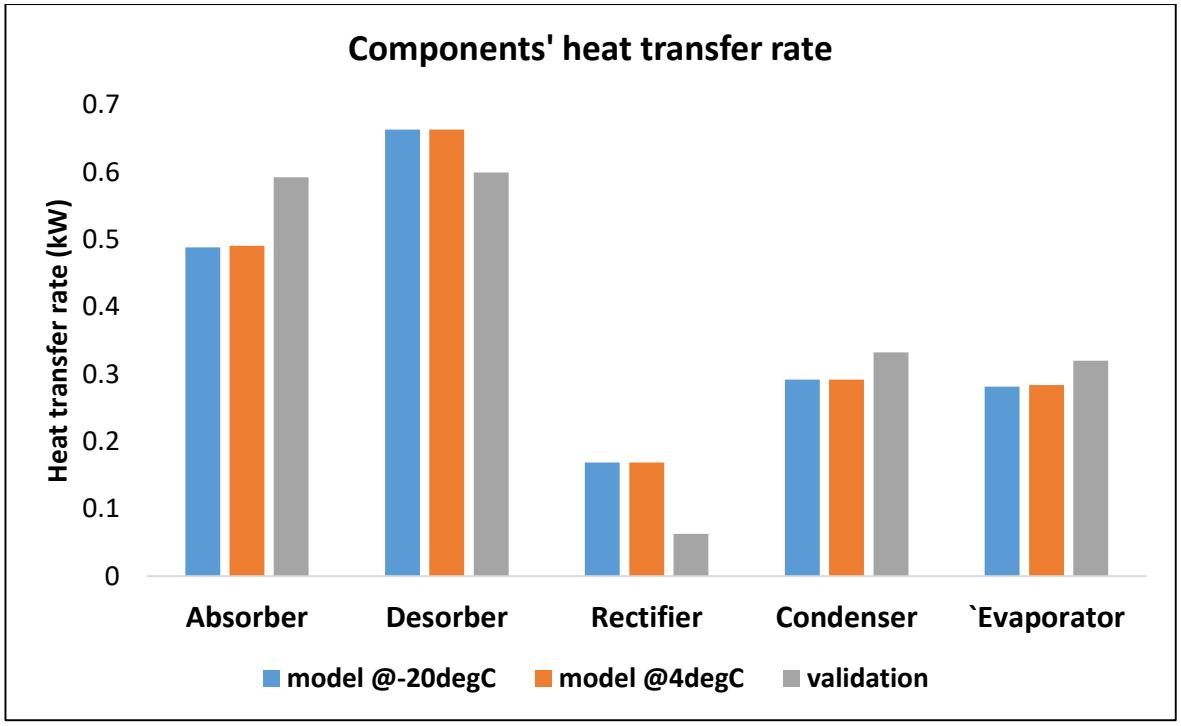

Figure 7.3 VARS heat exchangers heat transfer comparison

It is pertinent to point out here that the model was built to provide cooling at -20^{o}C (253K) but only 4^{o}C (277K) was achieved in the experiment which was due to low solution flow rate leading to low ammonia vapour desorption. The heat transfer at the main exchangers in the VARS at -20 ^{o}C and 4^{0}C refrigeration temperatures actually do not differ as seen in Figure 7.3. This is because the evaporator exit temperature do not have any significant effect on the components heat transfer as explained in Chapter 5. It can also be observed in Figure 7.3 that the heat rejected at the absorber, rectifier, and condenser were 0.4907, 0.1689, and 0.292 kW respectively for the model, while it was 0.5926, 0.0626, and 0.3321 kW respectively after validation. On the other hand, the heat input at the desorber and evaporator were 0.6633 and 0.2838 kW respectively for the model, while it was 0.5997 and 0.32 after validation. Validation here means, when the experimental values are implemented in the model. The error between

the model and validated results in terms of percentage were 17.2, 10.6, 62.9, 12.1, and 11.3 % respectively for the absorber, desorber, rectifier, condenser, evaporator respectively. These errors were due to the difference in the experiment and model value majorly at the absorber exit temperature (20 and 40^{o}C respectively). This is because a reduction in the absorber exit temperature increases ammonia solubility leading to higher strong ammonia-water solution concentration. The increased concentration means that more ammonia will be evaporated at the desorber leading to increased ammonia vapour mass flow rate at rectifier inlet and rectifier outlet to condenser as seen in Figure 7.4, while a reduction in the condensate (weak solution) mass flow rate leaving the rectifier is observed. These mass flow rates combination lead to a reduction in the rectifier heat rejected as seen in Eq. 7.1.

$$\dot{Q}_{rec} = \frac{\dot{m}_7 h_7}{\dot{m}_8 h_8 + \dot{m}_9 h_9} \qquad \text{Eq. 7.1}$$

Where the numbers 7, 8, and 9 are state points representing rectifier inlet, weak solution, and rectifier outlet to condenser respectively (explained earlier in Chapter 5). As seen in Figure 7.4 rate of increase of mass flow rate at point 9 is higher than that at state point 7 resulting in the denominator in Eq. 7.1 increasing higher that the numerator. This phenomenon will lead to a reduction in the rectifier heat transfer as seen in Figure 7.4 in the area covered by the red dotted triangle representing absorber exit temperature at 20 and 40^{o}C respectively. This explains the 62.9% difference between the model and experiment observed in Figure 7.3.

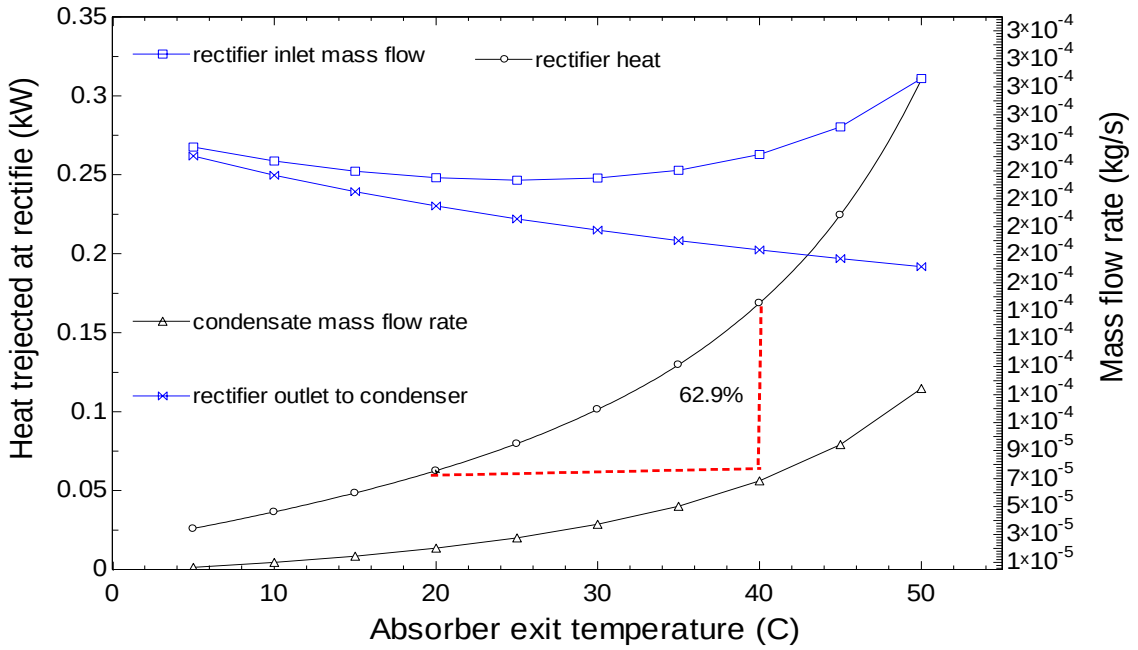

Figure 7.4 Effect of absorber exit temperature on rectifier heat transfer

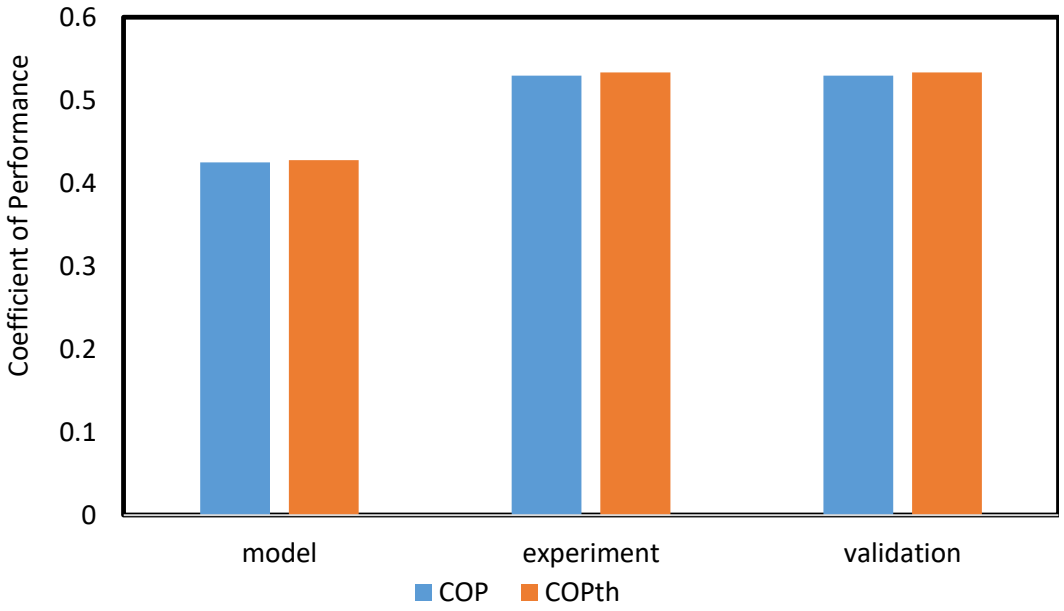

Figure 7.5 COP comparison between model, experiment, and validated results

The overall and thermal coefficients of performance (COP) of the VARS for the model, experiment, and validated results are shown in Figure 7.5. It was observed that the experimental and validated results were the same while there was a 19.7 and 19.8% difference respectively for overall and thermal COP between the model and experiment and validated results. This difference is due to the absorber exit temperature been 20^{o}C for the experiment as against 40^{o}C for the model. Ammonia solubility increases with reduced absorber exit temperature as explained in the previous paragraph thereby increasing the concentration of the solution in the absorber.

The increased ammonia concentration means that there is more ammonia to be desorbed at the desorber thereby increasing the refrigerant mass flow rate at the evaporator, hence the higher COP as illustrated in Figure 5.3a in Chapter 5. It is important to point out here that the lower absorber exit temperature was due to the fact the weak ammonia-water solution (condensate) returning to the absorber from the rectifier was water cooled as against the air cooled one in the model. This was due to the fact the air cooled patter was not too effective as the temperature in the absorber kept increasing above 60^{o}C which would reduce the ammonia concentration. Therefore, water cooled system was later employed which was more effective and resulted in a reduced absorber exit temperature

7.3 Conclusion

The modelling work carried out in Chapters 4 and 5 was validated in Chapter 7 with the experimental results obtained in Chapter 6. Based on the component level modelling of the coupling double heat exchanger, and system level modelling of the VARS, a close match was found between the values of the models and those of the experiments. The differences could

be improved if the flow regime in the test bench heat exchangers were changed from co-flow to counter flow and lower evaporator temperatures could be achieved at higher solution flow rates.

At this point it needs to be mentioned that the modification to counter-flow configuration had been prepared on the test bench. Unfortunately, it did not initially work to expectation because the solution pump developed issues and did not deliver the required higher flow. This could not be resolved anymore due to the university shutting down as a result of COVID-19 related decisions. Seeing the promising results from modelling and experiments, it could be reasonably expected that the modified test rig would have met the expectations.

8 Chapter 8

CONCLUSION AND SCOPE FOR FUTURE WORK

A practical investigation into the integration of a solid oxide fuel cell (SOFC) cathode exhaust and vapour absorption refrigeration system for refrigerated truck application was carried out in this thesis. It was based on various modelling work carried out in Chapters 4 and 5 of this thesis coupled with that reported in [149]. The use of SOFC exhaust heat to drive a thermally powered VARS for refrigerated trucks will reduce the electrical load placed on the main vehicle engine as is the case for most conventional systems. Besides, the electricity generated by the fuel cell can be used to power auxiliary loads on the vehicle.

Based on the experimental results in the previous chapters, it is evident that the practical integration of the SOFC and VARS was feasible and successful. The SOFC cathode exhaust temperature was 600 ^{0}C and above while that required at the desorber of the VARS was about 200 ^{0}C. Hence, an internally finned double pipe heat exchanger (DPHX) with a coupling fluid was employed to couple these two units of different temperatures. The experimental results and validation analysis presented in Chapters 6 and 7 showed that the simulated SOFC cathode exhaust mimics a real 5 kW_e stack size. The coupling DPHX was able to recover 1.84 kW of the thermal energy. It was also shown from the modelling work in Chapters 4 and 5 that the 1.84 kW thermal energy when delivered at the desorber of the VARS was able to cater to a cooling load of 1 kW. This amount of cooling load was sufficient for a small refrigerated van. It was also shown that the same amount of heat would be recovered to meet the same cooling load employing a 1 kWe SOFC. The model precision was in good agreement with the experimental results.

Furthermore, an evaporator temperature of 4^{o}C was achieved when the recovered fuel cell exhaust heat was integrated with the VARS. The novelty in this study is the successful integration of the simulated SOFC exhaust with the VARS experimentally in a laboratory setting.

8.1 Outcome of the experimental work

This section gives an overview of the findings based on the experimental work carried out in the previous chapters.

i. The experimental results mimics an SOFC stack size of 5 kW_e with the test rig able to simulate up to 10 kWe stack.

ii. The amount of thermal energy recovered by the DPHX was 1.84 kW at exhaust gas and thermal oil flow rates of 24.65 L/s and 16 g/s, respectively. The overall heat transfer coefficient and effectiveness of the DPHX were 60.15 W/m^2-K and 12.22% respectively. The inlet and outlet temperatures of the cathode exhaust and thermal oil at the DPHX were 873 and 818 ^{o}K, for the exhaust and 473 and 423 ^{o}K, for the thermal oil, respectively. It was also shown that the DPHX can be improved by about 81% if the exhaust flow rate is reduced to 4.653 L/s.

iii. The strong solution mass flow rate was 2 g/s at which an evaporator temperature of 4^{o}C was achieved at the vapour absorption refrigeration system.

iv. An evaporator temperature of 4^{o}C was achieved at the VARS with a COP of about 0.52

v. It was also discovered that only 0.5 kW of the recovered 1.84 kW heat was transferred to the VARS while losing the rest within the desorber.

8.2 Scope for future work

The work carried out here, if implemented on a real refrigerated truck with the SOFC stack and VARS, will be an interesting project and a world-first. This is because all the components of the VARS and accompanying accessories are available as they were used for the laboratory test. The following are aspects of future work to be carried out to add credence to the laboratory work reported here, and to the scarce practical work available in the public domain. To this date, fuel cells have only been used as an auxiliary power unit (APU) on-board refrigerated trucks. Tasks to be accomplished include

i. Integrate all components of the VARS into a system and acquire a 1 kW SOFC to integrate both systems on a truck. Use a 12 kg cylinder as hydrogen storage on board for the truck.
ii. Start the complete system as laid down in the previous chapters on-board the truck to achieve cooling. Depending on the amount of cooling archived fill the refrigerated cabin with some fresh foods that require chilled temperatures. Drive round campus to give free fruits and ice cream and study the performance of the system.
iii. Make some adjustment and modifications if necessary, and partner a refrigeration/logistics company to trial the demonstrator. Record data and study the performance of the system.
iv. Carry out an economic and technical analysis of the complete system and compare with other sources of refrigeration transportation system.

List of references

[1] Beddington, “Food, Energy, Water and Climate Change – A Perfect Storm of Global Events?”

[2] Defra, *Food Statistics Pocketbook 2013*. 2013.

[3] S. K. . Mei, V. C.; Lavan, Z.; Chaturvedi, “Highway Vehicle Exhaust Gas Refrigeration System. United States Patent 4341088,” *Geothermics*, vol. 14, no. 4, pp. 595–599, 1985, doi: 10.1016/0375-6505(85)90011-2.

[4] J. Koehler, W. J. Tegethoff, D. Westphalen, and M. Sonnekalb, “Absorption refrigeration system for mobile applications utilizing exhaust gases,” *Heat Mass Transf.*, vol. 32, pp. 333–340, 1997, doi: 10.1007/s002310050130.

[5] V. Venkataraman, A. W. Pacek, and R. Steinberger-Wilckens, “Coupling of a Solid Oxide Fuel Cell Auxiliary Power Unit with a Vapour Absorption Refrigeration System for Refrigerated Truck Application,” *Fuel Cells*, vol. 16, no. 3, pp. 273–293, 2016, doi: 10.1002/fuce.201500124.

[6] M. I. S. Adjibade, A. Thiam, C. Awanto, and D. Azilinon, “Experimental analysis of diffusion absorption refrigerator driven by electrical heater and engine exhaust gas,” *Case Stud. Therm. Eng.*, vol. 10, no. July, pp. 255–261, 2017, doi: 10.1016/j.csite.2017.07.004.

[7] A. Azapagic *et al.*, “Energy demand and reduction opportunities in the UK food chain,” *Proc. ICE - Energy*, vol. 167, no. 3, pp. 162–170, 2014, doi: 10.1680/ener.14.00014.

[8] S. J. James and C. James, “The food cold-chain and climate change,” *Food Res. Int.*, vol. 43, no. 7, pp. 1944–1956, 2010, doi: 10.1016/j.foodres.2010.02.001.

[9] O. Adekomaya, T. Jamiru, R. Sadiku, and Z. Huan, “Sustaining the shelf life of fresh food in cold chain - A burden on the environment,” *Alexandria Eng. J.*, vol. 55, no. 2, pp. 1359–1365, 2016, doi: 10.1016/j.aej.2016.03.024.

[10] P. Glouannec, B. Michel, G. Delamarre, and Y. Grohens, “Experimental and numerical study of heat transfer across insulation wall of a refrigerated integral panel van,” *Appl. Therm. Eng.*, vol. 73, no. 1, pp. 196–204, 2014, doi: 10.1016/j.applthermaleng.2014.07.044.

[11] Phys.org., “Refrigerated trucks to keep their cool thanks to fuel cell technology,” [Online]. Available: http://phys.org/news/2013-08-refrigerated-trucks-cool-fuel-cell.html.

[12] M. van der Tuin, “Time-dependent earliest arrival routes with drivers legislation and preferences,” Master thesis, Delft University of Technology, 2017.

[13] J. Deng, R. Z. Wang, and G. Y. Han, “A review of thermally activated cooling technologies for combined cooling, heating and power systems,” *Prog. Energy Combust. Sci.*, vol. 37, no. 2, pp. 172–203, 2011, doi: 10.1016/j.pecs.2010.05.003.

[14] J. Sun, L. Fu, and S. Zhang, “A review of working fluids of absorption cycles,” *Renew. Sustain. Energy Rev.*, vol. 16, no. 4, pp. 1899–1906, May 2012, doi: 10.1016/j.rser.2012.01.011.

[15] Z. X. Wang, S. Du, L. W. Wang, and X. Chen, “Parameter analysis of an ammonia-water power cycle with a gravity assisted thermal driven ‘pump’ for low-grade heat recovery,” *Renew. Energy*, vol. 146, pp. 651–661, Feb. 2020, doi: 10.1016/J.RENENE.2019.07.014.

[16] D. Lu *et al.*, “Modeling and analysis of an ammonia–water absorption refrigeration system utilizing waste heat with large temperature span,” *Int. J. Refrig.*, vol. 103, pp. 180–190, Jul. 2019, doi: 10.1016/J.IJREFRIG.2019.04.008.

[17] L. Sun, W. Han, X. Jing, D. Zheng, and H. Jin, “A power and cooling cogeneration system using mid/low-temperature heat source,” *Appl. Energy*, vol. 112, pp. 886–897, Dec. 2013, doi: 10.1016/J.APENERGY.2013.03.049.

[18] F. Mohammadkhani, F. Ranjbar, and M. Yari, “A comparative study on the ammonia–water based bottoming power cycles: The exergoeconomic viewpoint,” *Energy*, vol. 87, pp. 425–434, Jul. 2015, doi: 10.1016/J.ENERGY.2015.05.023.

[19] S. C. Kaushik and R. Kumar, “Thermodynamic study of a two-stage vapour absorption refrigeration system using NH3 refrigerant with liquid/solid absorbents,” *Energy Convers. Manag.*, vol. 25, no. 4, pp. 427–431, 1985, doi: 10.1016/0196-8904(85)90007-X.

[20] A. Altamirano, N. Le Pierrès, and B. Stutz, “Review of small-capacity single-stage continuous absorption systems operating on binary working fluids for cooling: Theoretical, experimental and commercial cycles,” *Int. J. Refrig.*, vol. 106, pp. 350–373, Oct. 2019, doi: 10.1016/J.IJREFRIG.2019.06.033.

[21] D.-W. Sun, “Comparison of the performances of NH3-H2O, NH3-LiNO3 and NH3-NaSCN absorption refrigeration systems,” *Energy Convers. Manag.*, vol. 39, no. 5–6, pp. 357–368, Mar. 1998, doi: 10.1016/S0196-8904(97)00027-7.

[22] R. R. M.O. Mclinden, “An experimental comparison of NH3–H2O and NH3–H2O–LiBr mixtures in an absorption heat pump,” pp. 1837–1846.

[23] S. Steiu, D. Salavera, J. C. Bruno, and A. Coronas, “A basis for the development of new ammonia-water-sodium hydroxide absorption chillers,” *Int. J. Refrig.*, 2009, doi: 10.1016/j.ijrefrig.2009.02.017.

[24] A. A. Berestneff, “Absorption refrigeration,” *Mech. Eng.*, vol. 72, pp. 216–235, 1949.

[25] M. A. R. Eisa, I. G. A. Rashed, S. Devotta, and F. A. Holland, “Thermodynamic design data for absorption heat pump systems operating on water-lithium bromide part

II: Heating," *Appl. Energy*, vol. 25, no. 1, pp. 71–82, Jan. 1986, doi: 10.1016/0306-2619(86)90062-0.

[26] H. R. Patil, S. K. Chaudhari, and S. S. Katti, "Thermodynamic design data for absorption heat pump systems operating on water-lithium iodide—part II. Heating," *Heat Recover. Syst. CHP*, vol. 11, no. 5, pp. 351–360, Jan. 1991, doi: 10.1016/0890-4332(91)90003-M.

[27] R. Best, "Modelling of single-effect stage and advanced absorption heat transformers operating with H2O/carrol mixture," *Appl. Therm. Eng.*, vol. 17, pp. 1111–1112, 1997.

[28] H. Lee, J. Kim, and Y. Park, "Performance evaluation of absorption chiller using LiBr+H2N(CH2)2OH+H2O, LiBr+HO(CH2)3OH+H2O, and LiBr+(HOCH2CH2)2NH+H2O as working fluids," *Appl. Therm. Eng.*, vol. 19, no. 2, pp. 217–225, 1999, [Online]. Available: http://linkinghub.elsevier.com/retrieve/pii/S1359431198000325.

[29] G. G. A. M.B.R. Rosa, M.A.G. Victor, "Performance modeling of single and double absorption heat transformers," *Curr. Appl. Phys.*, vol. 10, pp. 244–248, 2010.

[30] F. R. J. D.L. Antonio, D. Marina, "Absorption of H2O vapor into new working fluids for absorption refrigeration systems," *Ind. Eng. Chem. Res.*, vol. 46, pp. 345–350, 2007.

[31] F. R. J. D.L. Antonio, D. Marina, "Vapor pressures, densities, and viscosities of the (H2O + LiBr + sodium formate) system and (H2O + LiBr + potassium formate) system," *J. Chem. Eng. Data*, vol. 48, pp. 18–22, 200AD.

[32] A. De Lucas, M. Donate, C. Molero, J. Villaseñor, and J. F. Rodríguez, "Performance evaluation and simulation of a new absorbent for an absorption refrigeration system," *Int. J. Refrig.*, vol. 27, no. 4, pp. 324–330, Jun. 2004, doi: 10.1016/J.IJREFRIG.2003.12.008.

[33] M. Bourouis, M. Vallès, M. Medrano, and A. Coronas, “Absorption of water vapour in the falling film of water–(LiBr + LiI + LiNO3 + LiCl) in a vertical tube at air-cooling thermal conditions,” *Int. J. Therm. Sci.,* vol. 44, no. 5, pp. 491–498, May 2005, doi: 10.1016/J.IJTHERMALSCI.2004.11.009.

[34] A. M. M. D. Salavera, X. Esteve, K.R. Patil, “Coronas solubility, heat capacity, and density of LiBr + Lithium Iodide + Lithium Nitrate + Lithium chloride aqueous solutions at several compositions and temperatures,” *J. Chem. Eng. Data,* vol. 49, pp. 613–619, 2004.

[35] J. S. M. Bourouis, A. Coronas, R.J. Romero, “Purification of sea H2O using absorption heat transformers with H2O-(LiBr + LiI + LiNO3 + LiCl) and low temperature heat sources,” *Desalination,* vol. 166, pp. 209–214, 2004.

[36] H. R. Lee *et al.*, “Thermodynamic design data and performance evaluation of the water+lithium bromide+lithium iodide+lithium nitrate+lithium chloride system for absorption chiller,” *Appl. Therm. Eng.*, vol. 20, no. 8, pp. 707–720, 2000, doi: 10.1016/S1359-4311(99)00059-9.

[37] D. C. E. W.F. Davidson, “260 °C aqueous absorption working pair under development,” *IEA Heat Pump Centre Newsletter*, vol. 4, pp. 29–31, 1986.

[38] D. C. E. L.A. Howe, “260 °C absorption working pair ready for field test,” vol. 8, pp. 7–9, 1990.

[39] C. Z. Zhuo and C. H. M. Machielsen, “Performance of high-temperature absorption heat transformers using alkitrate as the working pair,” *Appl. Therm. Eng.*, vol. 16, no. 3, pp. 255–262, 1996, doi: 10.1016/1359-4311(95)00069-0.

[40] M. Flamensbeck, F. Summerer, P. Riesch, F. Ziegler, and G. Alefeld, “A cost effective absorption chiller with plate heat exchangers using water and hydroxides,” *Appl. Therm. Eng.*, vol. 18, no. 6, pp. 413–425, 1998, doi: 10.1016/S1359-4311(97)00049-5.

[41] F. A. H. R. Best, “A study of the operating characteristics of an experimental absorption cooler using ternary systems,” *Reservation*, vol. 14. pp. 553–561, 1990.

[42] Z. He, Z. Zhao, X. Zhang, and H. Feng, “Thermodynamic properties of new heat pump working pairs: 1,3-Dimethylimidazolium dimethylphosphate and water, ethanol and methanol,” *Fluid Phase Equilib.*, vol. 298, no. 1, pp. 83–91, Nov. 2010, doi: 10.1016/J.FLUID.2010.07.005.

[43] R. Saravanan and M. P. Maiya, “Thermodynamic comparison of water-based working fluid combinations for a vapour absorption refrigeration system,” *Appl. Therm. Eng.*, vol. 18, no. 7, pp. 553–568, 1998, doi: 10.1016/S1359-4311(97)00072-0.

[44] T. K. Gogoi and D. Konwar, “Exergy analysis of a H2O-LiCl absorption refrigeration system with operating temperatures estimated through inverse analysis,” *Energy Convers. Manag.*, vol. 110, pp. 436–447, 2016, doi: 10.1016/j.enconman.2015.12.037.

[45] J. Yin, L. Shi, M. S. Zhu, and L. Z. Han, “Performance analysis of an absorption heat transformer with different working fluid combinations,” *Appl. Energy*, vol. 67, no. 3, pp. 281–292, 2000, doi: 10.1016/S0306-2619(00)00024-6.

[46] A. Coronas, M. Vallès, S. K. Chaudhari, and K. R. Patil, “Absorption heat pump with the TFE-TEGDME and TFE-H2O-TEGDME systems,” *Appl. Therm. Eng.*, vol. 16, no. 4, pp. 335–345, 1996, doi: 10.1016/1359-4311(95)00007-0.

[47] K. Stephan and R. Hengerer, “Heat transformation with the ternary working fluid TFE-H2O-E181: Transformation de chaleur avec le fluide de travail ternaire TFE-H2O-E181,” *Int. J. Refrig.*, vol. 16, no. 2, pp. 120–128, Jan. 1993, doi: 10.1016/0140-7007(93)90068-J.

[48] M. Medrano, M. Bourouis, and A. Coronas, “Double-lift absorption refrigeration cycles driven by low–temperature heat sources using organic fluid mixtures as working pairs,” *Appl. Energy*, vol. 68, no. 2, pp. 173–185, Feb. 2001, doi:

10.1016/S0306-2619(00)00048-9.

[49] Z. Zhao, X. Zhang, and X. Ma, “Thermodynamic performance of a double-effect absorption heat-transformer using TFE/E181 as the working fluid,” *Appl. Energy*, vol. 82, no. 2, pp. 107–116, Oct. 2005, doi: 10.1016/J.APENERGY.2004.10.012.

[50] M. Jelinek and I. Borde, “Single- and double-stage absorption cycles based on fluorocarbon refrigerants and organic absorbents,” *Appl. Therm. Eng.*, vol. 18, no. 9–10, pp. 765–771, Sep. 1998, doi: 10.1016/S1359-4311(97)00114-2.

[51] I. Borde, M. Jelinek, and N. . Daltrophe, “Absorption system based on the refrigerant R134a,” *Int. J. Refrig.*, vol. 18, no. 6, pp. 387–394, Jul. 1995, doi: 10.1016/0140-7007(95)98161-D.

[52] I. Borde, M. Jelinek, and N. . Daltrophe, “Working fluids for an absorption system based on R124 (2-chloro-1,1,1,2,-tetrafluoroethane) and organic absorbents,” *Int. J. Refrig.*, vol. 20, no. 4, pp. 256–266, Jun. 1997, doi: 10.1016/S0140-7007(97)00090-X.

[53] M. Jelinek and I. Borde, “Working fluids for absorption heat pumps based on R125 (pentafluoroethane) and organic absorbents,” in *International Sorption Heat Pumps Conference, Munich, Germa*, 1999, pp. 205–208.

[54] K. Makita, “Development and commercialisation of triple-effect absorption chiller-heaters,” 2006.

[55] Mori K, Oka M, and Ohhashi T, “Development of triple-effect absorption chiller-heater,” 2005.

[56] L. K. C. Tse, S. Wilkins, N. McGlashan, B. Urban, and R. Martinez-Botas, “Solid oxide fuel cell/gas turbine trigeneration system for marine applications,” *J. Power Sources*, vol. 196, no. 6, pp. 3149–3162, 2011, doi: 10.1016/j.jpowsour.2010.11.099.

[57] A. Scotta, “3-Stage absorption chiller successfully tested in field,” *Heat. Pip. air Cond. Eng.*, vol. 75, no. 1, p. 15, 2003.

[58] Devault RC and Biermann WJ, “Absorption refrigeration system with double-condenser coupling. USA, Patent No. 5,205,136.”

[59] M. Izquierdo, R. Lizarte, J. D. Marcos, and G. Gutiérrez, “Air conditioning using an air-cooled single effect lithium bromide absorption chiller: Results of a trial conducted in Madrid in August 2005,” *Appl. Therm. Eng.*, vol. 28, no. 8–9, pp. 1074–1081, Jun. 2008, doi: 10.1016/J.APPLTHERMALENG.2007.06.009.

[60] R. A. Zogg, M. Y. Feng, and D. Westphalen, “Guide to Developing Air-Cooled LiBr Absorption for Combined Heat and Power Applications,” *Heat Mass Transf.*, no. April, p. 37, 2005, doi: Re:D0281.

[61] I. Stambler, “4.6 MW plant with an indirect fired 2600 ton chiller at 76.8% efficiency,” *Gas Turbine World*, vol. 34, no. 4. pp. 14–17, 2004, [Online]. Available: http://www.scopus.com/inward/record.url?eid=2-s2.0-7044271144&partnerID=tZOtx3y1.

[62] P. Srikhirin, S. Aphornratana, and S. Chungpaibulpatana, “A review of absorption refrigeration technologies,” *Renew. Sustain. Energy Rev.*, vol. 5, no. 4, pp. 343–372, 2000, doi: 10.1016/S1364-0321(01)00003-X.

[63] S. E. Systems, “Report on Energy Efficient and Renewable Energy Systems Planning and Recommendations for their Successful Application,” *Renew. Energy*, p. 186, 2011.

[64] H. A, L. F, Z. C, B. M, R. M, and et al. Henning HM, “A linear concentrating Fresnel collector driving a NH3–H2O absorption chiller,” in *Proceedings of the second international conference solar air-conditioning*, 2007, pp. 662–667.

[65] S. Alam, “A Proposed Model for Utilizing Exhaust Heat to run Automobile Air-conditioner,” *2nd Jt. Int. Conf. “Sustainable Energy Environ. (SEE 2006)*, vol. E-011(P), no. November, pp. 21–23, 2006.

[66] A. Ouadha and Y. El-Gotni, “Integration of an Ammonia-water Absorption

Refrigeration System with a Marine Diesel Engine: A Thermodynamic Study," *Procedia Comput. Sci.*, vol. 19, pp. 754–761, Jan. 2013, doi: 10.1016/J.PROCS.2013.06.099.

[67] J. Fernández-Seara, A. Vales, and M. Vázquez, "Heat recovery system to power an onboard NH3-H2O absorption refrigeration plant in trawler chiller fishing vessels," *Appl. Therm. Eng.*, vol. 18, no. 12, pp. 1189–1205, 1998, doi: 10.1016/S1359-4311(98)00001-5.

[68] M. Talbi and B. Agnew, "Energy recovery from diesel engine exhaust gases for performance enhancement and air conditioning," vol. 22, no. C, pp. 693–702, 2006.

[69] C. m. Keinath, J. C. Delahanty, S. Garimella, and M. A. Garrabrant, "Diesel Engine Waste-Heat Driven Ammonia-Water Absorption System for Space-Conditioning Applications," 2012.

[70] A. Ramanathan and P. Gunasekaran, "Simulation of absorption refrigeration system for automobile application," *Therm. Sci.*, vol. 12, no. 3, pp. 5–13, 2008, doi: 10.2298/TSCI0803005R.

[71] G. Vicatos, J. Gryzagoridis, and S. Wang, "A car air-conditioning system based on an absorption refrigeration cycle using energy from exhaust gas of an internal combustion engine," *J. Energy South. Africa*, vol. 19, no. 4, pp. 6–11, 2017, doi: 10.17159/2413-3051/2008/v19i4a3331.

[72] N. Javani, I. Dincer, and G. F. Naterer, "Thermodynamic analysis of waste heat recovery for cooling systems in hybrid and electric vehicles," *Energy*, vol. 46, no. 1, pp. 109–116, 2012, doi: 10.1016/j.energy.2012.02.027.

[73] N. Sarabchi, R. Khoshbakhti Saray, and S. M. S. Mahmoudi, "Utilization of waste heat from a HCCI (homogeneous charge compression ignition) engine in a tri-generation system," *Energy*, vol. 55, pp. 965–976, Jun. 2013, doi:

10.1016/J.ENERGY.2013.03.065.

[74] K. AlQdah, S. Alsaqoor, and A. Al-Jarrah, “Design and Fabrication of Auto Air Conditioner Generator Utilizing Exhaust Waste Energy from a Diesel Engine,” *Int. J. Therm. Environ. Eng.*, vol. 3, no. 2, pp. 87–93, 2011, doi: 10.5383/ijtee.03.02.005.

[75] H. L. Talom and A. Beyene, “Heat recovery from automotive engine,” *Appl. Therm. Eng.*, vol. 29, no. 2–3, pp. 439–444, 2009, doi: 10.1016/j.applthermaleng.2008.03.021.

[76] I. Horuz, “An alternative road transport refrigeration,” *Turkish J. Eng. Environ. Sci.*, vol. 22, no. 3, pp. 211–222, 1998.

[77] I. Horuz and T. M. S. Callander, “Experimental investigation of a vapor absorption refrigeration system,” *Int. J. Refrig.*, vol. 27, no. 1, pp. 10–16, 2004, doi: 10.1016/S0140-7007(03)00119-1.

[78] A. A. Manzela, S. M. Hanriot, L. Cabezas-Gómez, and J. R. Sodré, “Using engine exhaust gas as energy source for an absorption refrigeration system,” *Appl. Energy*, vol. 87, no. 4, pp. 1141–1148, 2010, doi: 10.1016/j.apenergy.2009.07.018.

[79] K. S. Alqdah, “Performance and evaluation of aqua ammonia auto air conditioner system using exhaust waste energy,” *Energy Procedia*, vol. 6, pp. 467–476, 2011, doi: 10.1016/j.egypro.2011.05.054.

[80] S. Kaewpradub *et al.*, “Absorption refrigeration system using engine exhaust gas as an energy source,” *Case Stud. Therm. Eng.*, vol. 12, no. August, pp. 797–804, 2018, doi: 10.1016/j.csite.2018.10.003.

[81] W. I. A. Aly, M. Abdo, G. Bedair, and A. E. Hassaneen, “Thermal performance of a diffusion absorption refrigeration system driven by waste heat from diesel engine exhaust gases,” *Appl. Therm. Eng.*, vol. 114, pp. 621–630, 2017, doi: 10.1016/j.applthermaleng.2016.12.019.

[82] Z. Yu, J. Han, and X. Cao, “Investigation on performance of an integrated solid oxide

fuel cell and absorption chiller tri-generation system," *Int. J. Hydrogen Energy*, vol. 36, no. 19, pp. 12561–12573, Sep. 2011, doi: 10.1016/j.ijhydene.2011.06.147.

[83] Y. Wang, Y. Shi, M. Ni, and N. Cai, "A micro tri-generation system based on direct flame fuel cells for residential applications," *Int. J. Hydrogen Energy*, vol. 39, no. 11, pp. 5996–6005, 2014, doi: 10.1016/j.ijhydene.2014.01.183.

[84] P. Margalef and S. Samuelsen, "Integration of a molten carbonate fuel cell with a direct exhaust absorption chiller," *J. Power Sources*, vol. 195, no. 17, pp. 5674–5685, Sep. 2010, doi: 10.1016/j.jpowsour.2010.03.051.

[85] M. Ishizawa, S. Okada, and T. Yamashita, "Highly efficient heat recovery system for phosphoric acid fuel cells used for cooling telecommunication equipment," *J. Power Sources*, vol. 86, no. 1, pp. 294–297, 2000, doi: 10.1016/S0378-7753(99)00411-5.

[86] V. Venkataraman, A. W. Pacek, and R. Steinberger-Wilckens, "Coupling of a Solid Oxide Fuel Cell Auxiliary Power Unit with a Vapour Absorption Refrigeration System for Refrigerated Truck Application," *Fuel Cells*, vol. 16, no. 3, pp. 273–293, 2016, doi: 10.1002/fuce.201500124.

[87] P. Kazempoor, V. Dorer, and A. Weber, "Modelling and evaluation of building integrated SOFC systems," *Int. J. Hydrogen Energy*, vol. 36, no. 20, pp. 13241–13249, Oct. 2011, doi: 10.1016/j.ijhydene.2010.11.003.

[88] O. Joneydi Shariatzadeh, A. H. Refahi, M. Rahmani, and S. S. Abolhassani, "Economic optimisation and thermodynamic modelling of SOFC tri-generation system fed by biogas," *Energy Convers. Manag.*, vol. 105, pp. 772–781, 2015, doi: 10.1016/j.enconman.2015.08.026.

[89] M. Fazly, J. M. Ali, F. Ramadhani, M. A. Hussain, and H. Mokhlis, "Evaluation of solid oxide fuel cell based polygeneration system in residential areas integrating with electric charging and hydrogen fueling stations for vehicles," *Appl. Energy*, vol. 238,

no. October 2018, pp. 1373–1388, 2019, doi: 10.1016/j.apenergy.2019.01.150.

[90] N. Li *et al.*, "Economic and environmental multi-optimal design and dispatch of solid oxide fuel cell based CCHP system," *Energy Convers. Manag.*, vol. 154, no. November, pp. 365–379, 2017, doi: 10.1016/j.enconman.2017.11.035.

[91] H. Zhao, T. Jiang, and H. Hou, "Performance analysis of the SOFC-CCHP system based on H2O/Li-Br absorption refrigeration cycle fueled by coke oven gas," *Energy*, vol. 91, pp. 983–993, 2015, doi: 10.1016/j.energy.2015.08.087.

[92] C. Weber, M. Koyama, and S. Kraines, "CO2-emissions reduction potential and costs of a decentralized energy system for providing electricity, cooling and heating in an office-building in Tokyo," *Energy*, vol. 31, no. 14, pp. 3041–3061, 2006, doi: 10.1016/j.energy.2005.12.003.

[93] F. Calise, G. Ferruzzi, and L. Vanoli, "Transient simulation of polygeneration systems based on PEM fuel cells and solar heating and cooling technologies," *Energy*, vol. 41, no. 1, pp. 18–30, 2012, doi: 10.1016/j.energy.2011.05.027.

[94] P. Tippawan, A. Arpornwichanop, and I. Dincer, "Energy and exergy analyses of an ethanol-fueled solid oxide fuel cell for a trigeneration system," *Energy*, vol. 87, pp. 228–239, 2015, doi: 10.1016/j.energy.2015.04.072.

[95] V. Venkataraman, A. El-Kharouf, B. Pandya, E. Amakiri, and R. Steinberger-Wilckens, "Coupling of engine exhaust and fuel cell exhaust with vapour absorption refrigeration/air conditioning systems for transport applications: A Review," *Therm. Sci. Eng. Prog.*, vol. 18, no. March, p. 100550, 2020, doi: 10.1016/j.tsep.2020.100550.

[96] B. Pandya, A. El-Kharouf, V. Venkataraman, and R. Steinberger-Wilckens, "Comparative Study of Solid Oxide Fuel Cell Coupled Absorption Refrigeration System for Green and Sustainable Refrigerated Transportation," *Appl. Therm. Eng.*, p. 115597, 2020, doi: 10.1016/j.applthermaleng.2020.115597.

[97] K. Brooks, P. Pm, G. Block, and N. F. Cells, “Demonstration of Fuel Cell Auxiliary Power Unit (APU) to Power Truck Refrigeration Units (TRUs) in Refrigerated Trucks,” 2016.

[98] G. Loreti, A. L. Facci, I. Baffo, and S. Ubertini, “Combined heat, cooling, and power systems based on half effect absorption chillers and polymer electrolyte membrane fuel cells,” *Appl. Energy*, vol. 235, no. April 2018, pp. 747–760, 2019, doi: 10.1016/j.apenergy.2018.10.109.

[99] F. Flow, “Fluid f l o w and heat transfer between finite rotating disks,” vol. 11, no. 1, pp. 155–163, 1990.

[100] G. Fabbri, “Heat transfer optimization in internally finned tubes under laminar flow conditions,” *Int. J. Heat Mass Transf.*, vol. 41, no. 10, pp. 1243–1253, 1998, doi: 10.1016/S0017-9310(97)00209-3.

[101] B. Kundu and P. K. Das, “Performance analysis and optimization of straight taper fins with variable heat transfer coefficient,” *Int. J. Heat Mass Transf.*, vol. 45, no. 24, pp. 4739–4751, 2002, doi: 10.1016/S0017-9310(02)00189-8.

[102] S. K. Rout, D. N. Thatoi, A. K. Acharya, and D. P. Mishra, “CFD supported performance estimation of an internally finned tube heat exchanger under mixed convection flow,” *Procedia Eng.*, vol. 38, no. Icmoc, pp. 585–597, 2012, doi: 10.1016/j.proeng.2012.06.073.

[103] W. K. Tien, R. H. Yeh, and J. C. Hsiao, “Numerical analysis of laminar flow and heat transfer in internally finned tubes,” *Heat Transf. Eng.*, vol. 33, no. 11, pp. 957–971, 2012, doi: 10.1080/01457632.2012.654729.

[104] H. M. Soliman and A. Feingold, “Analysis of fully developed laminar flow in longitudinal internally finned tubes,” *Chem. Eng. J.*, vol. 14, no. 2, pp. 119–128, 1977, doi: 10.1016/0300-9467(77)85007-7.

[105] N. Sreedhar and G. Varghese, “Analysis of longitudinal fin patterns in a concentric double tube heat exchanger using LMTD and CFD techniques,” *Int. J. Appl. Eng. Res.*, vol. 12, no. 17, pp. 6471–6479, 2017.

[106] M. J. Indhe, V. W. Bhatkar, M. H. Power, G. S. M. College, and O. Engg, “OPTIMIZATION OF LONGITUDINAL FIN PROFILE FOR DOUBLE PIPE HEAT EXCHANGER,” pp. 517–529, 2015.

[107] L. H. Tang, M. Zeng, and Q. W. Wang, “Experimental and numerical investigation on air-side performance of fin-and-tube heat exchangers with various fin patterns,” *Exp. Therm. Fluid Sci.*, vol. 33, no. 5, pp. 818–827, 2009, doi: 10.1016/j.expthermflusci.2009.02.008.

[108] H. M. Transfer, “Experimental Measurements of Heat Transfer in an,” vol. 25, no. 5, pp. 619–630, 1998.

[109] WilkeW., *VDI Heat Atlas*. 1962.

[110] J. Taborek, “Double-pipe and multitube heat exchangers with plain and longitudinal finned tubes,” *Heat Transf. Eng.*, vol. 18, no. 2, pp. 34–45, 1997, doi: 10.1080/01457639708939894.

[111] B. C. Ankanna and B. S. Reddy, “Performance Analysis of Fabricated Helical Coil Heat Exchanger,” *Int. J. Eng. Res.*, vol. 5013, no. 3, pp. 33–39, 2014.

[112] R. Andrzejczyk and T. Muszyński, “Performance analyses of helical coil heat exchangers. the effect of external coil surface modification on heat exchanger effectiveness,” *Arch. Thermodyn.*, vol. 37, no. 4, pp. 137–159, 2016, doi: 10.1515/aoter-2016-0032.

[113] M. Lazova, H. Huisseune, A. Kaya, S. Lecompte, G. Kosmadakis, and M. De Paepe, “Performance Evaluation of a Helical Coil Heat Exchanger Working under Supercritical Conditions in a Solar Organic Rankine Cycle Installation,” *Energies*, vol.

9, no. 6, p. 432, 2016, doi: 10.3390/en9060432.

[114] M. Aminyavari, M. Aprile, T. Toppi, S. Garone, and M. Motta, “Étude Détaillée Sur Le Transfert Simultané De Chaleur Et De Masse Dans Un Tube Absorbeur Vertical À Film Tombant,” *Int. J. Refrig.*, vol. 80, pp. 37–51, 2017, doi: 10.1016/j.ijrefrig.2017.04.029.

[115] J. Fernández-Seara, J. Sieres, C. Rodríguez, and M. Vázquez, “Ammonia-water absorption in vertical tubular absorbers,” *Int. J. Therm. Sci.*, vol. 44, no. 3, pp. 277–288, 2005, doi: 10.1016/j.ijthermalsci.2004.09.001.

[116] Y. T. Kang, A. Akisawa, and T. Kashiwagi, “Analytical investigation of two di € erent absorption modes : falling ® lm and bubble types Comparaison de deux modes d ’ absorption : ® lm tombant et bulles : falling ® lm and bubble types,” *Int. J. Refrig.*, vol. 23, pp. 430–443, 2000.

[117] C. A. I. Ferreira, C. Keizer, and C. H. M. Machielsen, “Heat and mass transfer in vertical tubular bubble absorbers for ammonia-water absorption refrigeration systems,” *Int. J. Refrig.*, vol. 7, no. 6, pp. 348–357, 1984, doi: 10.1016/0140-7007(84)90004-5.

[118] J. Fernández-Seara, F. J. Uhía, and J. Sieres, “Analysis of an air cooled ammonia-water vertical tubular absorber,” *Int. J. Therm. Sci.*, vol. 46, no. 1, pp. 93–103, 2007, doi: 10.1016/j.ijthermalsci.2006.03.005.

[119] X. Wu, S. Xu, and M. Jiang, “Development of bubble absorption refrigeration technology: A review,” *Renew. Sustain. Energy Rev.*, vol. 82, no. 2, pp. 3468–3482, 2018, doi: 10.1016/j.rser.2017.10.109.

[120] M. Jiang, S. Xu, X. Wu, J. Hu, and W. Wang, “Visual experimental research on the effect of nozzle orifice structure on R124-DMAC absorption process in a vertical bubble tube,” *Int. J. Refrig.*, vol. 68, pp. 107–117, 2016, doi: 10.1016/j.ijrefrig.2016.04.025.

[121] N. Goel and D. Y. Goswami, “Analysis of a counter-current vapor flow absorber,” *Int. J. Heat Mass Transf.*, vol. 48, no. 7, pp. 1283–1292, 2005, doi: 10.1016/j.ijheatmasstransfer.2004.10.009.

[122] P. Lin, R. Z. Wang, and Z. Z. Xia, “Numerical investigation of a two-stage air-cooled absorption refrigeration system for solar cooling: Cycle analysis and absorption cooling performances,” *Renew. Energy*, vol. 36, no. 5, pp. 1401–1412, 2011, doi: 10.1016/j.renene.2010.11.005.

[123] S. M. Yih, “Modeling heat and mass transfer in wavy and turbulent falling liquid films,” *Wärme- und Stoffübertragung*, vol. 21, no. 6, pp. 373–381, 1987, doi: 10.1007/BF01376293.

[124] T. H. Chilton and A. P. Colburn, “Mass Transfer (Absorption) Coefficients: Prediction from Data on Heat Transfer and Fluid Friction,” *Ind. Eng. Chem.*, vol. 26, no. 11, pp. 1183–1187, 1934, doi: 10.1021/ie50299a012.

[125] John Wiley & Sons Inc. (1987), *Handbook of single-phase convective heat transfer*. 1987.

[126] T. B. Unversity, “On Upward Flow of Gas-Liquid Mixtures in Vertical Tubes,” 2008. doi: 10.1248/cpb.37.3229.

[127] I. Ferreira, “Vertical Tubular Absorbers for Ammonia-Salt Absorption Refrigeration,” 1985.

[128] C. H. Scholz, “The Prediction of bubble Terminal velocities from wave Theory,” *Science (80-.).*, vol. 327, no. 5969, pp. 1082–1082, 2010, doi: 10.1126/science.1187372.

[129] M. A. R. Talaia, “Terminal velocity of a bubble rise in a liquid column,” *Proc. World Acad. Sci. Eng. Technol.*, no. 28, pp. 264–268, 2007, doi: 10.1016/j.jjcc.2011.11.013.

[130] P. K, “M echanisms of heat ¯ ow in suspensions of nano-sized particles nano ¯ uids),”

Int. J. Heat Mass Transf., vol. 45, pp. 855–863, 2002.

[131] N. A. C. Sidik, I. A. Muhammad, R. Mamat, M. J. Muhammad, G. Najafi, and M. N. A. W. M. Yazid, "The use of nanofluids for enhancing the thermal performance of stationary solar collectors: A review," *Renew. Sustain. Energy Rev.*, vol. 63, pp. 226–236, 2016, doi: 10.1016/j.rser.2016.05.063.

[132] W. D. Wu, G. Liu, S. X. Chen, and H. Zhang, "Nanoferrofluid addition enhances ammonia/water bubble absorption in an external magnetic field," *Energy Build.*, vol. 57, pp. 268–277, 2013, doi: 10.1016/j.enbuild.2012.10.032.

[133] C. Pang, W. Wu, W. Sheng, H. Zhang, and Y. T. Kang, "Mass transfer enhancement by binary nanofluids (NH 3/H 2O + Ag nanoparticles) for bubble absorption process," *Int. J. Refrig.*, vol. 35, no. 8, pp. 2240–2247, 2012, doi: 10.1016/j.ijrefrig.2012.08.006.

[134] J. K. Kim, J. Y. Jung, and Y. T. Kang, "Absorption performance enhancement by nano-particles and chemical surfactants in binary nanofluids," *Int. J. Refrig.*, vol. 30, no. 1, pp. 50–57, 2007, doi: 10.1016/j.ijrefrig.2006.04.006.

[135] J. K. Kim, J. Y. Jung, and Y. T. Kang, "The effect of nano-particles on the bubble absorption performance in a binary nanofluid," *Int. J. Refrig.*, vol. 29, no. 1, pp. 22–29, 2006, doi: 10.1016/j.ijrefrig.2005.08.006.

[136] A. K. Rasheed, M. Khalid, W. Rashmi, T. C. S. M. Gupta, and A. Chan, "Graphene based nanofluids and nanolubricants - Review of recent developments," *Renew. Sustain. Energy Rev.*, vol. 63, pp. 346–362, 2016, doi: 10.1016/j.rser.2016.04.072.

[137] D. K. Devendiran and V. A. Amirtham, "A review on preparation, characterization, properties and applications of nanofluids," *Renew. Sustain. Energy Rev.*, vol. 60, pp. 21–40, 2016, doi: 10.1016/j.rser.2016.01.055.

[138] I. M. Shahrul, I. M. Mahbubul, S. S. Khaleduzzaman, R. Saidur, and M. F. M. Sabri, "A comparative review on the specific heat of nanofluids for energy perspective,"

Renew. Sustain. Energy Rev., vol. 38, pp. 88–98, 2014, doi: 10.1016/j.rser.2014.05.081.

[139] L. Yang, K. Du, S. Bao, and Y. Wu, "Investigations of selection of nanofluid applied to the ammonia absorption refrigeration system Etudes sur la sélection des nanofluides utilisés dans les systèmes frigorifiques à ammoniac à absorption," *Int. J. Refrig.*, vol. 35, no. 8, pp. 2248–2260, 2012, doi: 10.1016/j.ijrefrig.2012.08.003.

[140] Y. Zhang, L. Yang, K. Du, X. Niu, and Y. Li, "An experimental and theoretical study of the influence of surfactant on the preparation and stability of ammonia-water nanofluids," *Int. J. Refrig.*, vol. 34, no. 8, pp. 1741–1748, 2011, doi: 10.1016/j.ijrefrig.2011.06.007.

[141] L. Yang, K. Du, X. S. Zhang, and B. Cheng, "Preparation and stability of Al2O3 nano-particle suspension of ammonia-water solution," *Appl. Therm. Eng.*, vol. 31, no. 17–18, pp. 3643–3647, 2011, doi: 10.1016/j.applthermaleng.2010.11.031.

[142] Y. J. Kim, J. K. Lee, and Y. T. Kang, "The effect of oil-droplet on bubble absorption performance in binary nanoemulsions Nanoémulsions binaires," *Int. J. Refrig.*, vol. 34, no. 8, pp. 1734–1740, 2011, doi: 10.1016/j.ijrefrig.2011.07.008.

[143] Y. T. Kang, M.-G. Kim, T. Kashiwagi, J. H. Kim, J.-K. Kim, and J. Y. Jung, "The effect of chemical surfactants on the absorption performance during NH3/H2O bubble absorption process," *Int. J. Refrig.*, vol. 29, no. 2, pp. 170–177, 2005, doi: 10.1016/j.ijrefrig.2005.06.006.

[144] Y. Cuenca, A. Vernet, and M. Vallès, "Thermal conductivity enhancement of the binary mixture (NH<inf>3</inf> + LiNO<inf>3</inf>) by the addition of CNTs," *Int. J. Refrig.*, vol. 41, pp. 113–120, 2014, doi: 10.1016/j.ijrefrig.2013.12.013.

[145] L. Chen and H. Xie, "Surfactant-free nanofluids containing double- and single-walled carbon nanotubes functionalized by a wet-mechanochemical reaction," *Thermochim.*

Acta, vol. 497, no. 1–2, pp. 67–71, 2010, doi: 10.1016/j.tca.2009.08.009.

[146] M. Legay, B. Simony, P. Boldo, N. Gondrexon, S. Le Person, and A. Bontemps, "Improvement of heat transfer by means of ultrasound: Application to a double-tube heat exchanger," *Ultrason. Sonochem.*, vol. 19, no. 6, pp. 1194–1200, 2012, doi: 10.1016/j.ultsonch.2012.04.001.

[147] Y. Yao, "Research and applications of ultrasound in HVAC field: A review," *Renew. Sustain. Energy Rev.*, vol. 58, pp. 52–68, 2016, doi: 10.1016/j.rser.2015.12.222.

[148] I. Vilarinho, D. Rossetti, and and R. Critoph, "Evaluation of Solar Assisted Sorption Refrigeration for Ice Cream Cabinets: I Absorption."

[149] V. Venkataraman, "Coupling of a Solid Oxide Fuel Cell with a Vapour Absorption Refrigeration System for refrigerated truck application," PhD thesis, University of Birmingham, UK, 2017.